UNIVERSIDADE ESTADUAL DE CAMPINAS

INSTITUTO DE QUÍMICA

Vera Katic

SYNTHESIS AND APPLICATION OF INORGANIC MATERIALS IN ELECTROCHEMICAL SENSING

SÍNTESE E APLICAÇÃO DOS MATERIAIS INORGÂNICOS COMO SENSORES ELETROQUÍMICOS

CAMPINAS

2018

VERA KATIC

SYNTHESIS AND APPLICATION OF INORGANIC MATERIALS IN ELECTROCHEMICAL SENSING

SÍNTESE E APLICAÇÃO DOS MATERIAIS INORGÂNICOS COMO SENSORES ELETROQUÍMICOS

Tese de Doutorado apresentada ao Instituto de Química da Universidade Estadual de Campinas como parte dos requisitos exigidos para a obtenção do título de Doutora em Ciências

Doctor´s Thesis presented to the Institute of Chemistry of the University of Campinas as part of the requirements to obtain the title of Doctor in Sciences.

Supervisor: Prof. Dr. Juliano Alves Bonacin

ESTE EXEMPLAR CORRESPONDE À VERSÃO FINAL DA TESE DEFENDIDA PELA ALUNA VERA KATIC E ORIENTADA PELO PROF. DR. JULIANO ALVES BONACIN

CAMPINAS

2018

Agência(s) de fomento e nº(s) de processo(s): CNPq, 161819/2014-1; CAPES

Ficha catalográfica
Universidade Estadual de Campinas
Biblioteca do Instituto de Química
Camila Barleta Fullin - CRB 8462

K156s

Katic, Vera, 1986-
Synthesis and application of inorganic materials in electrochemical sensing / Vera Katic. – Campinas, SP : [s.n.], 2018.

Orientador: Juliano Alves Bonacin.
Tese (doutorado) – Universidade Estadual de Campinas, Instituto de Química.

1. Azul da Prússia. 2. Impressão tridimensional. I. Bonacin, Juliano Alves, 1980-. II. Universidade Estadual de Campinas. Instituto de Química. III. Título.

Informações para Biblioteca Digital

Título em outro idioma: Síntese e aplicação dos materiais inorgânicos como sensores eletroquímicos
Palavras-chave em inglês:
Prussian blue
Printing, three-dimensional
Área de concentração: Química Inorgânica
Titulação: Doutora em Ciências
Banca examinadora:
Juliano Alves Bonacin [Orientador]
Pedro Paulo Corbi
Italo Odone Mazali
Rodrigo Alejandro Abarza Munoz
Bruno Campos Janegitz
Data de defesa: 05-10-2018
Programa de Pós-Graduação: Química

BANCA EXAMINADORA

Prof. Dr. Juliano Alves Bonacin (Orientador)

Prof. Dr. Pedro Paulo Corbi (IQ-UNICAMP)

Prof. Dr. Italo Odone Mazali (IQ-UNICAMP)

Dr. Bruno Campos Janegitz (UFSCAR)

Dr. Rodrigo Alejandro Abarza Munoz (IQ-UFU)

A Ata da defesa com as respectivas assinaturas dos membros encontra-se no processo de vida acadêmica do(a) aluno(a).

Este exemplar corresponde à redação final da Tese de Doutorado defendida pelo(a) aluno(a) **VERA KATIC**, aprovada pela Comissão Julgadora em 5 outubro de 2018.

ACKNOWLEDGEMENTS

I wish to express my sincere gratitude and appreciation to my intelligent, hardworking and extremely patient supervisor, Prof. Dr. Juliano Alves Bonacin for accepting me into his group and keeping me motivated from the beginning. I am forever indebted for everything that he did for me, and for all the encouragement that I received from him.

My sincere thanks to our group, Bruno, Pãmyla, Matheus, Marcio, Kalil and Thiago, for their assistance in my experiments, helpful suggestions and friendly dealing; without their cooperation, the culmination of this project would not have taken place in time.

A big thank you goes to Pãmyla and Bruno with whom I rode this journey together. They have been very helping and supportive, sometimes out of the way, for their friendship, and all the fun and laughter.

I would like to thank all the professors at Labortório de Química de Coordenacão Prof Formiga, Prof Corbi and Prof Diego, for their kindness.

Thanks to my friends who are my lab fellows too; especially to Douglas and Naheedinha, Renan, Louis, Ana Carla, Carlos. Thanks to Ana Theresa for all the fun games and parties, and Rafael Enoque for all the kind words and photography sessions.

I am thankful to Isabel (Bel), Isabela and Janaina from CPG for their friendship and help in all the documents. I am also thankful to the lab assistant Cintia Massae, Diego, and especially Acacia (I don’t know how I’d even survive) for providing all the glassware, chemicals, and everything that I needed. They made my life easier.

Lab technicians of Microscopy (Hugito), UV (Claudinha), Raman (Milene), IR (Sonia), powder XRD (Renata), for their kindness and timely services. Lab technicians from Ensino (Lindo Reinaldo, Marcelo, Thalitinha, Michele, Daniel, Divino) fot making my PED days way easier.

I would also like to show my appreciation for the Crystallography Service in IQ, UNICAMP to Dr. Deborah Simoni, for spending long hours working with my crystals. I love crystals, receiving these results provided motivation and kept me going. Thank you!

A very big thanks to CNPq for my PhD scholarship, without this, my stay in Brazil would have been impossible.

This study was financed in part by the Coordenação de Aperfeiçoamento de Pessoal de Nível Superior - Brasil (CAPES) - Finance Code 001".

I would like to thank Brazil and Brazilians for opening their doors and hearts to foreign students who come here and take knowledge.

Now at the end of the road and looking back, I must admit that this PhD journey despite being challenging and demanding at times, has been a gratifying and empowering experience.

I offer my heartiest gratitude to my late father (Darko) and my lovely late Mom (Ankica) for their eternal support and love, for never clipping my feathers, their unconditional love made me set higher goals.

To my lovely husband Luciano Ferreira dos Reis without whom I do not know what I would do. Thank you for your love, support and especially for his patince.

Beskrajno sam zahvalna mom bratu Vladimiru i Jovani što su me trpeli u Srbiji I što su stalno tu za mene iako se ne čujemo koliko bih trebali. Osećam veliku zahvalnost što ste na svet doneli moje predivne bratanice Ani i Beku (koju još uvek nisam uživo videla). Iako su daleko jako ih volim.

Jako sam zahvalna Žulencetu, poznajemo se od davnih dana i zbog njega sam uspostavila odnos sa mojim bratom. Hvala ti na tome.

Jedna od stvari na koje sam najponosnija na ovom svetu su moja tri predivna prijateljstva, a to su sa Danijelom, Listinom i Ostinom. Bez vas ništa ne bih uspela. Nemam inspiraciju da pišem, kad se obogatim sešćemo kao ljudi.

RESUMO

Nossa sociedade moderna se encontra em um constante crescimento e desenvolvimento, o que torna inevitável o aumento da demanda por energia, alimento, medicamentos e qualidade de vida. Um ponto em comum entre inúmeras aplicações na área de saúde, bem-estar e inúmeros processos industriais reside na quantificação de espécies moleculares de interesse. Neste sentido, o desenvolvimento de sensores tem se tornado indispensável para o mundo moderno. Dentre os sensores químicos, o subgrupo dos sensores eletroquímicos conquistou espaço nos últimos anos por conta de sua versatilidade, simplicidade em termos de arranjo experimental, além do baixo custo. A eficiência dos sensores depende do potencial de um material ativo que será acoplado a um transdutor. Desta maneira, polímeros de coordenação eletroativos como o azul da Prússia, com suas propriedades estruturais e redox bem conhecidas, têm sido explorados para essa aplicação, com resultados excepcionais. Em sua forma reduzida, o azul da Prússia possui uma interessante atividade catalítica, capaz de reduzir peróxido de hidrogênio com alta velocidade reacional e baixo sobrepotencial. Desta maneira, podem ser vistos como “peroxidases artificiais”.

Neste projeto, estudamos principalmente o desenvolvimento de sensores eletroquímicos e o azul da Prússia foi usado como camada eletroativa. Também realizamos a modificação de diferentes substratos convencionais, como ouro, platina, carbono vítreo, e eletrodos impressos. Além disso, técnicas modernas de impressão 3D foram utilizadas para a criação de eletrodos 3D de grafeno condutivo, os quais também foram modificados com azul da Prússia. O estudo eletroquímico comparativo entre substratos convencionais e os impressos em 3D modificados com azul da Prússia também foi realizado. Comparamos o azul da Prússia e seu análogo, amino azul da Prússia, para a modificação de eletrodos impressos. Além disso, o comportamento redox do azul da Prússia e a eletro-oxidação do eletrodo de grafeno impresso em 3D foram estudados *in situ* por espectroeletroquímica Raman. Por fim, apresentamos em detalhes a construção de um fotoreator e sua aplicação em síntese fotoquímicas de nanomateriais como o azul da Prússia e nanopartículas de ouro e exploramos também o controle do grau de redução de óxido de grafeno.

ABSTRACT

Our society is in a constant state of growth and development and it is inevitable that demands for energy, food, medicine and welfare will increase. A common point in both human health and industrial processes is information related to quantification of the molecules. In this sense, the development of sensors becomes essential in the modern world. The subgroup of chemical sensors - electrochemical sensors through years have earned special place, because of their remarkable detectability, experimental simplicity and low cost. The efficiency of the sensors depends on a potential active material that will be coupled with transducer. Thus, electroactive coordination polymers such as Prussian blue with its well knowns structural and redox properties has been applied for this purpose and shown remarkable results. In its reduced form Prussian blue has strong catalytic activity to reduce hydrogen peroxide at very fast catalytic rate and with a low overpotential, thus is referred as an “artificial peroxidase”.

During this this project we have been mainly focused on electrochemical sensors and Prussian blue was used as electroactive layer. Modification of different substrates, the traditional ones such as gold, platinum, glassy carbon and screen – printed electrodes was performed. In addition, remarkable 3D printing technologies were used for the creation of 3D conductive graphene electrodes which were also modified with Prussian blue. The comparative electrochemical studies between Prussian blue modified traditional substrates and 3D electrode were conducted. Also, between Prussian blue and its analogue Prussian blue - Ammine using screen printed electrode. Then, redox behaviour of Prussian blue and electro-oxidation of graphene 3D electrode were studied with *in situ* Raman spectroelectrochemistry. Lastly, the construction of lab-made photoreactor was presented in detail and tested for the synthesis of gold nanoparticles and reduction of graphene – oxide.

FIGURES LIST

TABLES LIST

Summary

Chapter 1

Overall introduction

1.1 Sensors

Our society is in a constant state of growth and development and it is inevitable that demands for energy, food, medicine and welfare will increase. The advances obtained are a consequence of the human and industrial development, and with tireless search for improvement for the quality of life. A common point in both human health and industrial processes is information related to quantification of the molecules. In this sense, the development of sensors becomes essential in the modern world.

A sensor is defined as a device which produces a measurable output in a response to a known stimulus [1].The output signal should be proportional to the input signal. In general, sensors are divided into: physical sensors (measuring physical properties such as temperature, pressure, flow, stress, position, etc.) and chemical sensors. Chemical sensors are devices were inputs (chemical information such as composition, presence of specific ions or a concentration) are transformed into an an alytically useful signal. A typical chemical sensor consists of a receptor and a transdu cer coupled with active sensing materials [2,3]. Chemical sensors can be classified according to the operating principle of the transducer [4].

Eelectrochemical transducers are used in fabrication of electrochemical sensors, where the analyte concertation is proportional to recorded electrical signal [2,5]. In Figure 1 the principal stages of the electrochemical sensors are presented. Electrochemical sensors have attracted special attention, because of their remarkable detectability, experimental simplicity and low cost [6].

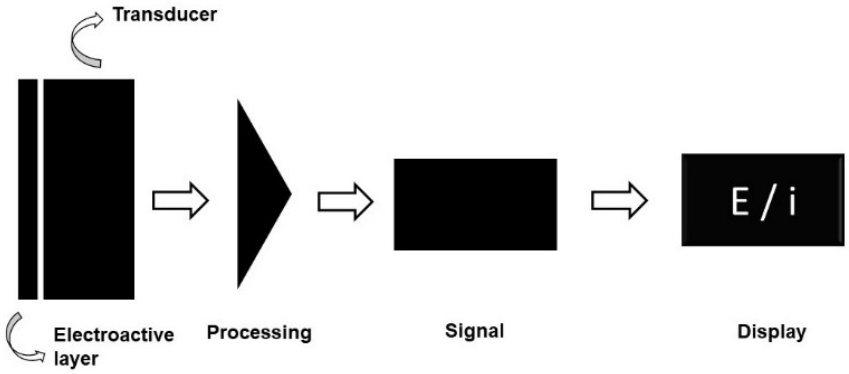

Figure 1: Principal stages in the operation of an electrochemical sensor. Adapted from[5].

The efficiency of the sensors depends on the selection and development of potential active materials. In this sense, electroactive coordination polymers such as Prussian blue have been applied and shown remarkable results [7].

1.2 Prussian blue

Prussian blue is the first synthetic coordination polymer compound reported in the literature [8]. Its crystal structure is face-center cubic where alternating Fe^{III} and Fe^{II} are bridged *via* cyan ligands [9]. The lattice is constructed in such a way, that each Fe^{III} ion is surrounded octahedrally with nitrogen atoms, and each Fe^{II} ion is surrounded by carbon [10], Figure 2.

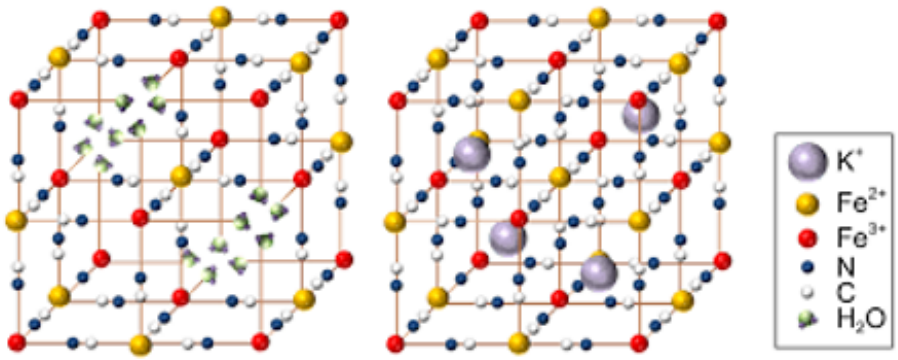

Figure 2: The crystal structure of Prussian blue, (left) insoluble form, (right) soluble form [11].

Its zeolitic structure, with a cubic unit cell of 10.2 Å and channel diameters of 3.2 Å allows the diffusion of low molecular weight molecules (O_2 and H_2O_2), thus turning Prussian blue into a three - dimensional catalyst [12]. Based on the powder diffraction patterns it is possible to distinguish two forms of Prussian blue, the “soluble” and “insoluble”, (Figure 2). Theses terms do not refer the real solubility in water, because both are highly insoluble ($Kps=10^{-40}$). In “soluble form” Prussian blue, half of cavities are usually occupied by alkali metal ions such as K^+ or Na^+. In insoluble form ($Fe^{III}_4[Fe^{II}(CN)_6]_3 . xH_2O$) the interstitial water molecules are found in the framework, which cause some structural defects [12,13].

Prussian blue has a well - known redox behavior with two set of peaks, Figure 3. In between the two observed peaks the oxidation state corresponds to the Prussian blue with basic unit of $[Fe^{III} Fe^{II}(CN)_6]^-$ [14]. Its reduction is followed with color loss, and the reduced form is denoted as Prussian white, with basic unit of $[Fe^{II} Fe^{II}(CN)_6]^{2-}$. In its oxidized form is known as Berlin green with basic unit of $[Fe^{III} Fe^{III}(CN)_6]$. The oxidation of Prussian white to Prussian blue occurs at potentials close to 0.2 V *vs* Ag/Ag/Cl, whereas oxidation of Prussian blue to Berlin green occurs at potentials close to 0.9 V *vs* Ag/Ag/Cl, as it can be seen from Figure 3 [13].

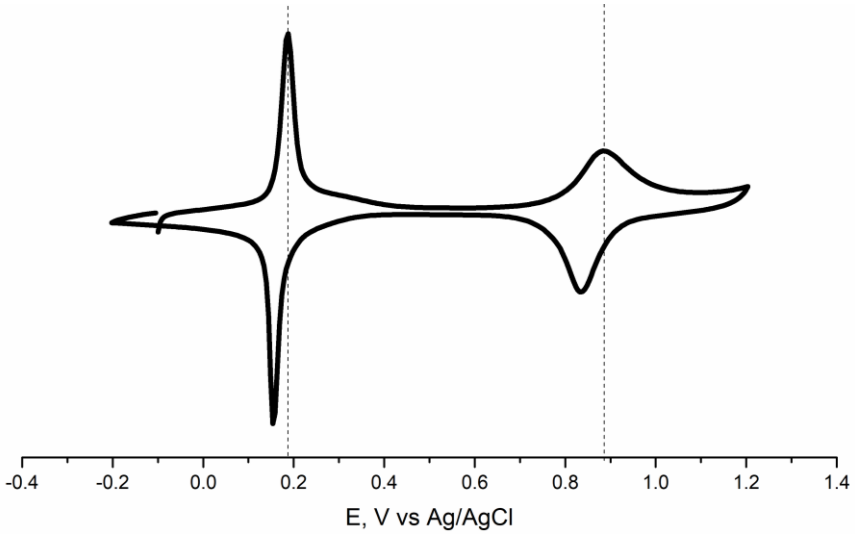

Figure 3: Cyclic voltammogram of Prussian blue modified glassy carbon electrode in 0.1 mol L-1 HCl/KCl at 50 mV s^{-1}.

The reduction and oxidation of reaction for “soluble” and “insoluble” form are shown in Eq (1-4) [15].

$$\mathbf{KFe^{III}Fe^{II}(CN)_6 + K^+ + e^- \rightarrow K_2Fe^{II}Fe^{II}(CN)_6} \quad (1)$$

$$\mathbf{KFe^{III}Fe^{II}(CN)_6 \rightarrow Fe^{III}Fe^{III}(CN)_6 + e^- + K^+} \quad (2)$$

$$\mathrm{Fe_4^{III}[Fe^{II}(CN)_6]_3 + 4K^+ + 4e^- \rightarrow K_4Fe_4^{II}[Fe^{II}(CN)_6]_3} \quad (3)$$

$$\mathrm{Fe_4^{III}[Fe^{II}(CN)_6]_3 + 3Cl^- \rightarrow Fe_4^{III}[Fe^{III}(CN)_6]_3\,Cl_3 + 3e^-} \quad (4)$$

The soluble Prussian blue form is generated by successively cycling freshly electrodeposited Prussian blue between the potential range from -0.2 V to + 0.60. During this process the Fe^{III} ions are replaced with potassium ions. In addition, the interstitial water is lost during the process and electrochemical repose of “soluble” Prussian blue films is different when compared to “insoluble”. When converted “soluble” Prussian blue films are electrochemically stable and can be cycled reversible between Prussian blue/Prussian white forms [12,14].

As a result of its structural and redox properties Prussian blue has been subject of many studied in application in many fields, especially in sensing applications [12]. As an active component Prussian blue has been used for sensing variety of analytes
such as: cholesterol[16], hydrazine[17], morphine[18] and mostly H_2O_2 [19,20]. In its r educed form, Prussian white has a catalytic activity to reduce H_2O_2 and is known as “artificial peroxidase”.

1.2.1 Hydrogen peroxide sensors

Hydrogen peroxide (H_2O_2) is a valuable marker for oxidative stress and is recognized as one of the major risk factors in progression of pathophysiological complications in diabetes, atherosclerosis, renal disease, cancer, and aging [21]. In addition, H_2O_2 is a product of enzymatic reactions catalyzed by oxidases and its concentration in serum is directly proportional to the concentration of diverse biomole cules such as glucose, cholesterol, lactate, urate, and glutamate [22].

Briefly, the oxidase enzymes act by oxidising the substrate and afterwards return to original active state by transferring electrons to molecular oxygen. The final product of these enzymes are the oxidized forms of the substrate and H_2O_2 as a side product [12]. The H_2O_2 production can provide information's linked directly to the initial concentration of substrate. However, its high overpotential (ca. 0.7 V *vs* Ag/AgCl), at which many electroactive substances (i.e. ascorbic acid, uric acid, etc.), can oxidize and act as interfering agents is a main drawback. A strategy used to avoid this problem is to use a redox mediator system to promote the reduction of hydrogen peroxide such as horseradish peroxidase (HRP) is an enzyme that catalyse this reaction and has been used with this function, however its high cost, low stability and poor binding to the surface of substrates limit its use [7].

In this sense, Prussian blue has the advantages due to its low cost, easy preparation methods and possibility of modification of many different substrates. A typical scheme of a Prussian blue biosensor is shown in Figure 4.

In 1984 Itaya et al. [23] has demonstrated that in its reduced form has a catalytic effect for the reduction of oxygen and hydrogen peroxide. In addition, in its oxidized form Prussian blue has catalytic activity towards the oxidation of hydrogen peroxide. This catalytic behavior has been ascribed to the specific structure of Prussian blue. As it has been explained, its zeolitic nature allows the diffusion of small molecules such as molecular oxygen and hydrogen peroxide.

Even though, the catalytic mechanism towards the hydrogen peroxide is not clear, according to the Itaya hypothesis when H_2O_2 penetrated inside the Prussian blue structure, it will be in the center of each vacancy and surrounded by four high spin iron ions, which can further catalyse reduction *via* a four - electron reaction [12].

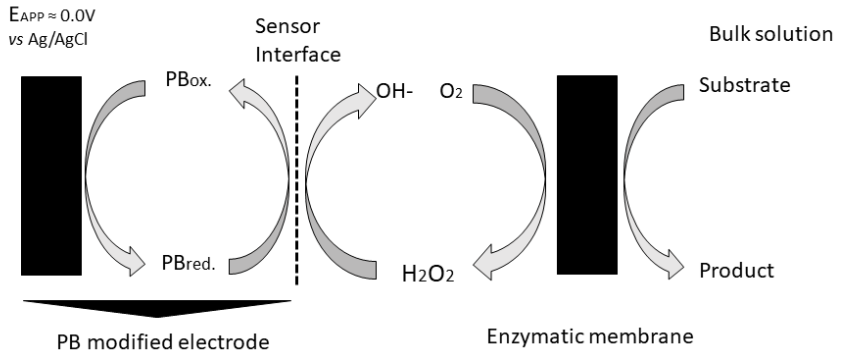

Figure 4: Scheme for Prussian blue - based biosensor with an oxidase enzyme. Adapted from [12].

Over the years Prussian blue has been successfully deposited over the surface of various substrates (platinum electrode [24], glassy carbon [25] fluorine doped tin oxide (FTO) [26] and used for the detection of H_2O_2. Carbon based materials are frequently employed as support for the immobilization of Prussian blue because of their mechanical properties, high conductivity and high surface area [7,27].

Recently, BlackMagic 3D company have successfully incorporated graphene into the conductive filament and have enabled this remarkable material to be coupled with revolutionary 3D printing technologies.

1.3 3D printing technologies

3D printing also known as addictive manufacturing is used for the fabrication of variety of structures and complex geometries based on digitally controlled deposition of successive layers of materials until the desired object is created [28].

On contrary, subtractive manufacturing – the traditional one, is a process where 3D objects are constructed by successively cutting material away from a solid block of material. From practical point of view both techniques are valid methodologies. The choice depends on the material to be employed because the additive manufacturing is generally used for plastic – based object, and subtractive manufacturing is suitable for wooden – based objects [29]. However, with addictive manufacturing is possible to reduce energy costs and waste. The comparison between the two fabrication techniques is shown in Figure 5.

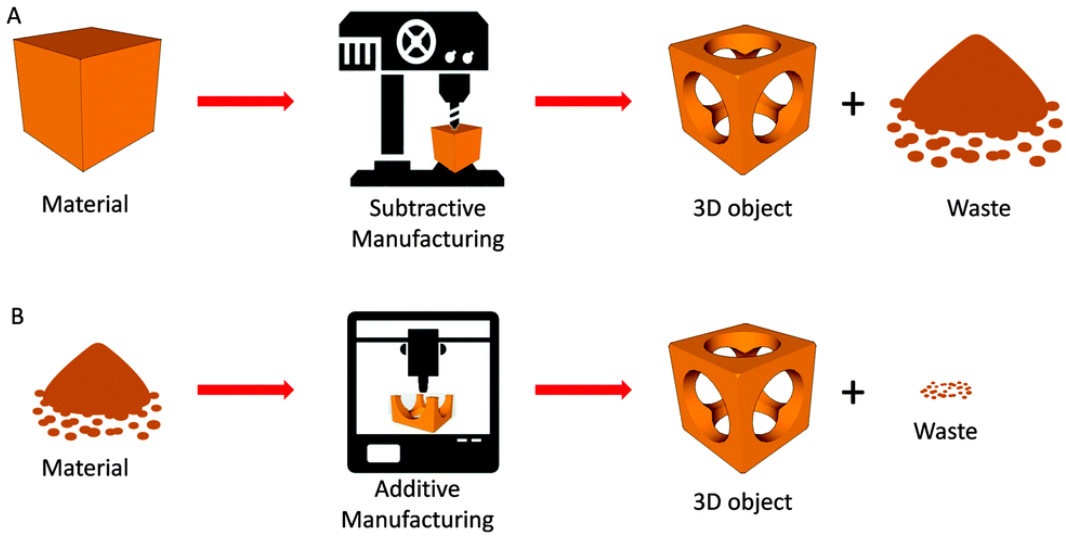

Figure 5: Comparison between A) addictive manufacturing and B) subtractive manufacturing [28].

The creation of a virtual model to be printed is the first step using computer-aided design (CAD). Nowadays there are numerous free online website available, simple to use where users can design their desired objects. The 3D object should be converted to STL (STL standing for STereoLithography) file, which contains information's about the model surface, and this extension is universally recognized by almost all 3D software's. When uploaded to the 3D software STL file is then "sliced" or converted to G – code. During the "slicing" procedure several 2D cross section layers of object are generated. The printer follows the sequence of these layers, which are build one on the top of the other until the 3D desired object is finally created [28,30]. The 3D printing process from the creation of the desired model using designing software till the printing of the final object is presented in Figure 6.

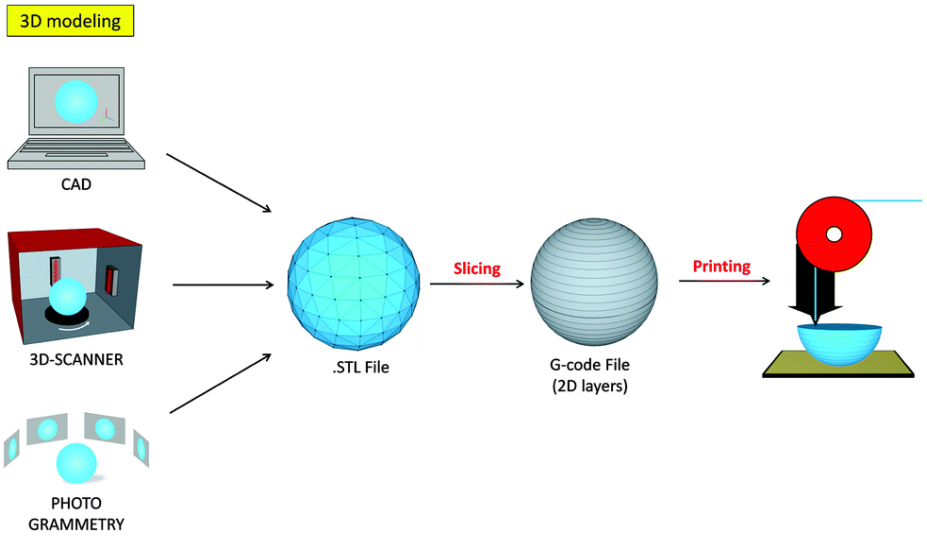

Figure 6: 3D printing process from object design to the printing process [28].

The most commonly employed 3D printing technique is fused deposition modeling (FDM). It is based on 3D printing process known as extrusion and materials to be used are usually thermoplastics such as acrylonitrile butadiene styrene (ABS) and polylactic acid. However, with powder - based technique is possible to created metallic 3D objects [31].

In its nutshell, FDM produces 3D models by depositing layer - by - layer thermoplastic material that has been previously heated to semi-molten state before extrusion from the nozzle. When deposited, material solidifies creating hard, uniform layer upon which next layer stacks. The FDM is the most common 3D printing technology because it is quite simple to use, and the 3D printers are available at low price [28,32].

In last few years, 3D printing technologies have found applications in variety of fields [33,34]. In addition, electrochemistry can also benefit from 3D printing especially because there is a possibility to design and create conductive electrodes at much lower price compared to the traditional electrodes available in the market today.

1.4 Motivation and the structure of thesis

Considering the great importance in quantification of the molecules, the sensors have emerged as leading devices and Prussian blue based materials have found important role as electroactive layers. Recently, we have acquired 3D printed in

our laboratory. Thus, we were able to combine all of this and we have been motivated and driven to create this work. The thesis is divided into five chapters. The first chapter is an overall introduction, afterwards each chapter consisting of either articles that have already been published or submitted ones.

In second chapter of this thesis four different substrates were used and modified with Prussian blue. Focus of this chapter is 3D printed graphene - based electrode, therefore its detailed spectroscopic characterization was performed. In addition, the electrochemical behaviour of Prussian blue modified 3D electrode was compared with traditional electrodes (gold, platinum and glassy carbon). The Prussian blue modified 3D printed electrodes have been investigated in the electrocatalytic reduction of H_2O_2.

The third chapter of this thesis has explored modification of screen - printed electrodes with Prussian blue and its analogues Prussian blue – Ammine. Comparative studies between two deposition methods were performed. Modified electrodes were electrochemically characterized and were employed toward the sensing of cysteine.

In fourth chapter, the 3D printed electrode based on conductive graphene a was modified with Prussian blue. In addition, the spectroelectrochemical cell was printed using ABS filament. The modified electrode was studied with *in situ* Raman spectroelectrochemistry. The bare 3D electrode was also submitted to *in situ* electrochemical oxidation.

The fifth chapter describes in detail the construction of a lab-made photoreactor. The proposed lab-made photoreactor was used for the synthesis of the gold nanoparticles and reduced graphene oxide. The gold nanoparticles synthesized using photochemical way were initially planned to be the focus of this thesis. The main idea was to obtain gold nanoparticles with different shapes using lab-made photoreactor. However, we were limited with the availability of essential characterization technique - scanning electron microscopy to follow the shape evolution and alteration.

Chapter 2

3D printed graphene electrodes modified with Prussian blue: Emerging electrochemical sensing platform for peroxide detection

2.1 Introduction

3D printing also known as additive manufacturing constructs three dimensional objects by depositing layer by layer build material, digitally coordinated [35]. This emerging technology has proven to ease manufacturing of materials and is

more advantageous compared to the subtractive manufacturing providing freedom of design, waste minimization and fast prototyping [28]. In contrast to traditional fabrication processes where predetermined molds are used and are optimized for large-volume production of identical objects, 3D printing provides significant flexibility with possibility to create unique objects tailored to a specific application [36]. Therefore, with its versatility 3D printing has proven to be useful technology for specialized applications in industry and for scientific research. Especially in field of electrochemistry since, 3D-printing technologies potentialize the fabrication of electrodes in large-scale for sensing applications [37].

For sensing applications, the carbon materials are preferred substrates since they offer greater stability and broader potential window [38]. Among carbon materials, graphene materials are highlighted and extensively studied in the field of electrochemistry due to their fascinating physical and electrochemical properties [2 7]. For electrochemical applications, the presence of oxygenated functional groups is essential. Thus, functionalization of graphene sheets has a great importance in electr ocatalytic sensing applications [39]. In this sense, our group has studied the influence of various applied potential of 3D printed graphene electrode and used for sensing of dopamine [40]. In addition, the surface functionalization allows electrocatalysts such as Prussian blue to be anchored on to the surface of 3D printed graphene electrodes.

Prussian blue and its analogues belong to the group of transition-metal hexacyanometalates with a face-centered cubic lattice with open, zeolite-like structure [41]. Prussian blue has attracted attention because of its remarkable magnetic, electrochromic, and electrochemical properties [41,42]. In addition, due to its high activity and good selectivity towards the reduction of hydrogen peroxide Prussia n blue is usually considered as “artificial” peroxidase [43]. The good selectivity toward s the reduction of hydrogen peroxide can be attributed to its structure, which only allo ws small molecule (such as H_2O_2) to diffuse into the lattice and to be reduced, thus decreasing the number of potential molecules that could interfere [12,14].

However, low stability in neutral media and poor conductivity of Prussian blue are obstacles for its efficient use in sensing applications [41]. To overcome these obstacles, a series of conductive supports have been used to enhance its conductivity.

Among support materials, carbon - based materials have demonstrated to provide better electrochemical stability and electrical conductivity [22].

In this work, Prussian blue films were electrodeposited onto the surface of 3D printed graphene electrode. In addition, the Prussian blue was also electrodeposited onto the surface of gold, platinum and glassy carbon electrode. The modified 3D printed electrode has larger surface area when compared to others and has shown to be more stable in acidic and neutral pH, when compared to gold and glassy carbon electrodes. The 3D modified electrode has been also investigated in electrocatalytic reduction of H_2O_2.

2. Experimental section

2.1 Modification of the electrodes

Prior to the modification, gold (Au), glassy carbon (GCE), and platinum (Pt) electrodes were carefully polished successively with 1.0, 0.5 and 0.3 μm alumina, sonicated in ethanol: water for 10 min and rinsed with Milli-Q water. 3D-printed graphene electrodes were fabricated and submitted to an electrochemical pre-treatment, based on our previous report [40]. Briefly, the surface of working electrode was oxidized (applying potential of 1.8 V *vs* Ag/AgCl for 15 minutes), and then reduced (by applying potential of -1.8 V *vs* Ag/AgCl for 50 seconds). Prussian blue films were electrodeposited by applied potential of 0.4 V *vs* Ag/AgCl for 600 s in a solution containing 1.0 x 10^{-3} mol L^{-1} $[Fe(CN)_6]^{3-}$, 1.0 x 10^{-3} mol L^{-1} $FeCl_3$, 0.01 mol L^{-1} HCl and 0.01 mol L^{-1} KCl. After, the modified electrodes were electrochemically activated by applying 25 voltammetric cycles from -0.2 to 0.6 V vs Ag/AgCl in a solution of 0.1 mol L^{-1} HCl containing 0.1 mol L^{-1} KCl at 50 mV s^{-1}. Then, the films were dried in an oven at 60 °C for 2 h.

2.2 Characterization

The bare and modified 3D-printed graphene electrode were characterized by Infrared, Raman, X-ray photoelectron spectroscopies. Fourier-transform infrared (FTIR) spectra were recorded on a portable Agilent Cary 630 ATR-FTIR analyzer, in the range of 450 to 4000 cm^{-1}. Raman spectra of the electrodes were performed on a

Confocal T64000 spectrometer from Jobin Yvon with a solid-state sapphire laser (532 nm, 10 mW), with an integration time of 20 s and a 100x LWD objective in the range of 1000-2400 cm^{-1}. X-ray photoelectron spectroscopy (XPS) measurements were performed with a VSW HA-100 spherical analyzer and AlKα radiation ($h\nu$ = 1486.6 eV). The high-resolution spectra were measured with constant analyzer pass energies of 44eV producing a full width at half-maximum (FWHM) linewidth of 1.6 eV for the Au ($4f_{7/2}$) line. The pressure during the measurements was always less than 6×10^{-8} mbar. The sample was fixed to a stainless-steel sample holder with double-faced conducting tape and analyzed without further preparation. Surface charging was corrected shifting all spectra so that the highest binding energy component of the PLA was at 289.06 eV [44]. Curve fitting was performed using Gaussian line shapes, and a Shirley background was subtracted from the data. The morphologies of the 3D-printed graphene electrodes before and after the electrodeposition of Prussian blue were investigated by FEI Quanta 250 field emission scanning electron microscope (FE-SEM) from FEI Co., USA, operating at 2.0 kV.

2.3 Electrochemical characterization of the electrodes

Cyclic voltammetry (CV) measurements were performed on an AUTOLAB modular electrochemical system (ECO Chemie, Utrecht, Netherlands) equipped with a STAT 12 module and driven by Nova 2.1 software in conjunction with a conventional three-electrode electrochemical cell and a personal computer for data storage and processing. Glassy carbon, gold, platinum or 3D-printed graphene electrodes were employed as working electrode (bare or modified); Ag/AgCl (in KCl 3.0 mol L^{-1}) as reference electrode, a Pt wire as the counter electrode. Cyclic voltammetry studies were performed in 0.1 mol L^{-1} KCl containing 5.0 mmol L^{-1} of $[Ru(NH_3)_6]^{2+/3+}$ at different scan rates to determine the electrochemical surface areas and the heterogeneous electron transfer rates (k^0) of the bare and modified electrodes. All electrochemical measurements were performed at room temperature.

The electroactive areas (A_e) of the electrodes were determined by cyclic voltammetry in 5.0 mmol L^{-1} of $[Ru(NH_3)_6]Cl_3$ and 0.1 mol L^{-1} KCl at different scan rates, according to the Randles-Ševčík equation [45], Eq. 5:

$$i_p = 2.69 \times 10^5 n^{3/2} A_e D^{1/2} C v^{1/2} \quad (5)$$

where i_p is the peak current, n is the number of electrons transferred in the electrochemical process, A_e is electrode area, *D* is the diffusion coefficient (9.10 x 10^{-6} cm^2 s^{-1} for $[Ru(NH_3)_6]^{3+}$ in 0.1 mol L^{-1} KCl), *C* is the concentration of the redox probe and v is the applied voltammetric scan rate.

In order to determinate the heterogeneous rate constants (k^0_{obs}) between the electrodes and $[Ru(NH_3)_6]^{3+/4+}$ probe, cyclic voltammograms in 5.0 mmol L^{-1} of $[Ru(NH_3)_6]Cl_3$ and 0.1 mol L^{-1} KCl at different scan rates were obtained, the constants were calculated using the Nicholson method [46,47] by the Eq. 6:

$$k^0_{obs} = \left[2.18\left(\frac{D\propto nFv}{RT}\right)^{1/2}\right] exp\left[-\left(\frac{a^2 nF}{RT}\right)\right] \Delta E_P \quad (6)$$

where D is the diffusion coefficient (9.10 x 10^{-6} cm^2 s^{-1} for $[Ru(NH_3)_6]^{3+}$), α is assumed to correspond to 0.5, n is the number of electrons transferred in the electrochemical process, F is the Faraday constant, v is the applied voltammetric scan rate, R is the gas constant, and T is the temperature of the solution and ΔE_p is peak-to-peak separation.

The electroactive surface coverage (Γ) and the thickness (*l*) of the PB film can be calculated according to Equations 7 and 8 [48] using the anodic current peak of the Prussian White (Fe^{2+}-Fe^{2+})/Prussian Blue (Fe^{2+}-Fe^{3+}) redox process. A plot of the anodic current peak as a function of the scan rate provides a linear correlation which slope provides the value of the Γ in mol m^{-2}

$$i_{pa} = \frac{n^2 F^2}{4RT} \Gamma v A \quad (7)$$

$$l = \Gamma\left(\frac{a^3 N_A}{4}\right) \quad (8)$$

where i_{pa} is the anodic peak current, *n* is the number of electrons involved in the redox process, F is the Faraday constant, *R* is the gas constant, *T* is the

temperature, Γ is the electroactive surface coverage, ν is the scan rate and A the electrode area, a is the unit cell parameter of Prussian Blue (1.01 nm), N_A is the Avogadro number.

2.4 H_2O_2 detection

Electrochemical detection of H_2O_2 was carried out in the same equipment with a conventional three-electrode electrochemical cell. Cyclic voltammetry measurements were performed from -0.2 V to 0.5 V *vs* Ag/AgCl, at a scan rate of 50 mV s^{-1}, upon successive addition of 0.5 mmol L^{-1} H_2O_2 stock solution, under N_2 atmosphere. Phosphate buffer solution (0.1 mol L^{-1}, pH 7.4) containing 0.1 mol L^{-1} KCl as supporting electrolyte.

3. Results and discussion

3.1 Electrochemical deposition of Prussian blue on 3D-printed electrode

3D-printed electrodes have been reported as a promising platform for sensing biomolecules. Moreover, according to our previous report, electrochemical pre-treatments creates oxygen functionalities, which allows anchoring of materials such as Prussian blue [49]. Additionally, the performance of PB modified electrodes increases when this material is combined with partially reduced graphene oxide, due to the synergist effect of the electrocatalytic activity of PB and the fast electron transfer rate kinetics of graphene [22]. Thus, considering many advantages cited above, we have electrodeposited PB on the pre-treated 3D-printed graphene electrode.

3.2 Morphology

The morphology of the 3D electrodes before and after modification with Prussian blue was investigated by FE-SEM, Figure 7. As it can bee seen from Figure 7-B, the surface of the pre-treated electrode has a more homogeneous and smoother surface than the as printed electrode, indicating that the electrochemical pre - treatment has removed a few layers of the polymeric surface exposing the bulk material, as already reported by [40]. The electrodeposition of Prussian blue onto the

surface of the electrochemically pre-treated graphene electrode produced nanocubes with an average length of 138 ± 73 nm that appeared to be anchored in the surface of the electrode.

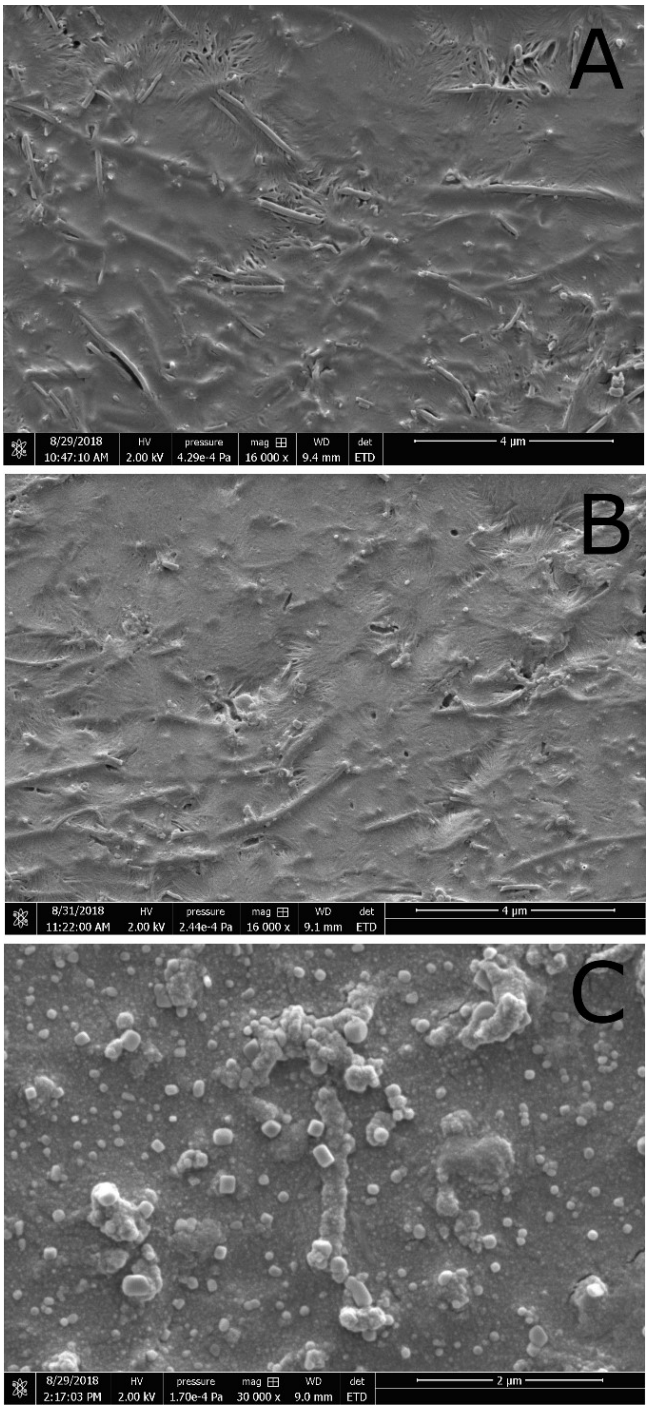

Figure 7: Field emission gun scanning electron microscopy (FEG-SEM) micrographs of A) as printed 3D electrode, B) the 3D graphene electrode submitted to oxidation (+1.8 V *vs* Ag/AgCl) followed by reduction (-1.8 V *vs* Ag/AgCl), C) the 3D

graphene electrode submitted to oxidation (+1.8 V *vs* Ag/AgCl) followed by reduction (-1.8 V *vs* Ag/AgCl) and afterwards modified with Prussian blue.

3.3 Spectroscopic characterization

XPS analysis provides information's related to materials chemical composition. XPS spectra of bare and modified 3D electrode are presented in Figure 8. The elemental percentage obtained from deconvoluted spectra are shown in Table 1. In comparison to the spectrum of 3D electrode before modification the presence of N and Fe elements clearly indicate formation of Prussian blue, Figure 8 A-B. The peak located at 707.8 eV can be attributed to the $Fe2p_{3/2}$ of $[Fe(CN)_6]^{4-}$ [50,51]. The N1s spectrum has two main peaks located at 397.04 eV and 398.38 eV corresponding to C-N of $[Fe(CN)_6]^{4-}$ [50].

The bare electrode shows peaks located at 289.1, 286.9, and 284.9 eV corresponding to the O-C=O, C-O-C, C-C/C-H, respectively, Figure 8-C. The modified electrode exhibits the same oxygen functionalities, Figure 8-D. The intensities have decreased probably because of reduction, and the peak located at 289.1 eV has shifted downwards to 288.7 eV, indicating the interaction of Prussian blue with graphene – based 3D electrode [51].The overall elemental content of O (atom %) was 33.81 for bare electrode and 15.05 after modification with Prussian blue, indicating that electrochemical pretreatment to some extent successfully removed oxygen – containing functional groups of 3D printed electrode.

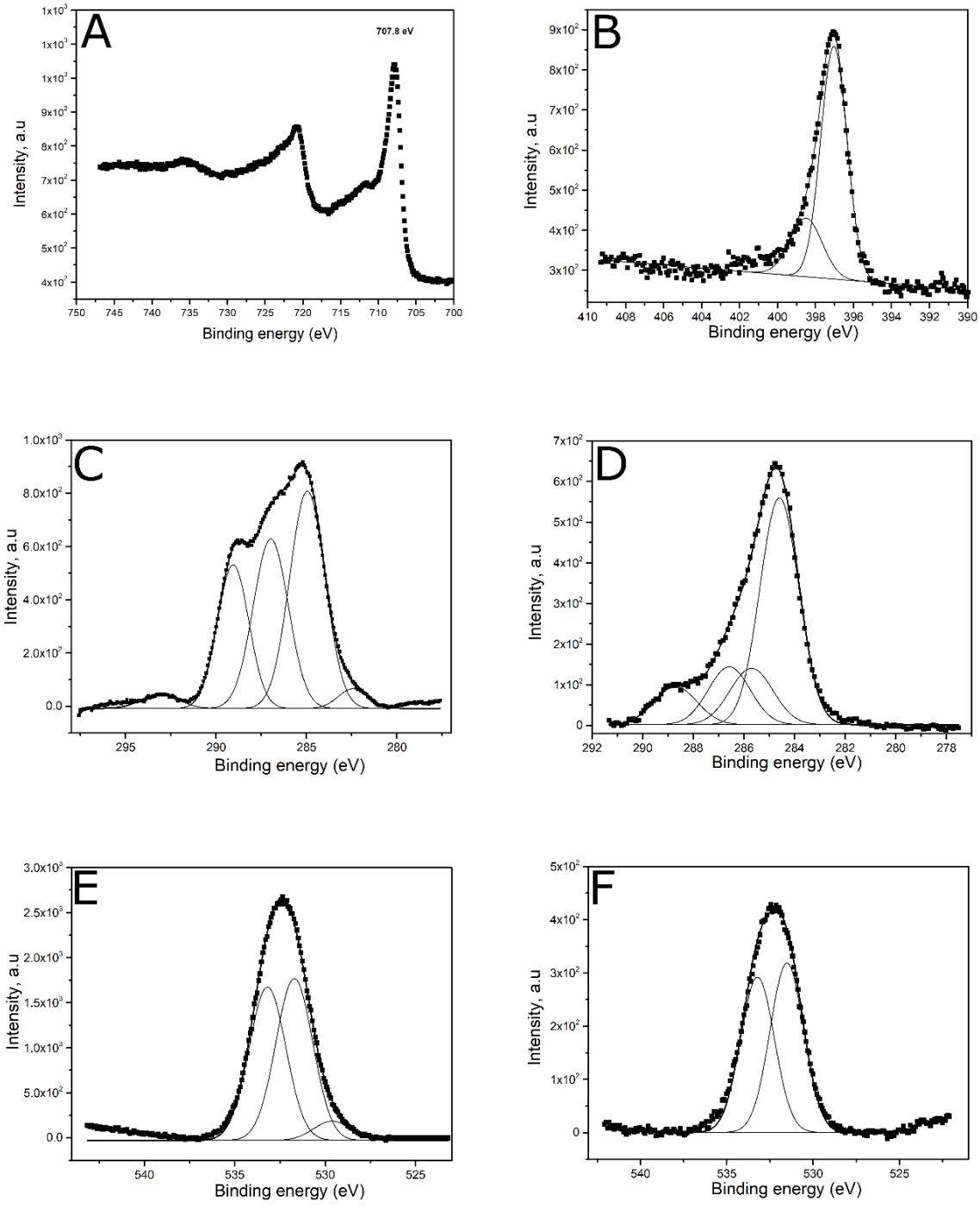

Figure 8: XPS spectra of bare and Prussian blue modified 3D electrode: A) Fe 2p spectrum of Prussian blue modified 3D electrode, B) N 1s spectrum of Prussian blue modified 3D electrode, C) C 1s spectrum of bare 3D electrode, D) C 1s spectrum of Prussian blue 3D modified electrode, E) O 1s spectrum of bare 3D electrode F) O 1s spectrum of Prussian blue modified 3D electrode.

Table 1: XPS data obtained from deconvoluted spectra of the bare and Prussian blue modified 3D printed graphene electrodes.

Electrode	% Elemental Atom C1s	% Elemental Atom O1s	% Elemental Atom Fe2p	% Elemental Atom N1s
3D	66.18	33.81	-	-
3D_PB	58.39	15.05	4.30	22.24

FTIR and Raman spectra of the as printed (3D), electrochemically pre-treated (3D_Bare) and Prussian blue modified 3D-printed graphene electrodes (3D_PB) are presented in Figure 9. A characteristic band of Prussian blue, attributed to ν(C≡N), can be observed close to the 2150 cm^{-1} in Raman and IR spectra. The spectra also presented bands associated to PLA, the complete attribution of these bands is presented in Table 2.

The bands D and G in Figure 9-B are assigned to vibrational modes of the graphene network and the ratio of its intensities (I_D/I_G) is proportional to the number of structural defects in the graphene sheet [52]. The calculated I_D/I_G ratios of 3D, 3D_Bare and 3D_PB were 0.64, 1.53 and 0.73, respectively, indicating the increases in the amount of defects/disorder upon insertion of oxygenated groups. Moreover, after the modification, the number of defect sites decreases, because its covered with PB particles, which alter the electronic structure and the density of states (DOS) of the graphene network.

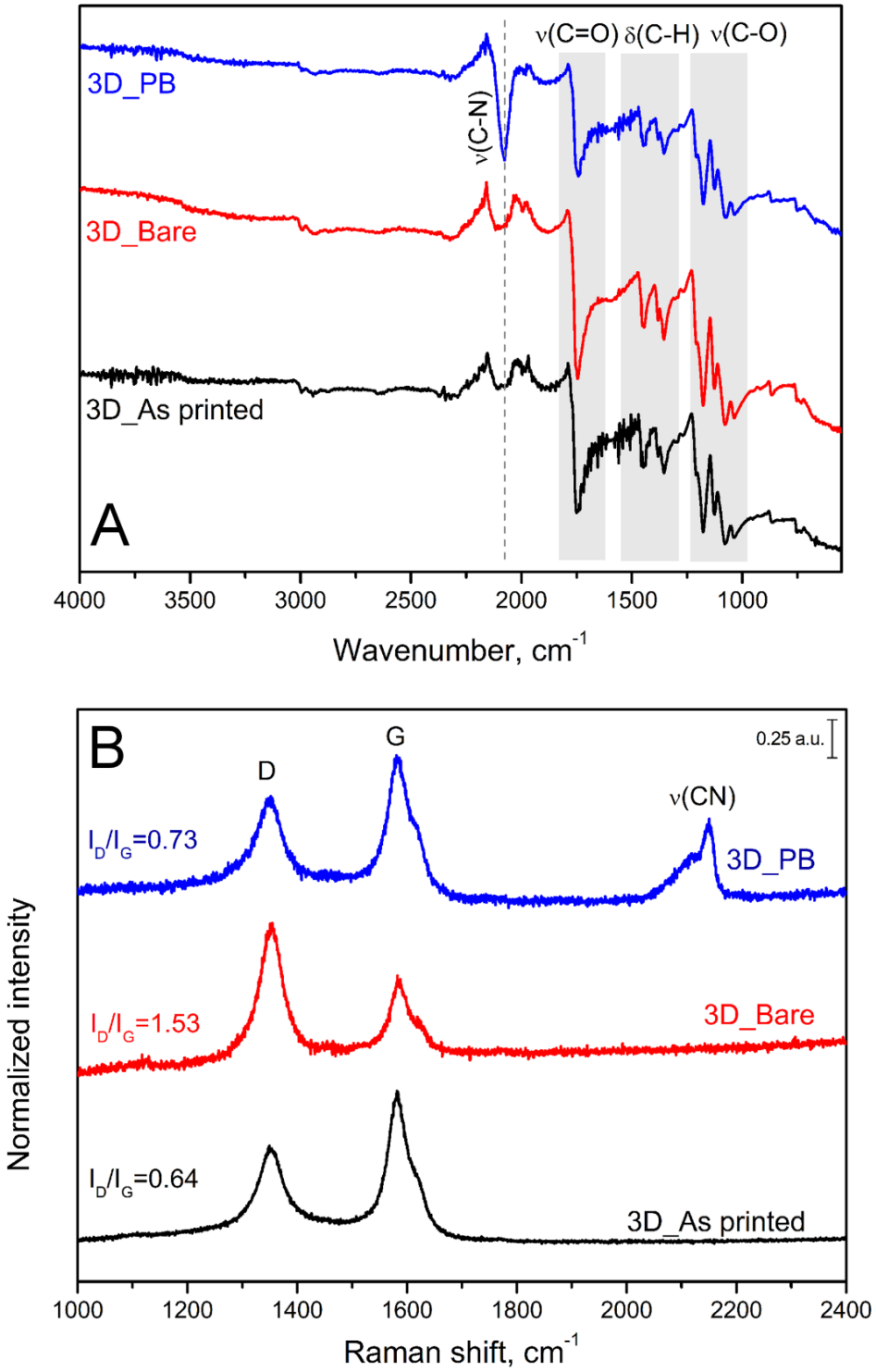

Figure 9: A) FTIR and B) Raman spectra and I_D/I_G ratio of the 3D-printed electrodes: as printed, bare and modified with PB.

Table 2: Infra-red spectrum of as printed (bare) 3D electrode and band attribution.

Wavenumber, cm^{-1}	Attribution

2989-2945	CH_3 antisymmetric and symmetric stretching
1752	C=O stretching
1453	CH_3 antisymmetric bending
1379 – 1349	CH deformation and symmetric bending
1178	C-O-C stretching
1079	C-O-C stretching
1039	C-O-C stretching

3.4 Electrochemical properties

Electrochemical properties of the electrochemically deposited PB films on 4 different substrates were studied by cyclic voltammetry. The cyclic voltammograms in 0.1 mol L^{-1} HCl/KCl (pH 1.0) of modified 3D, GCE, Au, Pt electrodes are presented Figure 10.

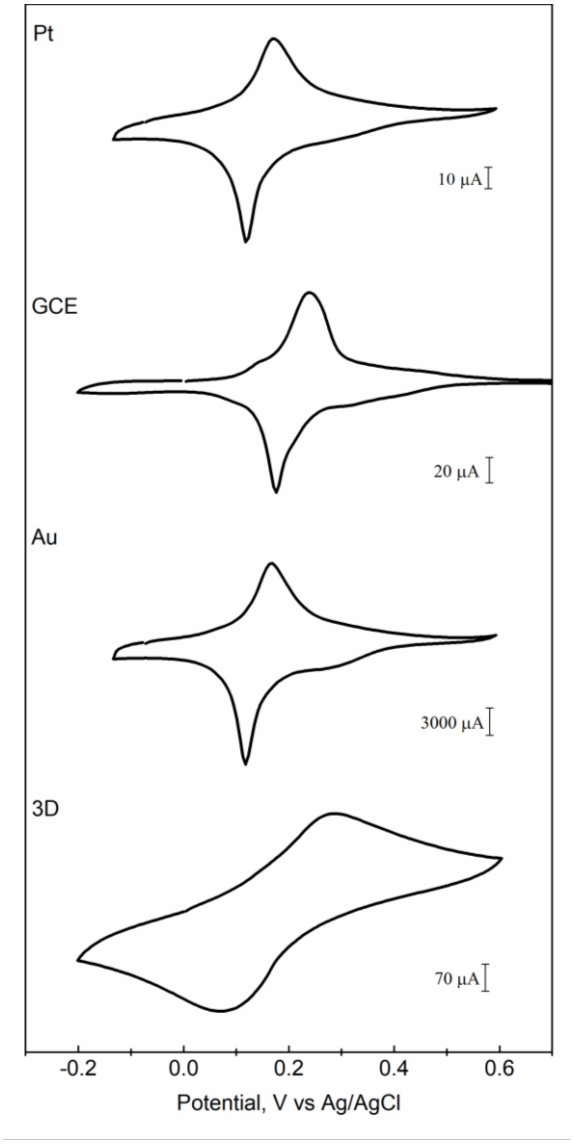

Figure 10: Comparison between the cyclic voltammograms of the Prussian blue modified electrodes in 0.1 mol L^{-1} HCl/KCl (pH 1) at 50 mV s^{-1}.

As shown in Figure 10 a pair of redox peaks appeared at E° approximately of 0.20 V *vs* Ag/AgCl, ascribed as the redox processes of Prussian blue and Prussian white.

The cyclic voltammograms of the Prussian blue modified 3D, Au, GCE and Pt in 0.1 mol L^{-1} HCl/KCl at different scan rates are shown in Figure 11-14, with corresponding electrochemical parameters presented in Table 3.

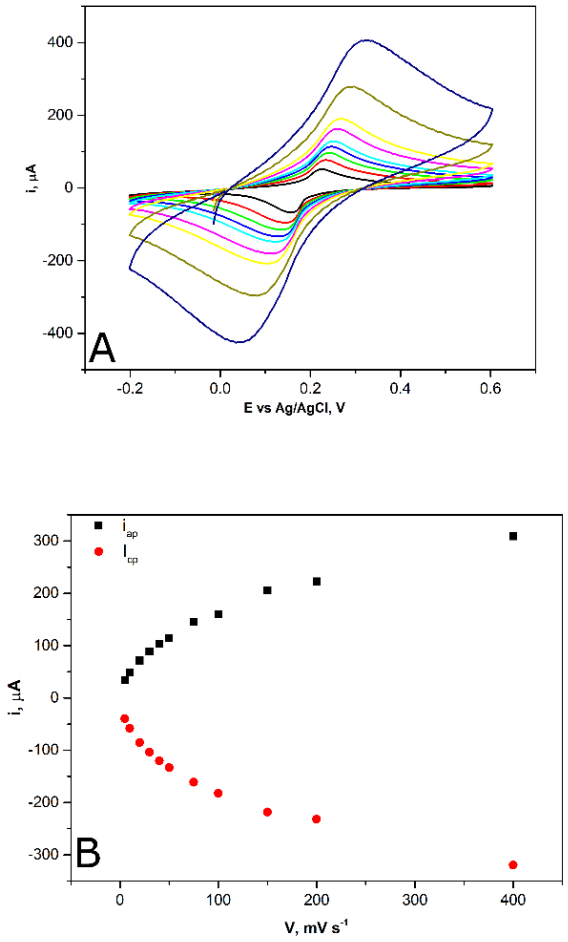

Figure 11: A) Cyclic voltammogram of 3D electrode modified with Prussian blue at different scan rates, B) The dependence of peak currents on the scan rates. The experiments were performed in 0.1 mol L^{-1} HCl and 0.1 mol L^{-1} KCl.

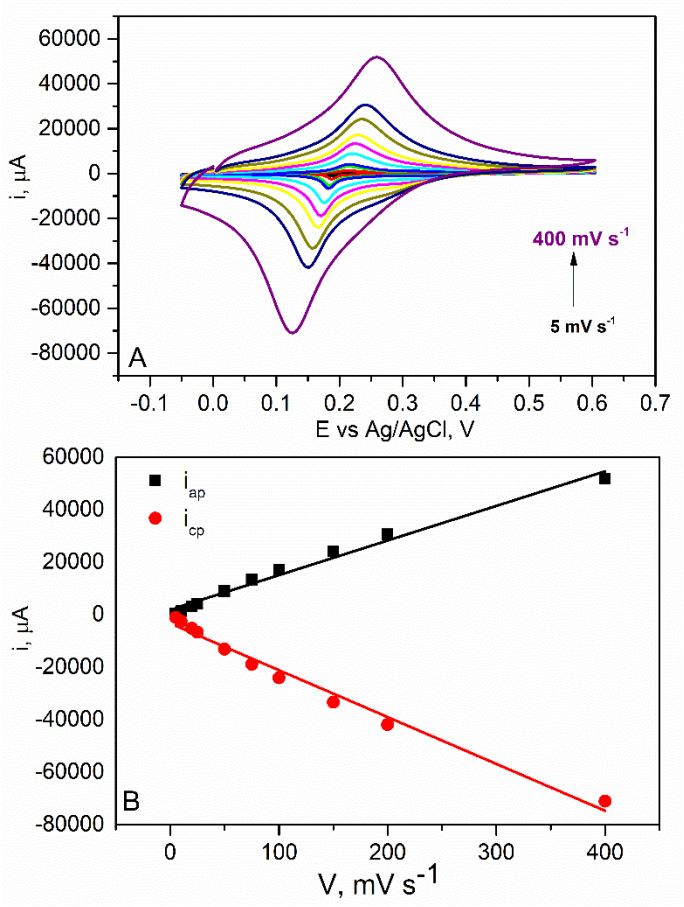

Figure 12: A) Cyclic voltammogram Au electrode modified with Prussian blue at different scan rates, B) The dependence of peak currents on the scan rates. The experiments were performed in 0.1 mol L^{-1} HCl and 0.1 mol L^{-1} KCl.

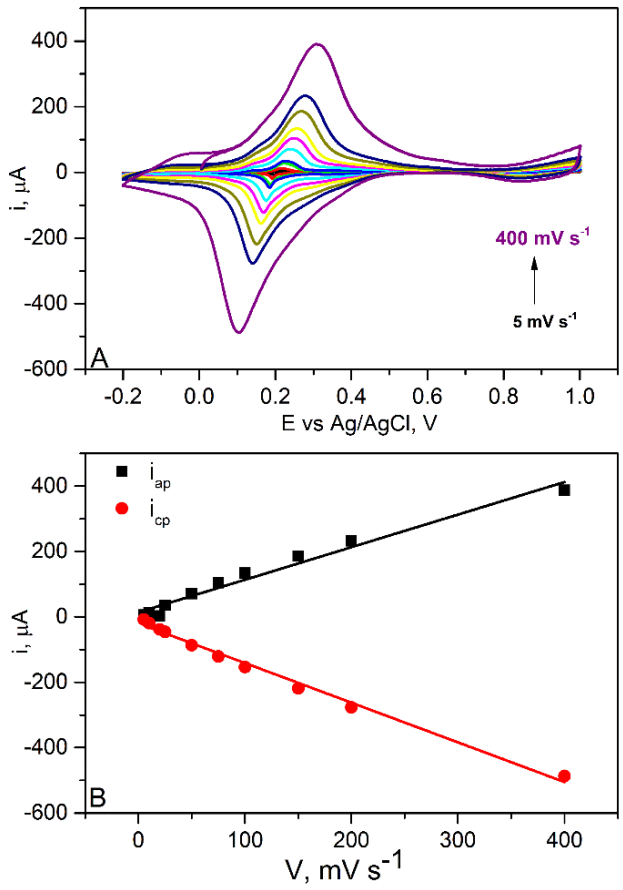

Figure 13: A) Cyclic voltammogram GCE electrode modified with Prussian blue at different scan rates, B) The dependence of peak currents on the scan rates. The experiments were performed in 0.1 mol L^{-1} HCl and 0.1 mol L^{-1} KCl.

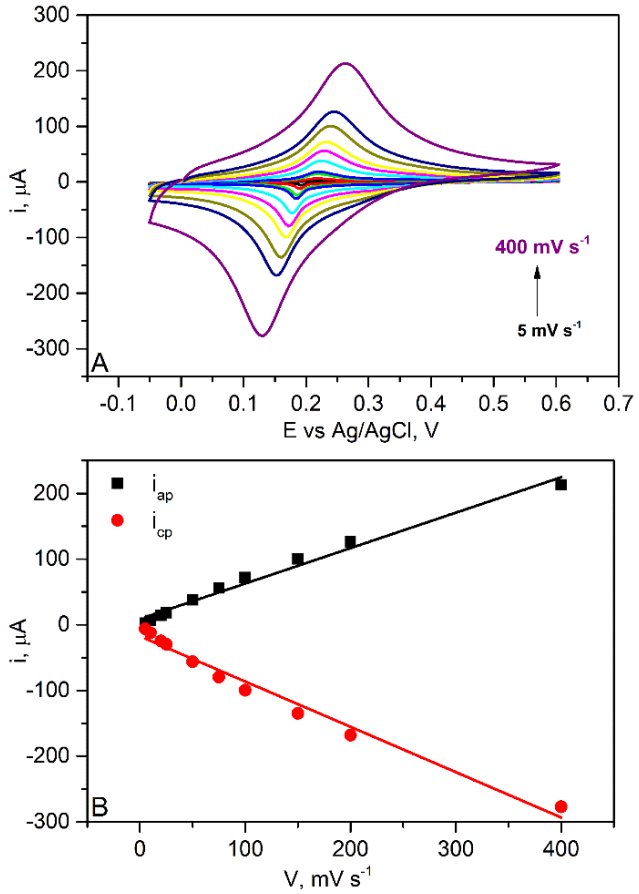

Figure 14: A) Cyclic voltammogram Pt electrode modified with Prussian blue at different scan rates, B) The dependence of peak currents on the scan rates. The experiments were performed in 0.1 mol L^{-1} HCl and 0.1 mol L^{-1} KCl.

Table 3: Electrochemical parameters calculated from voltammograms of 3D, Au, GCE and Pt electrodes modified with Prussian blue in 0.1 mol L^{-1} KCl/HCl

Electrode	V (mV s^{-1})	E_{pa}(V)	E_{pc}(V)	$E_{1/2}$(V)	ΔE_p(V)	I_{pa}(μA)	I_{pc}(μA)	I_{pa}/ I_{pc}
3D	2	0.211	0.156	0.183	0.06	0.61	-0.91	0.45
	5	0.221	0.135	0.178	0.09	0.96	-0.01	0.65
	7	0.226	0.120	0.173	0.11	0.01	-0.02	0.71
	9	0.231	0.115	0.173	0.17	0.01	-0.02	0.73
	11	0.231	0.110	0.171	0.12	0.01	-0.02	0.77
	13	0.231	0.095	0.163	0.14	0.01	-0.02	0.81
	15	0.236	0.090	0.163	0.15	0.	-164	0.81
	17	0.237	0.090	0.163	0.15	0.15	-221	0.84
Au	20	0.237	0.080	0.159	0.16	0.16	-271	0.85
	10	0.211	0.186	0.198	0.025	1.29	-2.56	0.51
	20	0.212	0.181	0.196	0.031	3.15	-5.15	0.62
	25	0.217	0.181	0.199	0.036	4.15	-6.73	0.62
	50	0.221	0.176	0.198	0.045	8.96	-13.4	0.68
	100	0.226	0.166	0.196	0.061	17.2	-24.7	0.71
	150	0.231	0.156	0.194	0.075	24.2	-33.7	0.72
	200	0.242	0.146	0.194	0.096	30.6	-41.4	0.74
	400	0.256	0.120	0.185	0.136	51.7	-70.6	0.73
GCE	5	0.211	0.196	0.203	0.015	0.565	-0.780	0.72
	10	0.217	0.191	0.204	0.026	1.26	-1.85	0.68
	25	0.226	0.186	0.206	0.041	3.52	-4.59	0.76
	75	0.246	0.171	0.208	0.075	10.42	-12.17	0.85
	100	0.251	0.161	0.206	0.09	13.31	-15.6	0.85
	150	0.267	0.151	0.209	0.116	18.58	-21.92	0.85
	200	0.276	0.141	0.209	0.135	23.27	-27.75	0.84
	400	0.307	0.100	0.203	0.207	39.01	-48.74	0.80
Pt	5	0.216	0.191	0.204	0.025	2.79	-6.08	0.46
	10	0.217	0.191	0.204	0.026	6.43	-12.2	0.52
	20	0.217	0.186	0.202	0.031	14.4	-24.6	0.59
	25	0.222	0.186	0.204	0.036	18.3	-29.7	0.61
	50	0.222	0.176	0.199	0.046	37.8	-56.1	0.67
	75	0.227	0.171	0.199	0.056	55.8	-79.4	0.70

100	0.231	0.166	0.199	0.065	71.8	-99.5	0.72
150	0.237	0.161	0.199	0.076	101	-135	0.74
200	0.242	0.151	0.197	0.091	126	-168	0.75
400	0.261	0.130	0.196	0.131	203	0.73	0.73

According to the obtained results, the redox processes described above are surface-confined at Au, Pt and GCE, due to the linear correlation between the peak current and the scan rate. Whereas at 3D, the redox processes were not surface-confined and depend on the diffusion of the ions into the structure of the materials. This is confirmed by the non-linear correlation between the peak current and the scan rate.

The stabilities of the PB in different substrates were investigated by cyclic voltammetry in 0.1 mol L^{-1} HCl/KCl (pH 1.0) and in 0.1 mol L^{-1} PBS containing 0.1 mol L^{-1} KCl (pH 7.4), according to Figure 15-16.

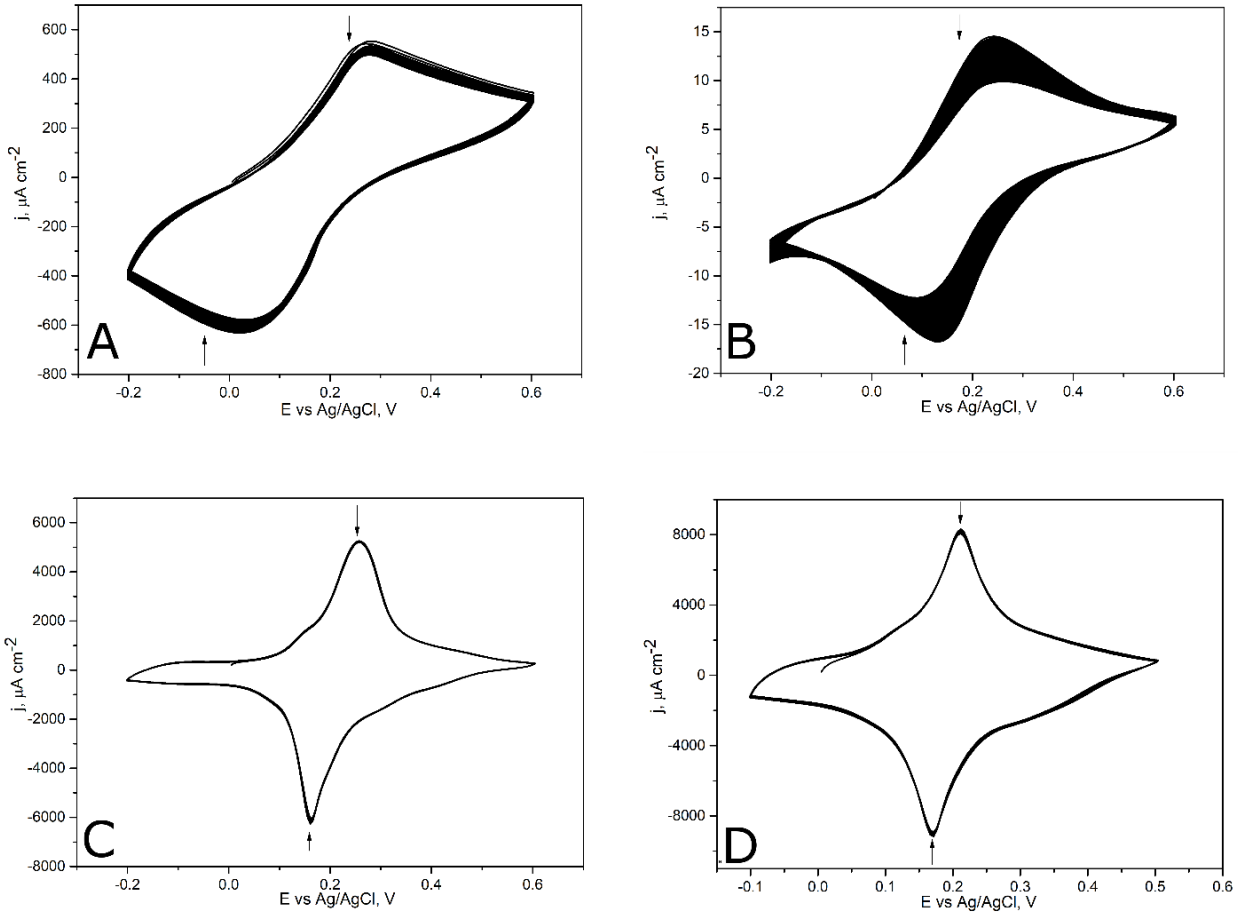

Figure 15: Cyclic voltammograms of Prussian blue modified (50 cycles): A) 3D, B) Au, C) GCE and D) Pt in 0.1 mol L^{-1} HCl/KCl (pH1).

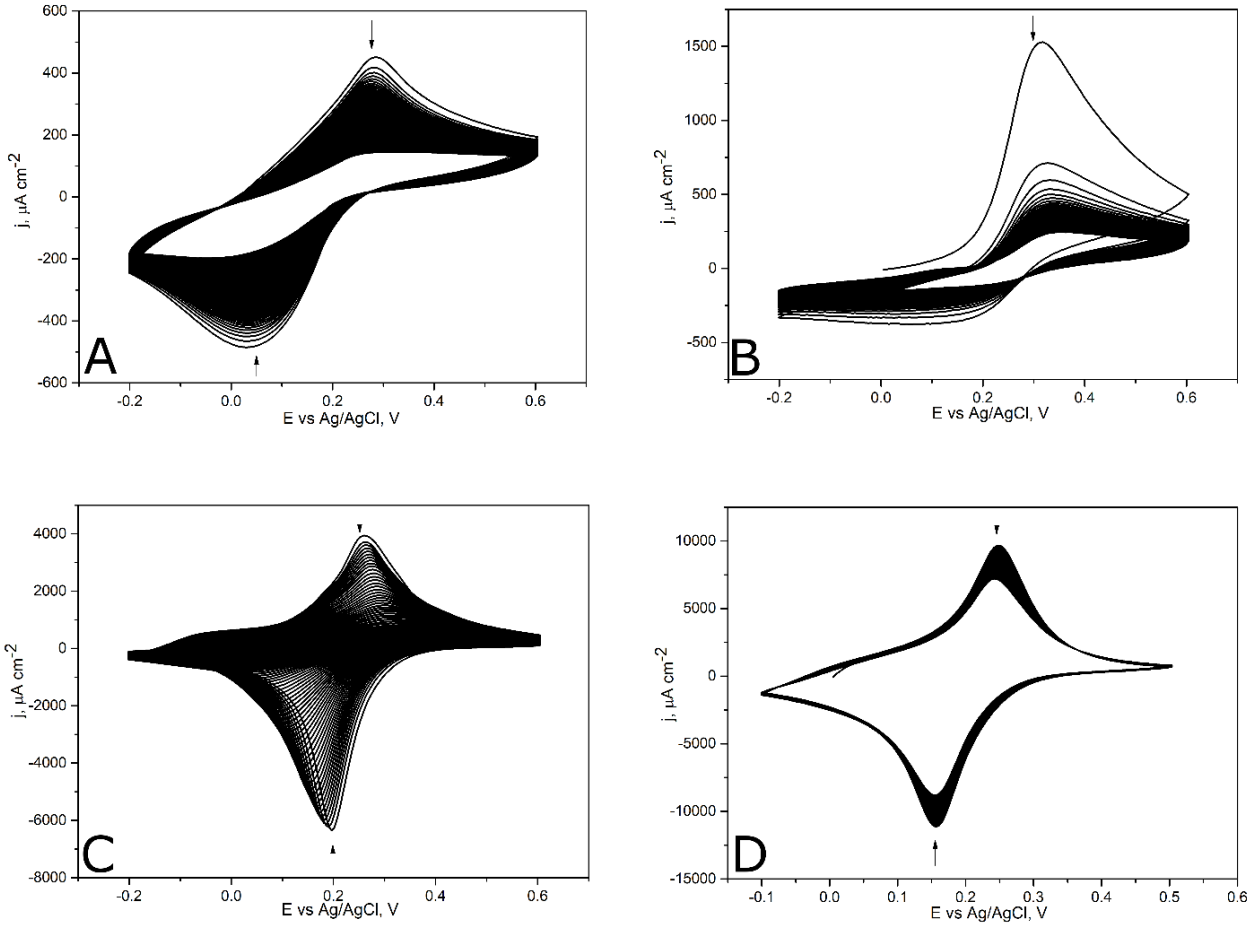

Figure 16: Cyclic voltammograms of Prussian blue modified (50 cycles): (A) 3D, (B) Au, (C) GCE and (D) Pt in 0.1 mol L^{-1} PBS/KCl (pH 7.4).

The percentages of Prussian blue on the surface of 3D, GCE, Au and Pt electrodes in function of the number of scans are presented in Figure 17. All of them have presented good stabilities at pH 1 and a decrease of the amount of film at pH 7.4. The lower stability of Prussian blue in neutral or alkaline solution is well known, due to the formation of iron hydroxide, breaking the Fe^{2+}−(CN)−Fe^{3+} bond [43]. According to our previous report, the stability of PB films can be increased by electrochemical activation in HCl/KCl, which converts the “insoluble” PB in its stable form, the “soluble” one [46]. The stabilization process occurs on the interface electrode/solution, by the insertion of K^+ into the interstitial sites of PB. Recently we have reported a comparison between the stabilities of PB_SPE (screen printed electrode), using a bulk and surface modification methods. The best stability was achieved using the last one, due to the interfacial activation [46]. Therefore, the stability of PB film depends on its thickness, thinner films tend to be more stable due to the higher conversion to “soluble” PB and

the better interaction with the substrate. The values of film thickness (l), estimated from the electroactive surface coverages (Γ) are presented in Table 4.

Comparing the behaviors of the modified electrodes in PBS, Prussian blue films have showed the best adherence on the Pt substrate. Additionally, the film was more stable at the surface of 3D than at the surfaces of GCE and Au. The increased stability of the 3D_PB can be attributed to the electrostatic interactions between iron cations of Prussian blue and the oxygen functionalities, created by the electrochemical pre-treatment. Moreover, the formation of a thin film, in the order of few nanometers, allows its conversion into the “soluble” form. The lowest stability of Prussian blue modified Au electrode can be associated with the largest film thickness, in the order of micrometers. It has been reported that the rate of chemical and electrochemical depositions of PB is higher on Au electrodes then on Pt or GCE substrates [24,53]. Therefore, using the same experimental conditions, such as electrodeposition time, ticker Prussian blue films are formed on Au. Thinner films are obtained at 3D due to its higher surface area.

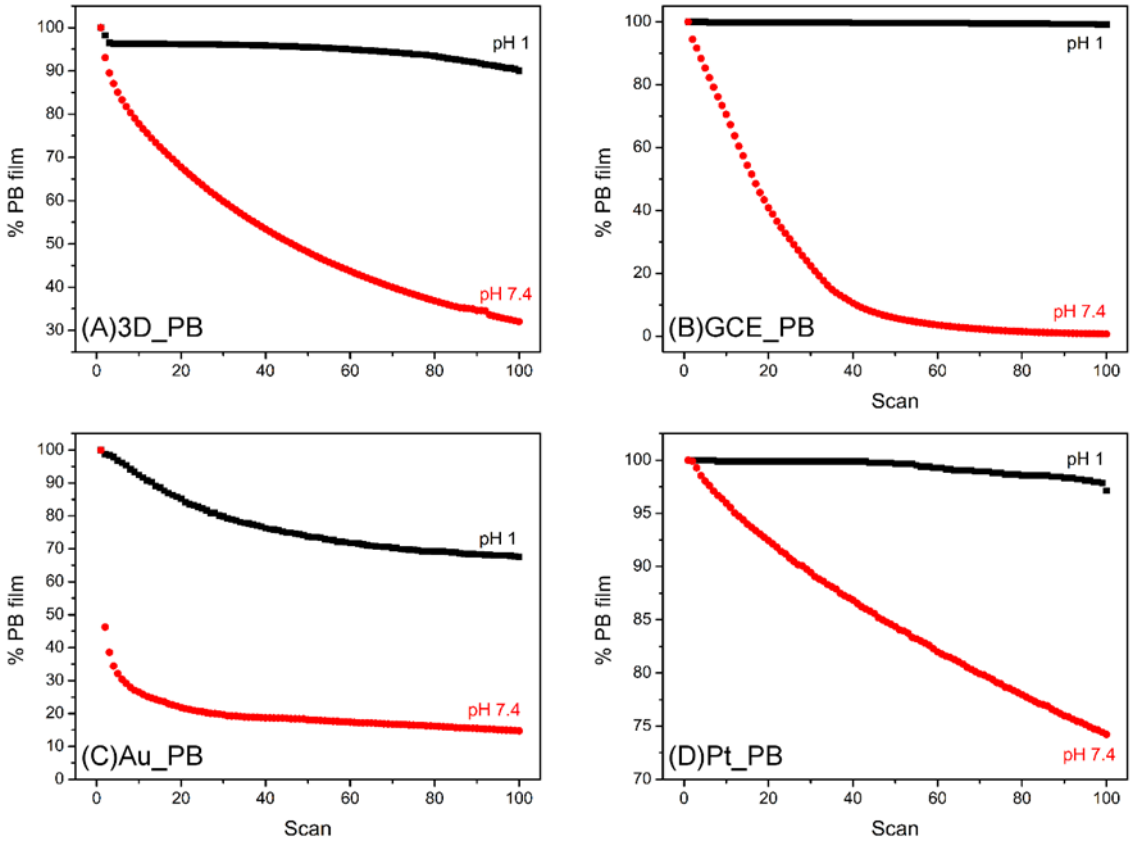

Figure 17: Comparison between the percentages of films in function of the number of scans at pH1.0 (0.1 mol L^{-1} HCl/KCl) and 7.4 (0.1 mol L^{-1} PBS/KCl) of the modified Prussian blue modified electrodes: A) 3D, B) GCE, C) Au and D) Pt..

The electrochemical behaviours of the bare and Prussian blue modified electrodes were analysed in the presence of $[Ru(NH_3)_6]^{3+}$ by cyclic voltammetry, Figure 18-19.

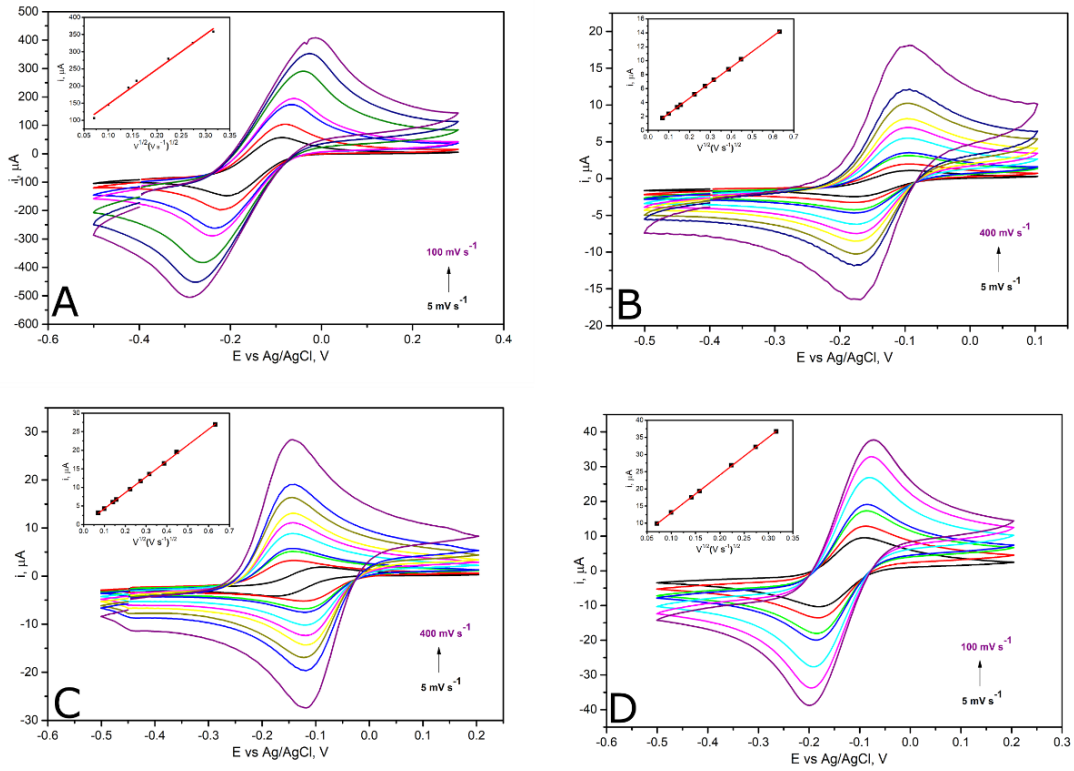

Figure 18: Cyclic voltammograms of bare A) 3D, B) Au, C) GCE and D) Pt electrode. An inset of each figure their respective linear relations between the anodic peak current and the square root of scan rate.

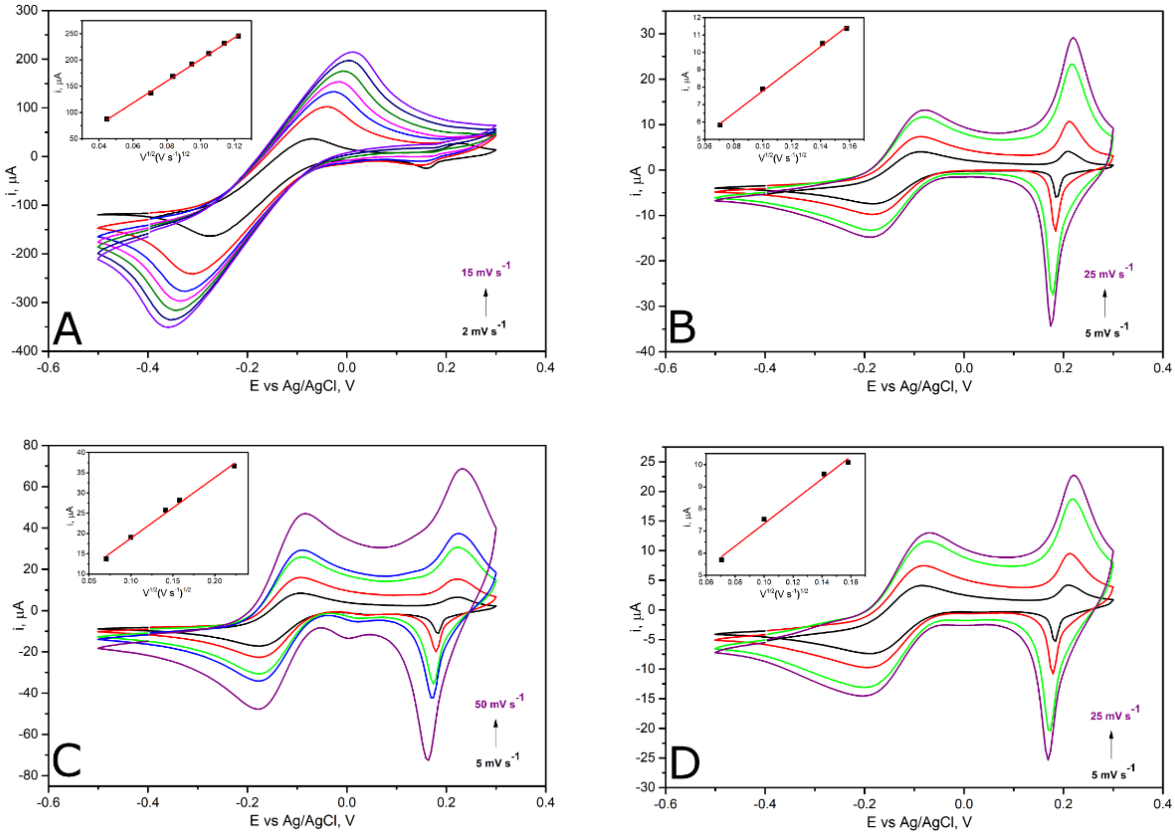

Figure 19: Cyclic voltammograms of Prussian blue modified A) 3D, B) Au, C) GCE and D) Pt electrode. An inset of each figure their respective linear relations between the anodic peak current and the square root of scan rate.

The electron transfer kinetics of the metallic substrates in $[Ru(NH_3)_6]^{2+/3+}$ has shown similar results. Since, $[Ru(NH_3)_6]^{2+/3+}$ is outer sphere redox probe, it is more sensitive to the electronic structure of the electrode material [54]. The modifier was not covalently attached to Pt or Au substrates, k^0_{obs} did not alter significantly after the modification. However, the electron transfer rates of GCE and 3D electrode depend on the ratio between the basal and edge planes exposed on the surface of the carbonaceous support [46,55,56].

The origin of the electron transfer in carbon-based materials is the edge planes, the number edge sites on the surface (θ_{edge}) can be estimated from Eq. 9, proposed by Hallam *et al*.

$$k^0_{obs} = k^0_{edge}(\theta_{edge}) \qquad (9)$$

were k^0_{obs} is the observed electron transfer rate; k^0_{edge} the electron transfer rate for edge plane (0.4 cm s^{-1}) [57]; θ_{edge} is the number of edge sites on the surface of the electrode.

The decrease of θ_{edge}, from 0.90 (GCE) to 0.30 (GCE_PB) and from 0.21 (3D_Bare) to 0.03 (3D_PB), can be directly associated the coverage of the edge planes with PB. These results corroborated with ones obtained in Raman spectra. The reduction of the number of structural defects/disorders, after the modification of 3D_Bare with PB, affects its electrochemical properties.

Table 4: Electroactive surface coverage, film thickness, electroactive area and heterogeneous electron transfer rate constant of the bare and modified electrodes.

	HCl/KCl		$[Ru(NH_3)_6]^{3+}$			
	Γ (mol m^{-2})	l (nm)	A_e (cm^2)		k^0_{obs} x 10^{-3} (cm^2 s^{-1})	
	PB		Bare	PB	Bare	PB
3D	4.55 x 10^{-5}	7.03	0.222	0.468	0.83	0.12
GCE	5.96 x 10^{-5}	92.1	0.0102	0.0256	3.58	1.21
Au	1.46 x 10^{-1}	22500	0.0051	0.0153	1.34	1.09
Pt	7.12 x 10^{-4}	440	0.0045	0.0148	1.26	0.99

3.5 Detection of H_2O_2

The performances of the bare and modified 3D electrodes towards H_2O_2 were evaluated by cyclic voltammetry, Figure 20.

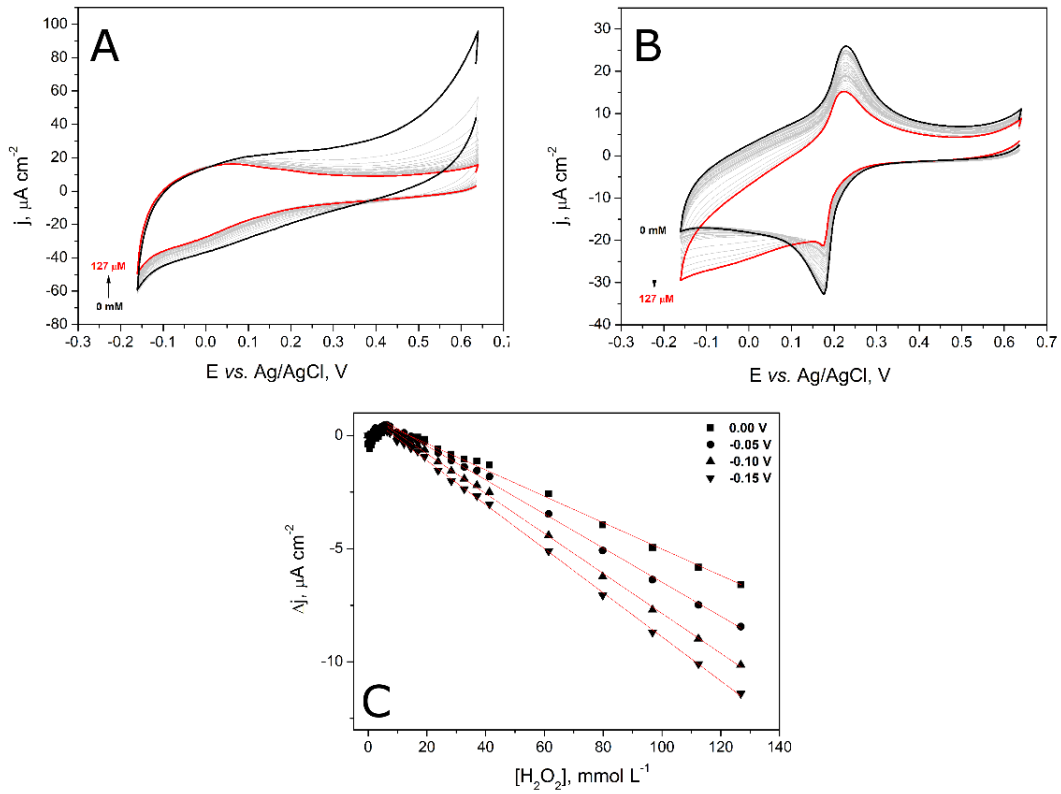

Figure 20: Cyclic voltammograms of A) bare 3D and B) modified 3D with PB in 0.1 mol L^{-1} PBS (pH 7.4) containing 0.1 mol L^{-1} KCl, with successive addition of 0.5 mmol L-1 H_2O_2 stock solution. Scan rate: 50 mV s^{-1}. C) Plots of the current response as a function of H_2O_2 concentration in different potentials of the voltammograms presented in B.

As it can be seen in Figure 20-A, there was no response for H_2O_2 reduction at the bare 3D electrode. However, at the 3D_PB (Figure 20-B), the profile the voltammogram changed after successive addition of H_2O_2, indicating the electrocatalytic activity of the modifier material. The electrocatalytic reduction of H_2O_2 produces hydroxide ions from the transfer of two electrons of Prussian white, as described by Eq. (10). The decrease of peak currents of Prussian blue after successive addition of H_2O_2 is due to the formation of iron hydroxide and destruction of the Fe^{2+}–(CN)–Fe^{3+} bond, Eq. (11) [43].

$$H_2O_2 + 2\,e^- \xrightarrow{k_{cat}} 2\,OH^- \quad (10)$$

$$Fe_4[Fe(CN)_6] + 12\,OH^- \rightarrow 4\,Fe(OH)_3 + 3\,[Fe(CN)_6]^{4-} \quad (11)$$

Based on the voltammogram of the 3D_PB, the reduction potential of -0.15 V vs. Ag/AgCl was selected for chronoamperometric measurements, which corresponds to the higher sensitivity (Figure 20-C). Chronoamperometry under successive additions of H_2O_2 at the 3D_PB was performed in triplicate as shown in Figure 21-A. The current density response in function of the concentration of H_2O_2 presented a linear range from 2.0 μmol L^{-1} to 112.0 μmol L^{-1}. The detection limit (LOD) of 0.44 μmol L^{-1} was calculated from the standard deviations of the intercepts (σ) and the slopes (s) of the calibration curve (Figure 21- B), LOD=3.3 σ/s. A comparison of several Prussian blue modified electrodes reported in the literature is presented in Table 5.

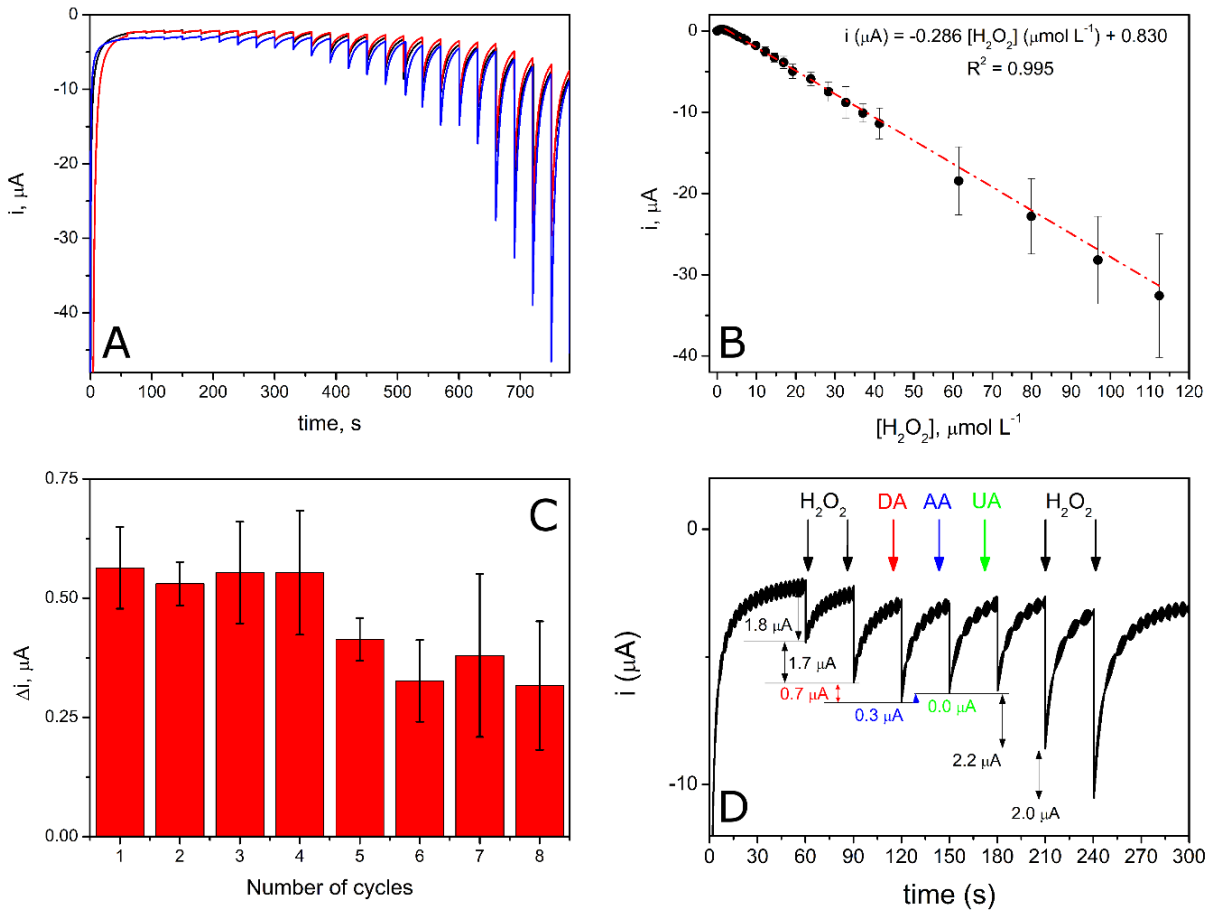

Figure 21: A) Chronoamperograms of three PB modified 3D electrodes recorded in 0.1 mol L^{-1} PBS (pH 7.4) containing 0.1 mol L^{-1} KCl, under successive addition of 10 (5x), 20 (5x), 50 (5x), 100 (5x) and 500 µL (4x) of 0.5 mmol L^{-1} H_2O_2 stock solution. Applied potential of -0.15 V vs. Ag/AgCl. B) Calibration curve of the current vs. H_2O_2 concentration. Standard deviations were calculated for the triplicate measurements shown in A. C) Current response of eight successive cycles of electrocatalytic reduction of 0.01 mmol L^{-1} H_2O_2. D) Amperometric response of 3D_PB in 0.1 mol L^{-1} PBS (pH = 7.4) containing 0.1 mol L^{-1} KCl at an applied potential of -0.15 V vs. Ag/AgCl with successive addition of 0.01 mmol L^{-1} H_2O_2 (2x), 0.01 mmol L^{-1} DA, 0.01 mmol L^{-1} AA, 0.01 mmol L^{-1} UA and of 0.01 mmol L^{-1} H_2O_2 (2x).

Table 5: Comparison of the performances of PB modified electrodes for detection of H_2O_2 in different substrates.

Electrode	Linear range, μM	Detection limit, μM	pH	Potential	Reference
GCE/PB[a]	0.1-100	0.10	PBS/KCl 6.0	-0.05 V*	[58]
FTO/PB[b]	90-350	36.0	HCl/KCl 2.0	-0.10 V*	[59]
SPE/PB[c]	0.4-100	0.40	PBS/KCl 7.4	0.0 V*	[60]
Fe-CNT/PB[b]	0.5-30	0.02	PBS/KCl 7.3	+0.15 V*	[61]
GCE/PB/rGO[b]	0.05-120	0.004	PBS/KCl 7.0	+0.20 V*	[50]
GCE/GO/PB[b]	5-1200	0.12	PBS/KCl 6.0	+0.10 V**	[62]
3D_PB[c]	2-112	0.44	PBS/KCl 7.4	-0.15 V*	This work

GCE: glassy carbon electrode; FTO: F-doped tin oxide; CPE: carbon paste electrode, Fe-CNT: Carbon nanotube paste electrode; GO: graphene oxide; rGO: reduced graphene oxide. *E *vs.* Ag/AgCl ** E *vs.* SCE [a] Flow-injection system; [b] Continuously stirred electrochemical cell; [c] Static electrochemical cell

The relative standard deviations (RSD) of the current response (Δi) for addition of 0.01 $mmoL^{-1}$ H_2O_2, using the same 3D_PB electrode, was 2.57% after 4 cycles. The decrease in the current response, RSD of 23.47% after 8 cycles, can be associated to the oxidation of Fe(II) during the electrocatalytic reaction (Eq. 10 and 11).

To investigate the possible interference of dopamine (DA), ascorbic acid (AA) and uric acid (UA) at the 3D_PB, chronoamperometry was performed after 2 successive additions of 0.01 mmol L^{-1} H_2O_2, followed by addition of 0.01 mmol L^{-1} DA, 0.01 mmol L^{-1} AA, 0.01 mmol L^{-1} UA and 2 additions of 0.01 mmol L^{-1} H_2O_2, Figure 21-D. Addition of UA resulted in a negligible current response, but DA and AA can affect the selectivity of the electrode, showing a current response of 38% and 15%, respectively.

4. Conclusion

Herein, we have reported electrochemical deposition of Prussian blue onto the surface of 3D printed graphene electrode. Prior to modification, the 3D printed electrode was submitted to simple electrochemical pre – treatment consisting. The treatment consists of application of constant potential of +1.8 V *vs* Ag/AgCl for 900 seconds in neutral media (PBS, pH 7.4), followed with application -1.8 V *vs* Ag/AgCl for 50 second. During electrochemical pre – treatment, the functionalization of the surface of the electrode occurs, *via* insertion of oxygenated groups.

Thus, allowing Prussian blue to be anchored onto the surface of 3D graphene electrode, which was confirmed with scanning electron microscopy. The gold, platinum and glassy carbon electrodes were also modified with Prussian blue. The 3D printed electrode has larger surface area when compared to others and has shown to be more stable in acidic and neutral pH, when compared to gold and glassy carbon electrodes. The modified 3D electrode was successfully applied in H_2O_2 electrochemical detection resulting in LOD of 0.44 µM with a linear range of 2-112 µM. The LOD is in the same order of magnitude compared with similar substrates reported in the literature.

Chapter 3

Use of screen-printed electrodes modified by Prussian blue and analogues in sensing of cysteine

3.1 Introduction

Over the recent decades, electroanalytical methods have received great attention from researchers, companies and clinical laboratories due to the simplicity of the procedures, speed of response, high reproducibility, satisfactory sensitivity and low costs [63,64].

This set of characteristics allows the application of electrochemical methods in
the determination of biomarkers, active pharmaceutical ingredient [55,64,65], food in gredients [66,67] and pollutants [68,69]. Because of this, the development of screen-printed electrodes (SPEs) have become a revolution in the world of electrochemical sensors [70].

SPEs are planar devices, based upon multiple layers of printable inks that can simplify the electroanalytical procedure. Such electrodes allow laboratory analyses to be performed on-site and are suitable for working with microvolumes and decentralized assays [37,71]. Furthermore, the ability to mass produce these screen-printed electrodes reproducibly allows their use as one-shot sensors, alleviating potential memory effects and contamination whilst eradicating the requirement of electrode pre-treatment and preparation (electrode polishing, potential cycling etc.), as is often the case for conventional solid electrodes (such as glassy carbon, boron-doped diamond etc.) [72–74].

SPEs have been widely used within clinical, environmental, biological, food safety and industrial analysis. The variety of commercials SPEs are available with an array of characteristics (i. e. different inks, substrates and heat curing temperatures) that directly influence on their electrochemical behaviour [68,71,75]. Typically, carbon materials used as the screen-printed mediators are widely applied within electrochemical research for the determination of biological analytes such as NADH, dopamine or cysteine.

In this sense, the analysis of the level of cysteine in the blood may reveal its deficiency and consequently be associated with the slow growth of children, some types of edemas, skin lesions, lethargy, liver damage, diabetes and mainly leukemia, Alzheimer and Parkinson's diseases [76,77].

The electroactive layer is the key to the transduction process in the electrochemical sensing of molecular targets. Due to this, the electroactive coordination polymers (ECP) prepared from cyanidoferrates (II) deserve attention owing to the well-defined chemical behaviour, stability of the film, facility in the preparation and wide range of application. In addition, the modulation of the electrochemical processes can be easily achieved by the strategic replacement of ligands in the complex and consequently, the properties are transferred to the ECP [59,78]. Prussian blue is a classic example of an ECP that can have its electrochemical behavior modulated according to the starting complex. For example, ECP or Prussian blue analogous (Prussian blue-Ammine) produced from $[Fe(CN)_5(NH3)]^{3+}$ have a shift of the electrochemical process Fe^{2+}/Fe^{3+} to $Fe^{3+/}Fe^{3+}$ to lower value when compared with the same process in the Prussian blue.

The shift observed is caused by lowering of energy levels of the HOMO orbital of the complex that is influenced by the sigma-donor character of NH_3 as ligand in the iron complex [79,80]. This modulation can be essential for the design of new types of sensors.

In this paper, we report the electrochemical behavior of a SPE modified with Prussian blue and Prussian blue - Ammine produced from $[Fe\ (CN)_5NH_3]^{3+}$ towards the sensing of cysteine. In addition, we compare the characteristics of SPEs with the electroactive materials incorporated within the ink and drop-cast upon the electrode.

3.2 Experimental section

3.2.1 Synthesis of $Na_3[Fe\ (CN)_5NH_3].3H_2O$

Sodium amminepentacyanidoferrate (II) was prepared by addition of 6.0 g of sodium nitroprusside in 40 mL of ammonium hydroxide in an Erlenmeyer. The mixture was stirred until the complete solubilization of $Na_2[Fe\ (CN)_5NO].2H_2O$. The Erlenmeyer was covered with aluminium foil and the top of the flask covered with cotton to allow the gas to exit. The solution was kept at room temperature, without stirring and

in the dark for 3h, turning into dark yellow. Then, 6.0 g of NaI was added for precipitation of a yellow solid. Finally, ethanol was slowly added to complete precipitation of the solid. The final product was filtered, washed with ethanol and dried under vacuum until constant weight. Yield: 87%. Elemental analysis calculated for $C_5H_9FeN_6Na_3O_3$ (325.98 g mol^{-1}): C 18.42%, H 2.78%, N 25.78%. Found: C 18.51%, H 2.69% and N 25.37%.

3.2.2 Synthesis of the ferric cyanidoferrates polymers

Ferric hexacyanidoferrate (II), known as Prussian blue (PB) and ferric pentacyanidoferrate (II) (PB-Ammine) were prepared by chemical method. It consists in adding FeCl3 in excess (4.10^{-2} mol L^{-1}) to a solution of potassium hexacyanidoferrate or sodium amminepentacyanidoferrate (1.10^{-2} mol $L^{-1)}$ under stirring. After 15 minutes, PB or PB-Ammine was precipitated in acetone and it was isolated by centrifugation.

3.2.3 Modification of the electrodes

. The bare screen-printed electrodes (SPEs) were fabricated as described previously [81,82]. The modified SPEs by ECP were prepared by two different methods. Firstly, 5.0 mL of suspensions of PB (2.0 mg mL^{-1}) and PB-Ammine (2.0 mg mL^{-1}) were drop-casted upon the surfaces of SPEs, which were subsequently left to dry overnight under vacuum at room temperature. The modified electrodes produced by the drop-casting method were labelled SPE/PB and SPE/PB-Ammine. Secondly, 10% (m/m) of PB and PB-Ammine were incorporated into the carbon-graphite ink (product code C2000802P2; Gwent Electronic Materials Ltd., U.K.) and used in the same printing process of the bare SPEs. The modified SPEs fabricated *via* the second method were labelled PB-SPE and PB-Ammine-SPE. After the modification, the SPEs were activated by applying 25 voltammetric cycles from -0.2 V to 0.6 V *vs* SCE in a solution of HCl 0.1 mol L^{-1} containing KCl 0.1 mol L^{-1} at a scan rate of 50 mV s^{-1}. Afterwards, the electrodes were dried in an oven at 60°C for 1 hour

3.2.4 Electrochemical measurements

Cyclic voltammetry (CV) measurements of SPE/PB and SPE/PB-Ammine were carried out using a Palmsens Emstat (Palmsens, Netherlands) potentiostat. CV of PB-SPE and PB-Ammine-SPE were performed on an AUTOLAB modular electrochemical system (ECO Chemie, Utrecht, Netherlands) equipped with a STAT 12 module and driven by NOVA 2.1 software. The bare or modified SPE were used as working electrode, a saturated calomel electrode (SCE) as reference electrode, and a platinum wire as auxiliary electrode. Acetate buffer (ABS, pH=6) containing KCl and HCl/KCl (pH=1) solutions were used for the stability measurements. Oxygen was removed by bubbling nitrogen for approximately 10 min through the solution before each electrochemical measurement.

The electroactive areas of the SPEs were determined via cyclic voltammetry in 1.0 mmol L^{-1} of $[Ru(NH_3)_6]^{3+}$ and 0.1 mol L^{-1} KCl at different scan rates, according to the Randles-Ševčík equation Eq. 5, (Chapter 2). The heterogeneous rate constants of the SPEs, k^0, were presented determined using the Nicholson method by the Eq.6, (Chapter 2).

3.2.5 Cysteine detection

Electrochemical detection of cysteine was carried out in the same conventional three-electrode electrochemical cell. Chronoamperometry measurements were performed at applied potential of 0.8 V *vs* SCE, upon successive additions of 0.1 mol L^{-1} L-cysteine hydrochloride stock solution, under N_2 atmosphere. Acetate buffer solution (0.1 mol L^{-1}, pH=6.0) containing 0.1 mol L^{-1} KCl was used as supporting electrolyte.

3.3 Results and discussion

3.3.1 Electrochemical properties of the screen-printed electrodes

The bare SPE does not exhibit any redox peaks, Figure 22. After 30 voltammetric cycles, the capacitive current increases, probably due to the alterations in the surface area and roughness of the electrodes. Functional groups, impurities, defects and edge plane-like sites on the graphite present in the ink also contribute to alterations within the double-layer capacitance [63].

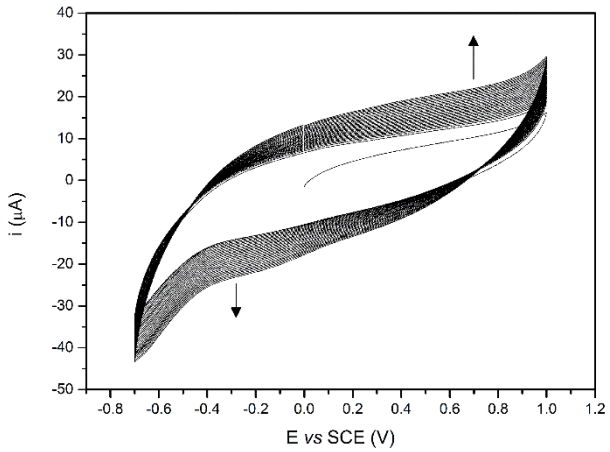

Figure 22: Cyclic voltammograms of the bare SPE at 100 mV s^{-1} in 0.1 M ABS (pH 6.0) and 0.1 mol L^{-1} KCl, 30 scans.

The electrochemical behaviour of the bare and modified SPEs was investigated by cyclic voltammetry and is depicted within Figure 23. All the modified SPEs exhibit two well-defined pairs of redox peaks ~ + 0.12 and + 0.80 V vs. SCE, which are ascribed to the electrochemical process between Prussian white (PW) to PB ($Fe^{2+/}Fe^{2+} \rightarrow Fe^{2+/}Fe^{3+}$), and PB to Berlin green (BG, $Fe^{2+/}Fe^{3+} \rightarrow Fe^{3+/}Fe^{3+}$), respectively. The composition of the modified SPEs is associated with the “insoluble” form of the ferric cyanidoferrate, synthesized from excess of Fe^{3+}.The “insoluble” form can be converted to the “soluble” after performing cyclic voltammetry experiments in KCl, because of the insertion of K^+ in the interstitial sites of the PB. The reduction and oxidation reactions of “soluble” (Eq. 1 – 2, Chapter 1) and “insoluble” forms of PB (Eq. 3-4, Chapter 1).

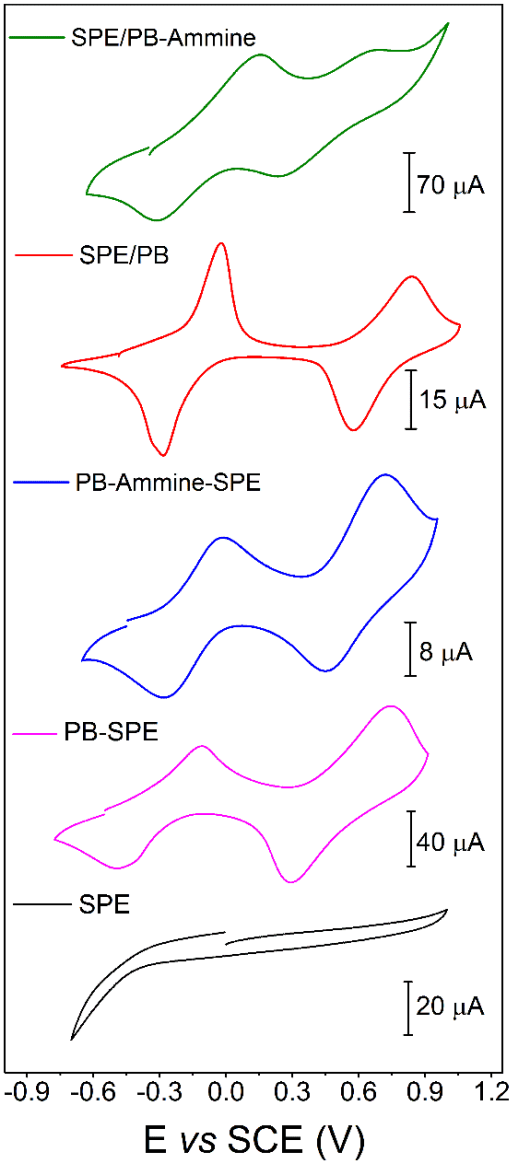

Figure 23: Comparison between the cyclic voltammograms of the bare SPE and modified: PB-SPE (*ink*), PB-Ammine-SPE (*ink*), SPE/PB (*drop*) and SPE/PB-Ammine (*drop*) in 0.1 mol L^{-1} ABS (pH = 6.0) and 0.1 mol L^{-1} KCl at 50 mV s^{-1}.

As described by the Eq. 1-4 (Chapter 1), the electrochemical process of Prussian blue is mediated by the transport of K^+ and Cl^- into and out of the film to maintain the electroneutrality. Thus, the redox processes of the modified electrodes are not surface-confined and depend on the diffusion of the ions into the structure of the materials. This is confirmed by the non-linear correlation between the peak current and the scan rates, as presented in Figure 24-26, with formal potential values ($E_{1/2}$) presented in Table 6-12.

The lowest values of $E_{1/2}$ of the SPE modified with PB-Ammine reflects the weaker π-acceptance character of the NH_3 ligand when compared with CN^-, consequently Fe^{3+} has a higher charge density facilitating the oxidation of this metal [80].

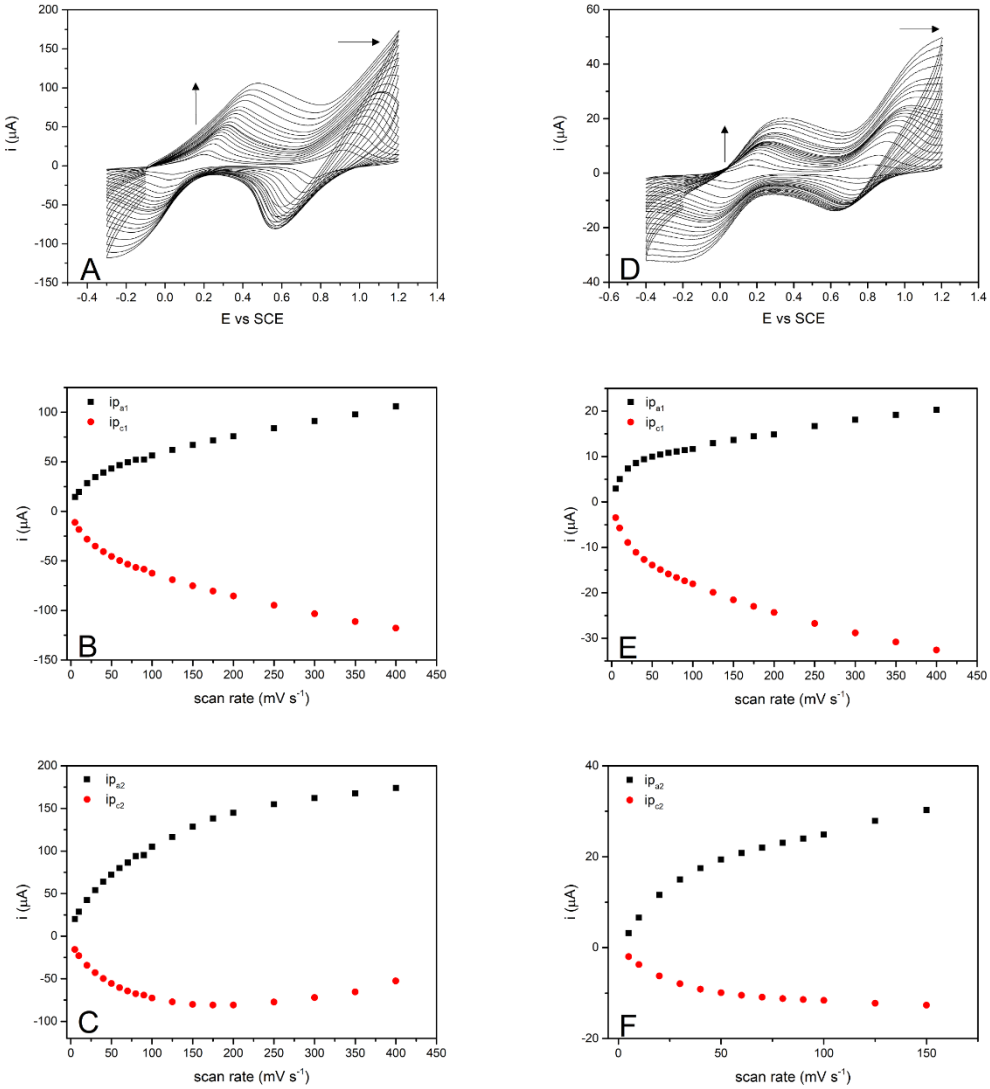

Figure 24: A) Cyclic voltammograms of PB-SPE (*ink*) at different scan rates in 0.1 mol L^{-1} ABS (pH 6.0) and 0.1 mol L^{-1} KCl. The dependence of peak currents on the scan rate (i_p *vs.* ν) for B) the process 1 and C) the process 2, D) cyclic voltammograms of PB-SPE-Ammine (*ink*) at different scan rates in 0.1 mol L^{-1} ABS (pH 6.0) and 0.1 mol L^{-1}KCl. The dependence of peak currents on the scan rate (ip *vs* ν), E) the process 1 and F) the process 2.

Table 6: Electrochemical parameters of the process 1 of PB-SPE (*ink*)

S. R.*	E_{pa1}	E_{pc1}	$E_{1/2}$ (V)	ΔE (mV)	i_{pa1}	i_{pc1}	$-i_{pa}/i_{pc}$
5	0.200	0.042	0.121	159	14.529	-11.231	1.294
10	0.220	0.022	0.121	198	19.571	-18.335	1.067
20	0.247	0.000	0.123	247	28.314	-28.009	1.011
30	0.266	-0.022	0.122	288	34.445	-35.098	0.981
40	0.278	-0.039	0.120	317	39.175	-40.747	0.961
50	0.288	-0.049	0.120	337	43.079	-45.554	0.946
60	0.300	-0.061	0.120	361	46.484	-49.744	0.934
70	0.308	-0.068	0.120	376	49.368	-53.497	0.923
80	0.318	-0.080	0.119	398	52.002	-56.610	0.919
90	0.320	-0.085	0.117	405	52.368	-58.411	0.897
100	0.332	-0.095	0.119	427	56.427	-62.378	0.905
125	0.347	-0.117	0.115	464	61.951	-69.000	0.898
150	0.361	-0.134	0.114	496	66.956	-75.165	0.891
175	0.374	-0.154	0.110	527	71.533	-80.536	0.888
200	0.388	-0.173	0.108	562	75.684	-85.480	0.885
250	0.410	-0.202	0.104	613	83.893	-94.788	0.885
300	0.430	-0.229	0.100	659	91.187	-100.330	0.883
350	0.449	-0.261	0.094	710	97.809	-111.121	0.880
400	0.474	-0.294	0.090	767	100.593	-117.889	0.899

*S. R. – scan rate in mV s^{-1}

Table 7: Electrochemical parameters of the process 2 of PB-SPE (*ink*)

S. R.*	E_{pa2}	E_{pc2}	$E_{1/2}$ (V)	ΔE (mV)	i_{pa2}	i_{pc2}	$-i_{pa}/i_{pc}$
5	0.913	0.767	0.840	146	14.529	-11.231	1.294
10	0.933	0.742	0.838	190	19.571	-18.335	1.067

20	0.965	0.711	0.838	254	28.314	-28.009	1.011
30	0.999	0.686	0.842	313	34.445	-35.098	0.981
40	1.026	0.667	0.846	359	39.175	-40.747	0.961
50	1.048	0.652	0.850	396	43.079	-45.554	0.946
60	1.069	0.637	0.853	432	46.484	-49.744	0.934
70	1.087	0.625	0.856	461	49.368	-53.497	0.923
80	1.109	0.615	0.862	493	52.002	-56.610	0.919
90	1.116	0.608	0.862	508	52.368	-58.411	0.897
100	1.140	0.598	0.869	542	56.427	-62.378	0.905
125	1.170	0.586	0.878	584	61.951	-69.000	0.898
150	1.199	0.574	0.886	625	66.956	-75.165	0.891
175	-	0.569	-	-	-	-80.536	-
200	-	0.564	-	-	-	-85.480	-
250	-	0.562	-	-	-	-94.788	-
300	-	0.567	-	-	-	-103.302	-
350	-	0.576	-	-	-	-111.206	-
400	-	0.596	-	-	-	-117.889	-

*S. R. – scan rate in mV s^{-1}

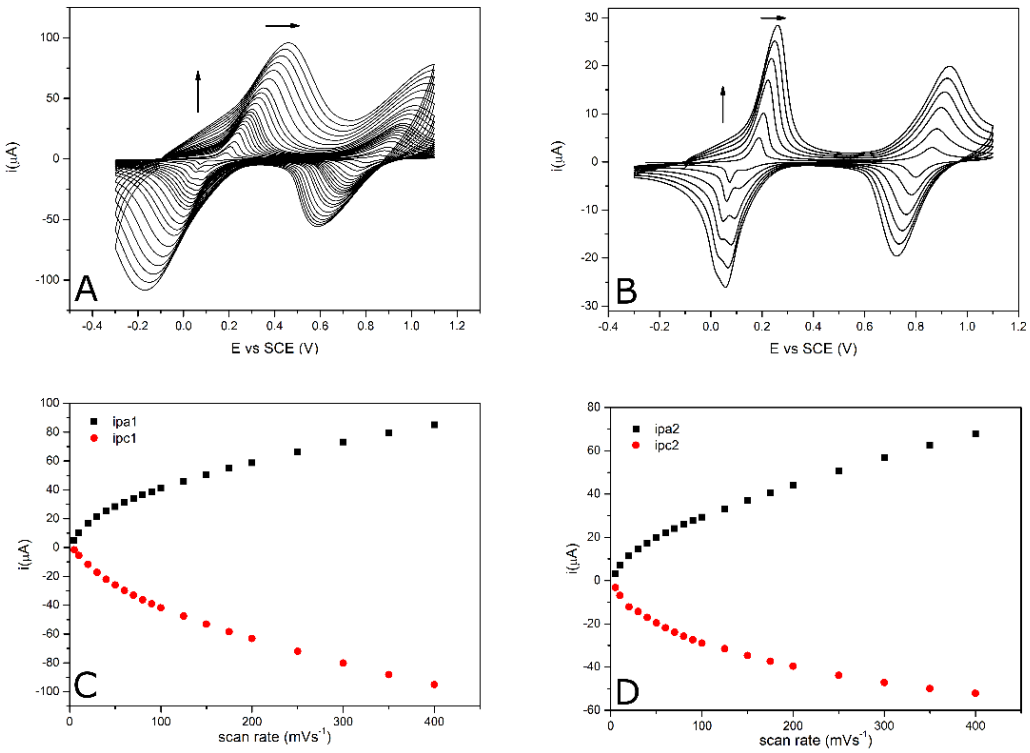

Figure 25: A) Cyclic voltammograms of SPE/PB (*drop*) at different scan rates in 0.1 mol L^{-1} ABS (pH 6.0) and 0.1 mol L^{-1} KCl. B) Cyclic voltammograms of SPE/PB (*drop*) at low scan rates in 0.1 mol L^{-1} ABS (pH 6.0) and 0.1 mol L^{-1} KCl. The dependence of peak currents on the scan rate (i_p *vs* ν) for C) the process 1 and D) the process 2.

Table 8: Electrochemical parameters of the process 1 of SPE/PB *(drop)*

S. R.*	E_{pa1}	E_{pc1}	$E_{1/2}$ (V)	ΔE (mV)	i_{pa1}	i_{pc1}	$-i_{pa}/i_{pc}$
5	0.185	0.140	0.163	45	5.035	-1.647	3.057
10	0.205	0.118	0.162	87	10.140	-5.535	1.832
20	0.223	0.092	0.158	131	16.730	-11.730	1.426
30	0.236	0.080	0.158	156	21.540	-17.280	1.247
40	0.248	0.069	0.159	179	25.220	-22.010	1.146
50	0.256	0.058	0.157	198	28.290	-26.090	1.084
60	0.269	0.048	0.159	221	31.270	-29.840	1.048
70	0.274	0.038	0.156	236	33.780	-33.160	1.019
80	0.282	0.033	0.158	249	36.390	-36.230	1.004
90	0.293	0.025	0.159	268	38.740	-39.110	0.991
100	0.300	0.017	0.159	283	41.040	-41.840	0.981
125	0.315	0.000	0.158	315	45.860	-47.560	0.964
150	0.330	-0.010	0.160	340	50.490	-53.210	0.949
175	0.340	-0.025	0.158	365	54.780	-58.390	0.938
200	0.350	-0.040	0.155	390	58.660	-63.090	0.930
250	0.375	-0.060	0.158	435	66.210	-72.030	0.919
300	0.395	-0.080	0.158	475	73.140	-80.140	0.913
350	0.410	-0.095	0.158	505	79.340	-88.100	0.901
400	0.425	-0.110	0.158	535	85.060	-95.080	0.895

*S. R. – scan rate in mV s^{-1}

Table 9: Electrochemical parameters of the process 2 of SPE/PB (*drop*)

S. R.*	E_{pa2}	E_{pc2}	$E_{1/2}$ (V)	ΔE	i_{pa2}	i_{pc2}	$-i_{pa}/i_{pc}$
5	0.860	0.800	0.830	60	2.984	-3.193	0.935

10	0.881	0.783	0.832	98	6.903	-6.842	1.009
20	0.897	0.763	0.830	134	11.320	-12.240	0.925
30	0.911	0.747	0.829	164	14.540	-14.320	1.015
40	0.919	0.735	0.827	184	17.360	-17.090	1.016
50	0.929	0.727	0.828	202	19.880	-19.590	1.015
60	0.935	0.717	0.826	218	22.060	-21.880	1.008
70	0.942	0.709	0.826	233	24.030	-23.880	1.006
80	0.953	0.704	0.829	249	25.890	-25.730	1.006
90	0.956	0.696	0.826	260	27.580	-27.380	1.007
100	0.961	0.690	0.826	271	29.340	-28.870	1.016
125	0.980	0.685	0.833	295	33.070	-31.520	1.049
150	0.990	0.670	0.830	320	36.950	-34.650	1.066
175	1.000	0.665	0.833	335	40.670	-37.330	1.089
200	1.010	0.655	0.833	355	44.050	-39.640	1.111
250	1.035	0.640	0.838	395	50.600	-43.790	1.156
300	1.050	0.620	0.835	430	56.700	-47.160	1.202
350	1.070	0.610	0.840	460	62.470	-50.000	1.249
400	1.079	0.600	0.840	479	67.890	-52.190	1.301

*S. R. – scan rate in mV s^{-1}

Table 10: Electrochemical parameters of the process 2 of the SPE/PB – Ammine (*drop*)

S. R.*	E_{pa2}	E_{pc2}	$E_{1/2}$ (V)	ΔE (mV)	i_{pa2}	i_{pc2}	$-i_{pa}/i_{pc}$
10	0.895	0.600	0.748	295	32.380	-16.060	2.016
20	0.955	0.570	0.763	385	52.240	-28.570	1.828

30	1.000	0.550	0.775	450	67.200	-38.690	1.737
40	1.025	0.520	0.773	505	80.750	-47.870	1.687
50	1.070	0.510	0.790	560	96.340	-53.190	1.811
60	1.090	0.495	0.793	595	109.300	-63.170	1.730
70	1.115	0.470	0.793	645	120.700	-70.280	1.717
80	1.140	0.455	0.798	685	133.100	-77.160	1.725
90	1.118	0.445	0.782	673	145.200	-83.470	1.740
100	1.200	0.425	0.813	775	159.500	-90.990	1.753
125	1.240	0.390	0.815	850	183.100	-103.100	1.776
150	1.300	0.360	0.830	940	204.400	-114.100	1.791
200	1.380	0.315	0.848	1065	246.600	-132.500	1.861

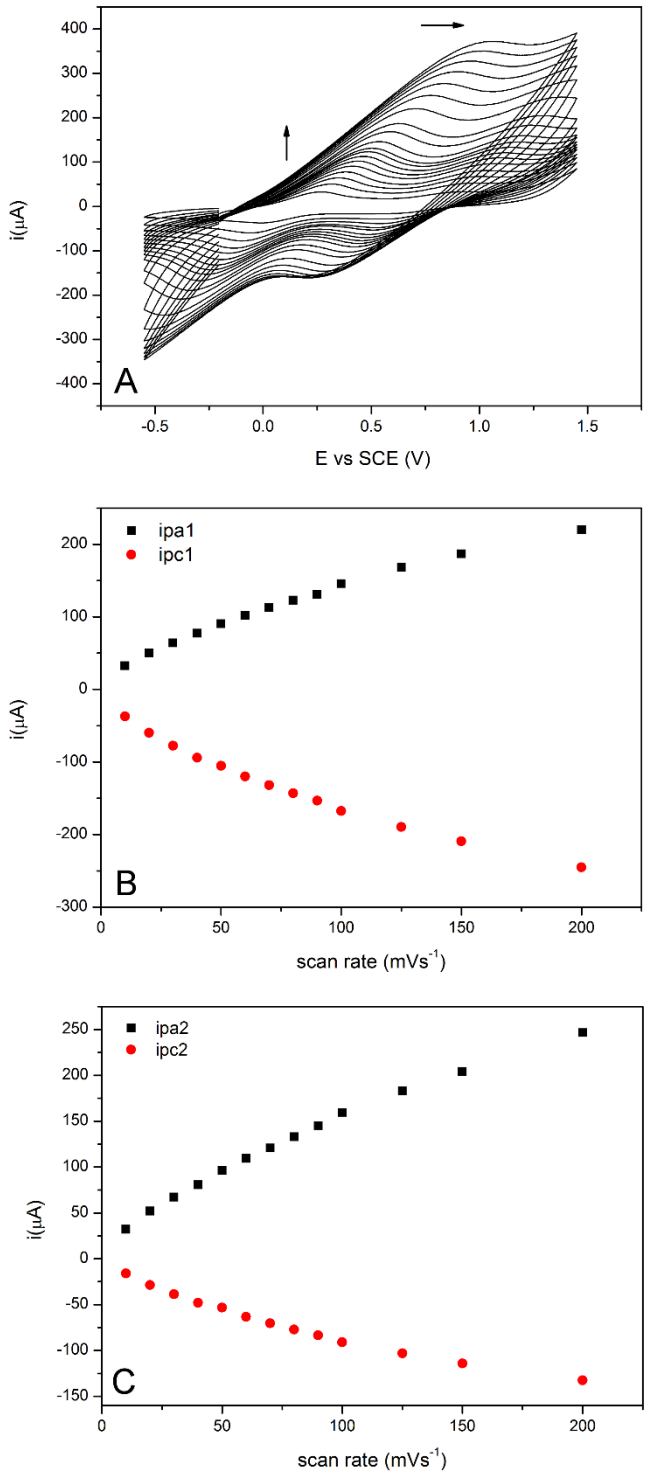

Figure 26: Cyclic voltammograms of SPE/PB-Ammine (*drop*) at different scan rates in 0.1 mol L^{-1} ABS (pH 6.0) and 0.1 mol L^{-1} KCl. The dependence of peak currents on the scan rate (i_p *vs* v) for B) the process 1 and C) the process 2.

Table 11: Electrochemical parameters of the process 1 of SPE/PB – Ammine (*drop*)

S. R.*	E_{pa1}	E_{pc1}	$E_{1/2}$ (V)	ΔE (mV)	i_{pa1}	i_{pc1}	$-i_{pa}/i_{pc}$
10	0.265	0.005	0.135	260	32.470	-37.040	0.877
20	0.315	-0.060	0.128	375	50.210	-59.760	0.840
30	0.345	-0.095	0.125	440	64.200	-77.630	0.827
40	0.385	-0.135	0.125	520	77.510	-94.080	0.824
50	0.415	-0.170	0.123	585	90.560	-105.300	0.860
60	0.440	-0.190	0.125	630	102.000	-119.900	0.851
70	0.460	-0.215	0.123	675	112.700	-132.000	0.854
80	0.490	-0.240	0.125	730	123.100	-143.000	0.861
90	0.505	-0.260	0.123	765	131.000	-153.200	0.855
100	0.540	-0.295	0.123	835	145.800	-167.600	0.870
125	0.580	-0.335	0.123	915	168.400	-189.400	0.889
150	0.625	-0.385	0.120	1010	186.800	-209.200	0.893
200	0.710	-0.455	0.128	1165	220.200	-245.300	0.898

Table 12: Electrochemical parameters of the process 2 of SPE/PB – Ammine (*drop*)

S. R.*	E_{pa2}	E_{pc2}	$E_{1/2}$ (V)	ΔE (mV)	i_{pa2}	i_{pc2}	$-i_{pa}/i_{pc}$

10	0.895	0.600	0.748	295	32.380	-16.060	2.016
20	0.955	0.570	0.763	385	52.240	-28.570	1.828
30	1.000	0.550	0.775	450	67.200	-38.690	1.737
40	1.025	0.520	0.773	505	80.750	-47.870	1.687
50	1.070	0.510	0.790	560	96.340	-53.190	1.811
60	1.090	0.495	0.793	595	109.300	-63.170	1.730
70	1.115	0.470	0.793	645	120.700	-70.280	1.717
80	1.140	0.455	0.798	685	133.100	-77.160	1.725
90	1.118	0.445	0.782	673	145.200	-83.470	1.740
100	1.200	0.425	0.813	775	159.500	-90.990	1.753
125	1.240	0.390	0.815	850	183.100	-103.100	1.776
150	1.300	0.360	0.830	940	204.400	-114.100	1.791
200	1.380	0.315	0.848	1065	246.600	-132.500	1.861

To study the electron transfer properties and determine the electroactive areas (A_e) of the bare and modified SPEs, cyclic voltammetry was carried out in the presence of the outer-sphere redox probe hexaammineruthenium (III) in 0.1 mol L^{-1} KCl, Figure 27, with corresponding values presented in the Table 13.

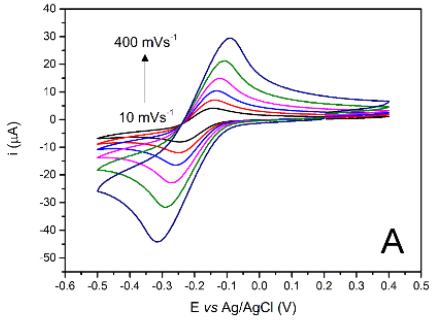
400 mVs-1
10 mVs-1
i (µA)
E vs Ag/AgCl (V)
A

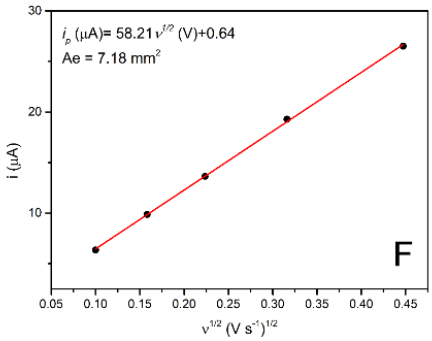
ip (µA)= 58.21 ν1/2 (V)+0.64
Ae = 7.18 mm2
i (µA)
ν1/2 (V s-1)1/2
F

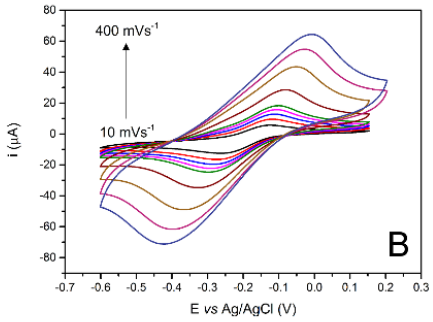
400 mVs-1
10 mVs-1
i (µA)
E vs Ag/AgCl (V)
B

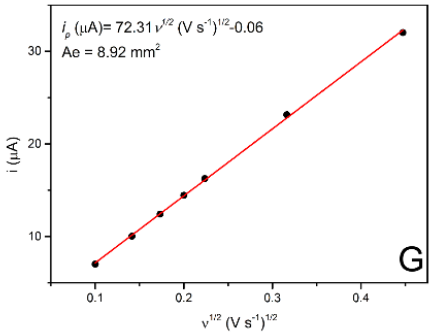
ip (µA)= 72.31 ν1/2 (V s-1)1/2-0.06
Ae = 8.92 mm2
i (µA)
ν1/2 (V s-1)1/2
G

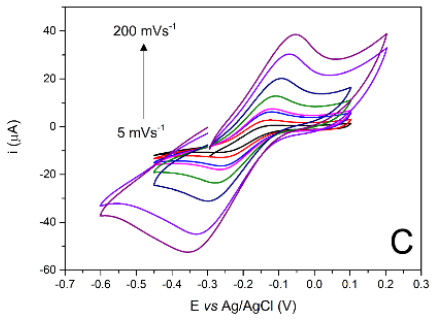
200 mVs-1
5 mVs-1
i (µA)
E vs Ag/AgCl (V)
C

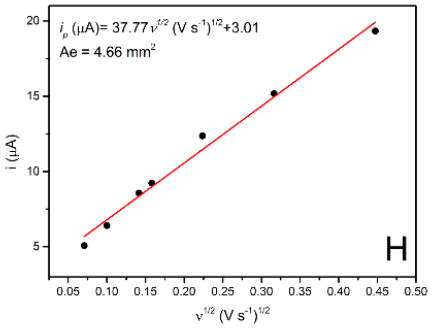
ip (µA)= 37.77 ν1/2 (V s-1)1/2+3.01
Ae = 4.66 mm2
i (µA)
ν1/2 (V s-1)1/2
H

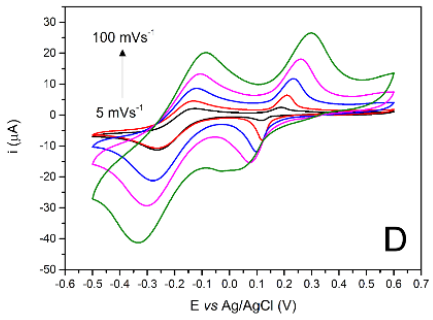
100 mVs-1
5 mVs-1
i (µA)
E vs Ag/AgCl (V)
D

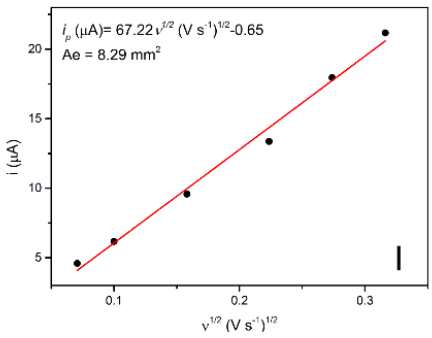
ip (µA)= 67.22 ν1/2 (V s-1)1/2-0.65
Ae = 8.29 mm2
i (µA)
ν1/2 (V s-1)1/2
I

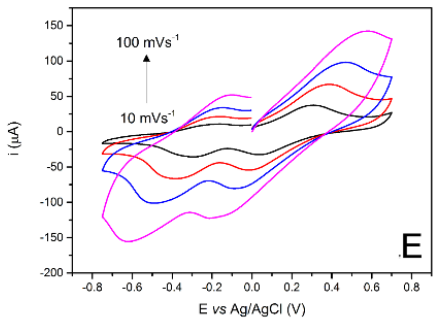
100 mVs-1
10 mVs-1
i (µA)
E vs Ag/AgCl (V)
E

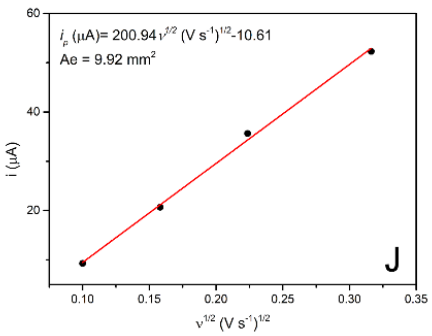
ip (µA)= 200.94 ν1/2 (V s-1)1/2-10.61
Ae = 9.92 mm2
i (µA)
ν1/2 (V s-1)1/2
J

Figure 27: Cyclic voltammograms of A) SPE, B) PB-SPE (*ink*), C) PB-Ammine-SPE (*ink*), D) SPE/PB (*drop*), E) SPE/PB-Ammine (*drop*) at different scan rates in 1.0 m mol L^{-1} $[Ru(NH_3)_6]^{3+}$ and 0.1 mol L^{-1} KCl. F-J) Their respectively linear relations between the anodic peak current and the square root of scan rate.

The electroactive areas of the PB or electroactive coordination polymers can be modulated by the utilisation of different monomers. Recently, an improvement of the A_e of the PB produced from pentacyanidoferrate complexes by drop-casting and potentiostatic methods was reported [59,67,78]. PB polymers with fcc structures are produced from hexacyanidoferrates complexes. The substitution of one CN^- to N-heterocycles ligands as isn (pyridine-4-carboxylate)[59] , mpz (N-methylpyrazinium) [78] and ppt (5-(4-pyridil)-1H-1,2,4-triazole-3-thiol)[67] promotes loss of symmetry and crystallinity of the polymers.

Thus, the higher electroactive area of SPE/PB-Ammine (*drop*) produced can be associated to its structural defects. On the contrary, the PB-Ammine-SPE (*ink)* presents the lower electroactive area, due to its decreased dispersibility in the carbonaceous matrix compared to the PB-SPE (*ink*). According to Table 13 the modified electrodes produced by the drop-casting method present larger electroactive areas, because of higher amount of the PB and PB-Ammine utilized, and it reflects in the heterogeneous rate constants (k^0).

The increase of the peak-to-peak separation in the voltammograms indicates the slower electron transfer after the modification of the electrodes,Table 13. The ferric cyanidoferrates polymers have partially blocked the interfacial charge transfer of the redox probe. The faster heterogenous electron transfer from the redox probe to the PB-Ammine-SPE is also attributed, to the low dispersibility of this material and better exposure of the conductive carbon material used in the ink.

Table 13: Peak potentials, electroactive areas and heterogeneous rate constants of the bare and modified SPEs

Electrode	E_{pa} (V)	E_{pc} (V)	ΔE (mV)	Ae (cm^2)	k^0 ($cm\ s^{-1}$)

SPE	-0.130	-0.260	130	0.0718	1.91×10^{-3}
PB-SPE*	-0.103	-0.299	196	0.0892	1.00×10^{-3}
PB-SPE-Ammine*	-0.109	-0.280	171	0.0466	1.28×10^{-3}
SPE/PB**	-0.105	-0.300	195	0.0829	1.02×10^{-3}
SPE/PB-Ammine**	-0.145	-0.490	345	0.0992	2.36×10^{-4}

* ink, ** drop

3.3.2 Stabilities of the modified screen-printed electrodes at different pH

To evaluate the stability of the films for application in electrochemical sensors, the stabilities of the modified electrodes were investigated by cyclic voltammetry in 0.1 mol L^{-1} ABS (pH 6.0) containing 0.1 mol L^{-1} KCl and in 0.1 mol L^{-1} HCl/KCl (pH 1.0), according to Figure 28-29.

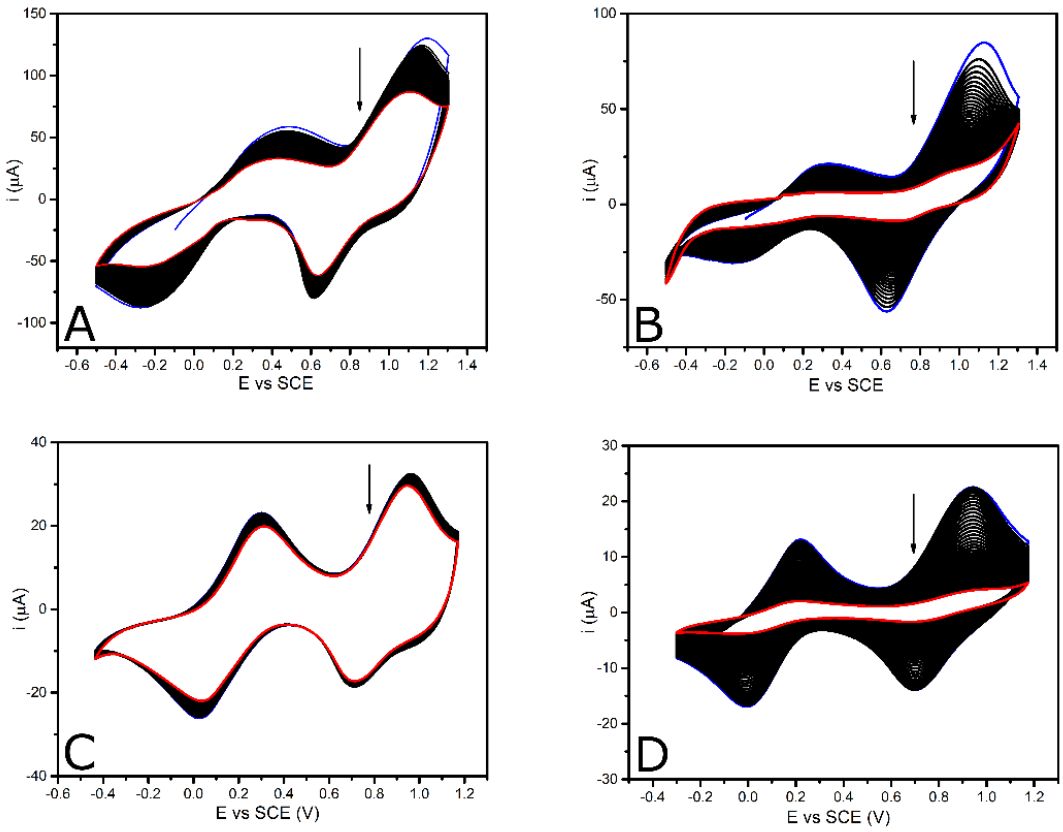

Figure 28: Comparison between cyclic voltammograms at pH1 and pH 6 of the modified electrodes by incorporation into ink (50 cycles) of PB-SPE A) at pH 1.0

(0.1 mol L^{-1} HCl/KCl), B) at pH 6.0 (0.1 mol L^{-1} ABS/KCl) and PB-SPE – Ammine C) at pH1.0 (0.1 mol L^{-1} HCl/KCl) and D) at pH 6.0 (0.1 mol L^{-1} ABS/KCl).

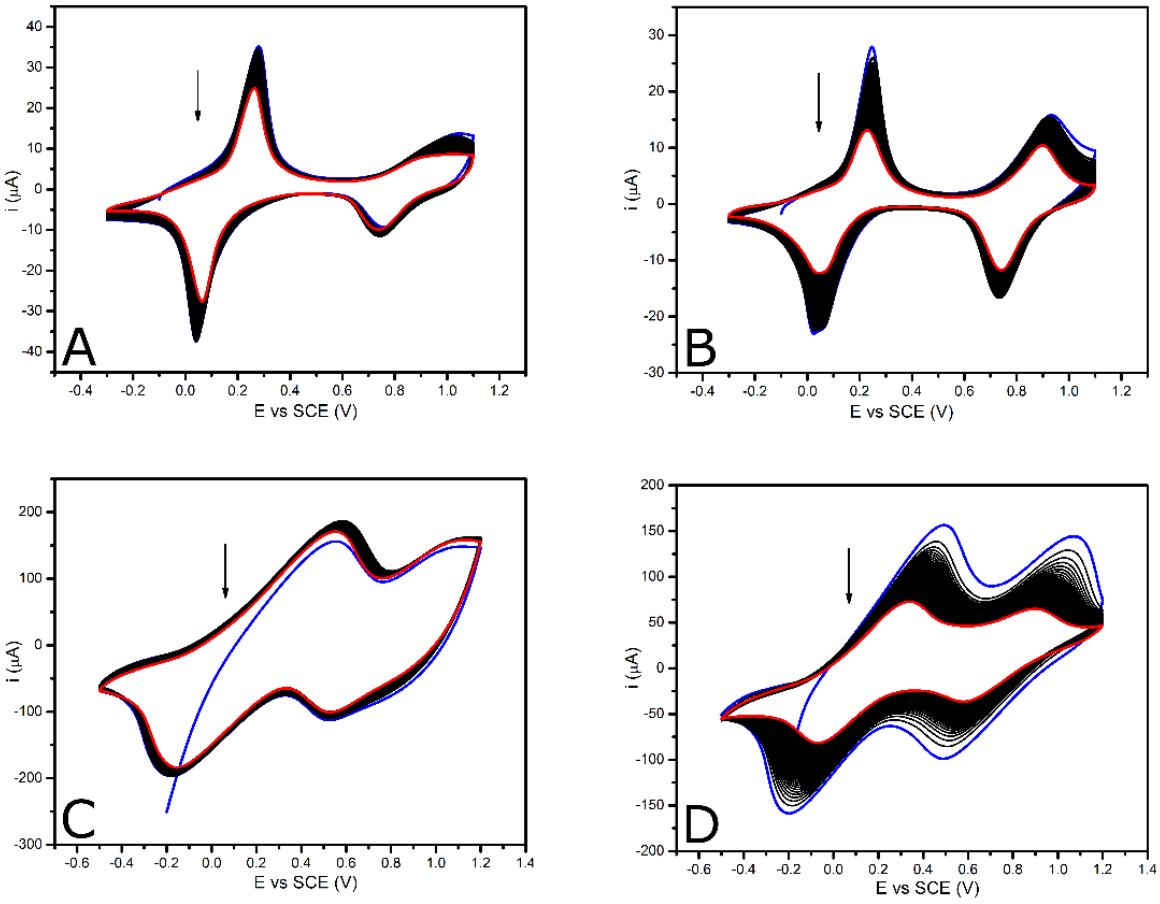

Figure 29: Comparison between cyclic voltammograms at pH1 and pH 6 of the modified electrodes by drop casting (50 cycles) of SPE/PB A) at pH 1.0 (0.1 mol L^{-1} HCl/KCl), B) at pH 6.0 (0.1 mol L^{-1} ABS/KCl) and SPE/PB– Ammine C) at pH1.0 (0.1 mol L^{-1} HCl/KCl) and D) at pH 6.0 (0.1 mol L^{-1} ABS/KCl).

The percentages of PB or PB-Ammine film in function of the scan is showed in Figure 30. The lower stability of the modified SPEs at pH 6.0 compared to pH 1.0 was as expected, due to the affinity of OH- ions for Fe (III) at pH close to 7.0, breaking the Fe^{2+}–(CN)–Fe^{3+} bond [43].

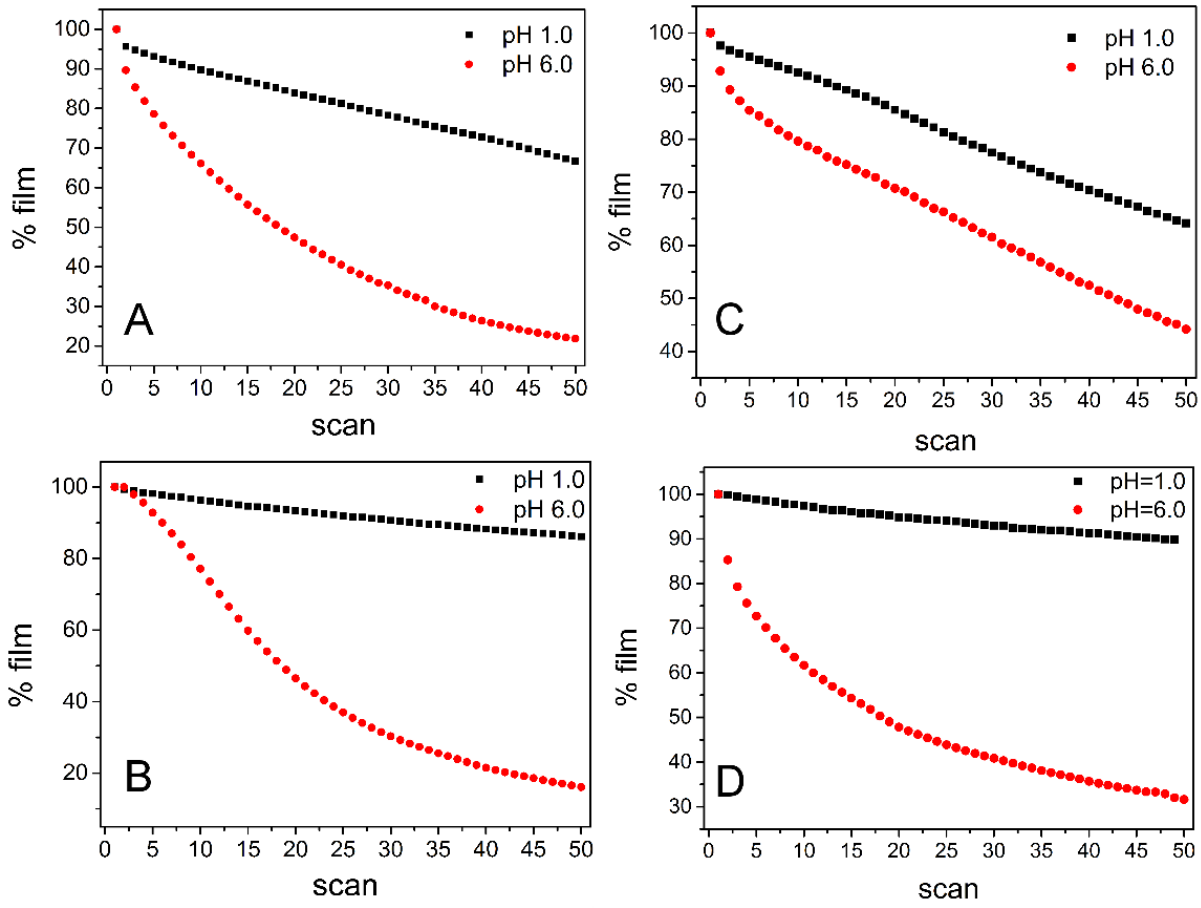

Figure 30: Comparison between the percentages of films in function of the number of scans at pH 1.0 and 6.0 of the modified electrodes: incorporation of ECP into the ink: A) PB-SPE, B) PB-Ammine-SPE, drop-casting: C) SPE/PB and D) SPE/PB-Ammine.

It is well known that the stability of the ferric hexacyanidoferrates polymers can be increased by electrochemical and thermal activations. These processes decrease the structural defects caused by the coordination of OH^- to Fe^{3+} during the formation of PB or PB-Ammine and remove water present within the crystals. However, the lability of the NH_3 ligand favours the exchange to H_2O or OH^- [43] at pH 6.0, affecting the structure of the SPEs modified with PB-Ammine and explains their lower stabilities.

The stability of the ferric cyanidoferrates polymers is also dependent on the method of deposition, due to the difference in availability of the ferric ions which can react with OH^-. In addition, the “soluble” form of PB is reported as the most stable one.

From electrochemical activation, the “insoluble” form of Prussian can be converted in to “soluble” form by insertion of K^+ in the interstitial site [83]. However, only the superficial layers of PB can be converted, due to direct contact with the KCl solution. It can explain the higher stability and more effective activation of the modified SPEs by drop-casting than the modification with the ink. In the other method, PB and PB-Ammine crystals are in the bulk of the electrode, entrapped in the carbonaceous matrix, presented as “insoluble” form.

3.3.3 Electrocatalytic properties

To determine the effect of pH upon the electro-oxidation of cysteine utilising the bare SPE, cyclic voltammetry experiments over a range of different pH’s in the presence of the analyte were performed, anodic peak current are shown in Figure 31.

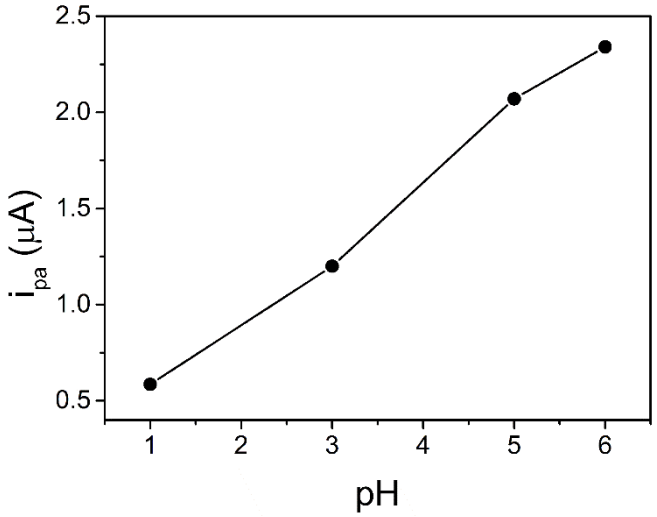

Figure 31: Plot of peak current of cysteine electro-oxidation at the bare SPE versus pH, in 1 mmol L^{-1} cysteine and 0.1 mol L^{-1} KCl/HCl (pH 1.0) or 0.1 mol L^{-1} ABS/KCl (pH 3.0, 5.0 and 6.0), at 5 mV s^{-1}.

The electrochemical oxidation of cysteine (RSH) to disulfide cystine (RSSR) on the bare SPE surface is proceed by Eq. 12-14:

$$RSH \rightarrow RS^- + H^+ \qquad (12)$$

$$RS^- \rightarrow RS\bullet + e^- \qquad (13)$$

$$2RS \bullet \rightarrow RSSR \qquad (14)$$

Depicted in the Figure 31, the peak current increases with the pH. At a higher pH deprotonation of RSH (pKa = 8.37) occurs producing RS^-, which is oxidized to RSSR *via* formation of sulphide radical [84], which corroborates with the improved electrochemical response at pH 6.0.

The lower peak potential at pH 6.0 can be associated to the deprotonation of cysteine. According to Fei and co authors, within an alkaline medium, the oxidation peak shifts to more cathodic potentials [85].

However, detection of cysteine in alkaline solution affects the stability of the ferric cyanidoferrates polymers. In our previous report, it was demonstrated that acetate buffer solution is the best choice for electrochemical experiments using modified electrodes with PB and analogues coordination polymers, causing small alterations in its structure [78]. In this sense, pH 6.0 is more appropriate for cysteine detection.

The electro-oxidation of cysteine at the bare and modified SPEs was compared by cyclic voltammetry at the chosen pH. Upon addition of cysteine, a pronounced increase of the current density was observed for the modified SPEs, due to the electrocatalytic activity of the PB and PB-Ammine toward the oxidation of the analyte, Figure 32.

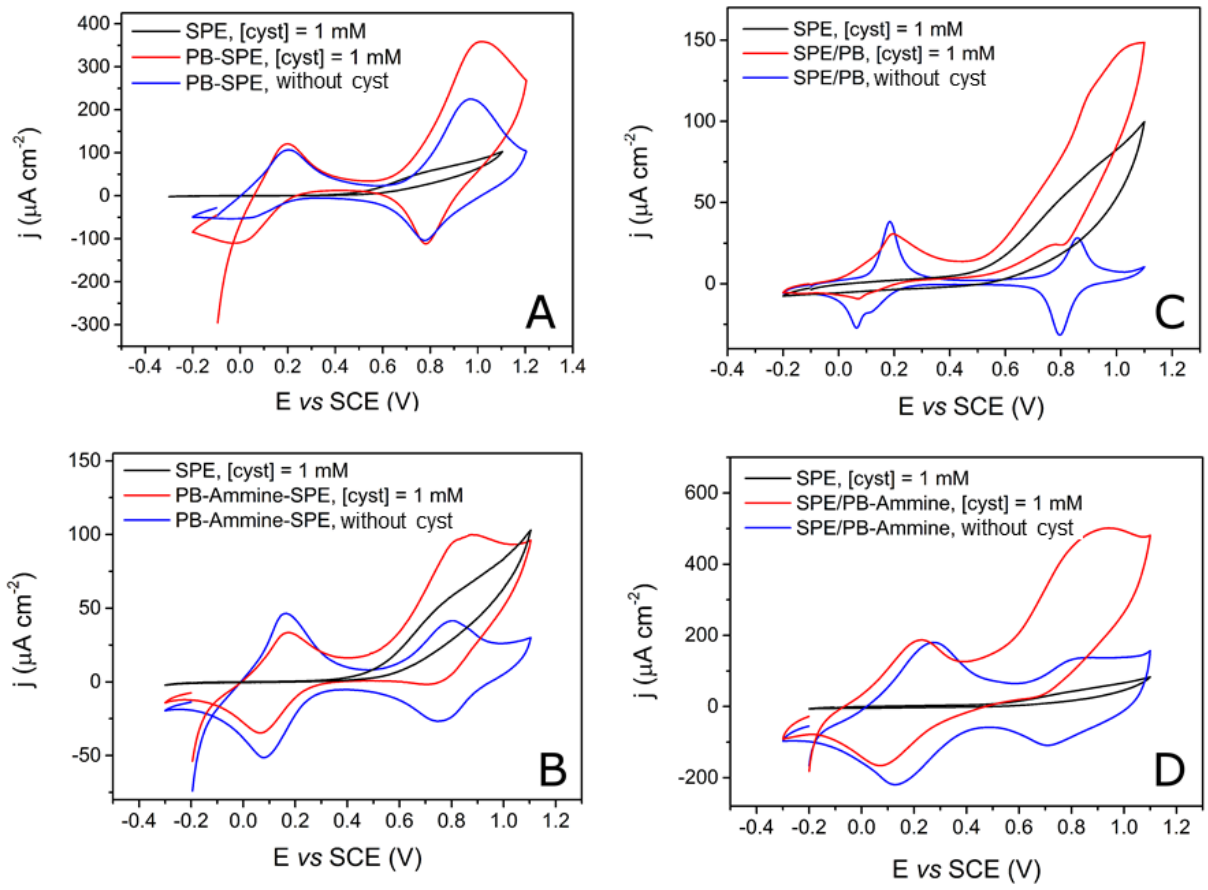

Figure 32: Comparison between the cyclic voltammograms of the bare SPE and modified: A) PB-SPE (*ink*), B) PB-Ammine-SPE (*ink*), C) SPE/PB (*drop*) and D) SPE/PB-Ammine (*drop*) in the absence and presence of 1 mmol L^{-1} of cysteine. All the measurements were performed in 0.1 mol L^{-1} ABS (pH = 6.0) and 0.1 mol L^{-1} KCl at 5 mV s^{-1}.

To further understand the electro-catalytic oxidation of cysteine on the surface of the modified SPEs, cyclic voltammetry experiments at different scan rates in presence of 1.0 mM of this analyte were performed, Figure 33.

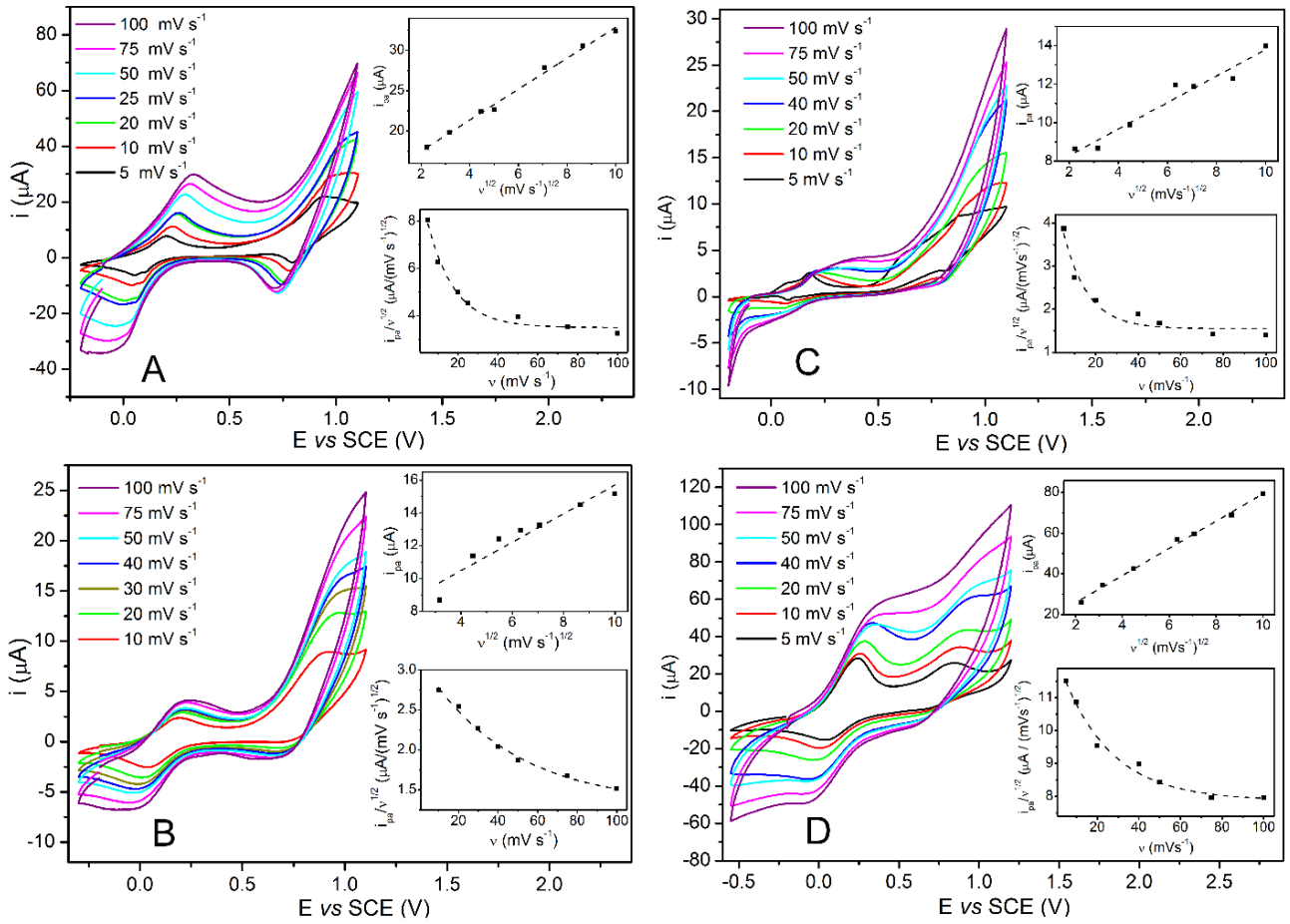

Figure 33: Cyclic voltammograms of A) PB-SPE (*ink*), B) PB-Ammine-SPE (*ink*), C) SPE/PB (*drop*) and D) SPE/PB-Ammine (*drop*) in presence of 1.0 mmol L^{-1} at various scan rates. All studies were performed in 0.1 mol L^{-1} ABS (pH = 6.0) and 0.1 mol L^{-1} KCl. Insert: plot of i_{pa} versus $\nu^{1/2}$ and plot of $i_{pa}/\nu^{1/2}$ versus ν. All currents were extracted from the potential of +0.87 V *vs* SCE.

The catalytic oxidation peak current (i_{pa}) increases linearly in function of the square root of the scan rate ($\nu^{1/2}$) in all modified electrodes, indicating that the electro-catalytic processes are diffusionally controlled toward cysteine (over the studied scan range) utilising all modified electrodes as can be expressed by Eq. 15-18 for the PB-SPE (ink), PB-Ammine-SPE (ink), SPE/PB (drop) and SPE/PB-Ammine (drop), respectively. In addition, characteristic shapes of a catalytic electrochemical process (EC_{cat}) were observed by plotting the scan rate normalized current ($i_{pa}/\nu^{1/2}$) versus scan rate, confirming the electro-catalytic efficiency of the ferric cyanidoferrate polymers.

$$(\mu A) = 13.7 + 1.9\, \nu^{\frac{1}{2}}(mV\ s^{-1})^{\frac{1}{2}} \qquad (15)$$

$$I(\mu A) = 8.5 + 0.7\, \nu^{\frac{1}{2}}(mV\ s^{-1})^{\frac{1}{2}} \qquad (16)$$

$$I(\mu A) = 4.5 + 2.5\, \nu^{\frac{1}{2}}(mV\ s^{-1})^{\frac{1}{2}} \qquad (17)$$

$$I(\mu A) = 3.2 + 10.5\, \nu^{\frac{1}{2}}(mV\ s^{-1})^{\frac{1}{2}} \qquad (18)$$

Cysteine (RSH) can be electro-oxidized to disulfide cysteine (RS-SR) by Fe^{3+} ions in the PB or PB-Ammine structures, which is reduced to Fe^{2+}. The generic reaction for cysteine oxidation on the surfaces of the modified SPEs has been proposed as follows [86,87]:

$$Fe^{3+} + 2RSH \xrightarrow{K_{obs}} Fe^{2+} + RS - SR + 2H^{+} \qquad (19)$$

To compare the kinetic of the chemical reactions between the Fe^{3+} ions in the PB or PB-Ammine modified SPEs and cysteine, chronoamperometric experiments in the presence of an array of concentrations of the analyte were performed and are presented in the Figure 34. The heterogeneous rate constants, k_{obs} of these reactions were determined according to Eq. 20:

$$\frac{i_{cat}}{i_0} = \gamma^{\frac{1}{2}}\, \pi^{\frac{1}{2}} = \pi^{\frac{1}{2}}(k_{obs}Ct)^{\frac{1}{2}} \qquad (20)$$

where i_{cat} is the catalytic current of the modified SPEs in the presence of cysteine, i_0 is the limiting current in the absence of cysteine and $\gamma = k_{obs}Ct$ (*C* is the bulk concentration of cysteine and *t* is the elapsed time [88].

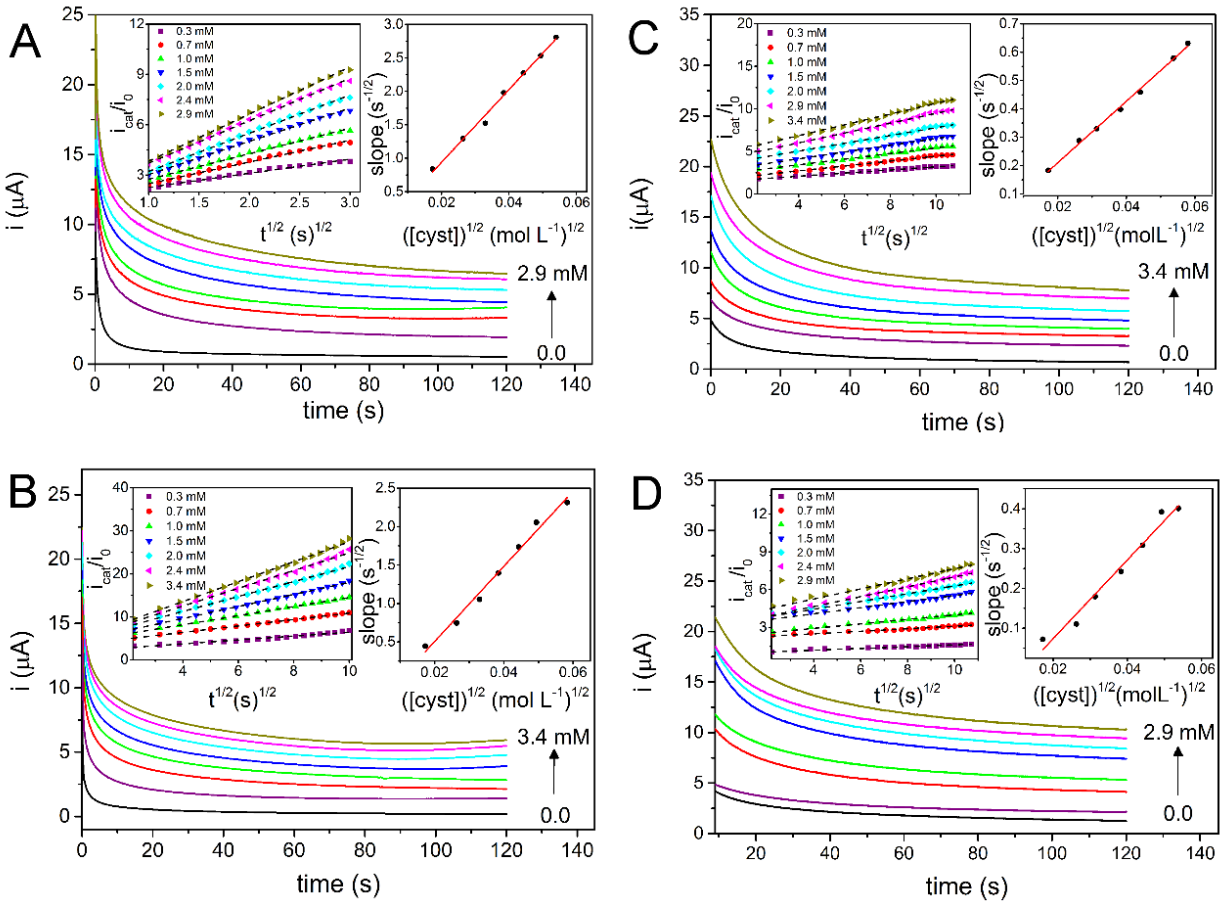

Figure 34: Chronoamperograms of A) PB-SPE (*ink*), B) PB-Ammine-SPE (*ink*), C) SPE/PB (*drop*) and D) SPE/PB-Ammine (*drop*) in 0.1 mol L^{-1} ABS at pH 6.0 different concentrations of cysteine. Insets: Curves of i_{cat}/i_0 versus $t^{1/2}$ for the same concentrations of cysteine, and plot of the slopes of these curves versus the square root of the concentrations of cysteine.

The heterogeneous rate constants were obtained from the linear plots of i_{cat}/i_0 *versus* $t^{1/2}$. Then, graphs of the slopes of these curves were plotted as a function of the square root of the concentrations of cysteine $[cyst]^{1/2}$. Finally, k_{obs} were calculated from the slopes of these graphs, resulting in values of 9.4×10^2, 3.6×10^2, 3.7×10^1 and 3.1×10^1 L mol^{-1} s^{-1} for PB-SPE (*ink*), PB-Ammine-SPE (*ink*), SPE/PB (*drop*) and SPE/PB-Ammine (*drop*), respectively. The modified SPEs *via* the incorporation of the materials in the ink presents a lower stability due to more exposure of the Fe^{3+}. However, the larger availability of these sites increases the heterogeneous rate constants for cysteine electro-oxidation at PB-SPE (*ink*) and SPE- PB-Ammine (*ink*). The faster kinetics of the chemical reactions between the Fe^{3+} ions in the PB-SPE (*ink*) and cysteine is attributed to the better distribution of this material and its higher

electroactive area. To compare the performances of the modified electrodes for sensing of cysteine, chronoamperometric experiments were next carried out.

2.3.4 Chronoamperometric detection of cysteine

Figure 35 presents the chronoamperometric responses of bare SPE, SPE/PB (*drop*), SPE/PB-Ammine (*drop*), PB-SPE (*ink*) and PB-SPE-Ammine (*ink*) after successive additions of cysteine in 0.1 mol L^{-1} ABS and 0.1 mol L^{-1} KCl at pH 6.0.

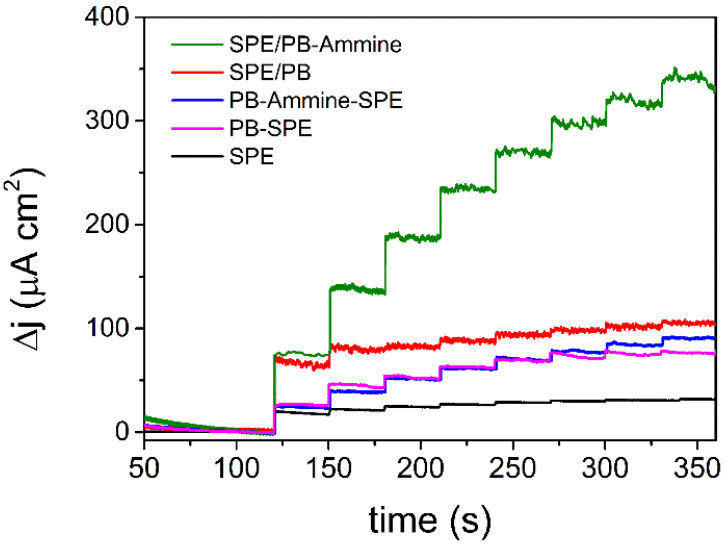

Figure 35: Chronoamperograms of the bare and modified SPEs: PB-SPE (*ink*), PB-Ammine-SPE (*ink*), SPE/PB (*drop*) and SPE/PB-Ammine (*drop*) in 0.1 mol L^{-1} ABS at pH 6.0 and 0.1 mol L^{-1} KCl after successive additions of 0.1 mol L^{-1} cysteine. Applied potential of + 0.8 V *vs* SCE.

As it can be seen from Figure 36 with an applied potential of 0.8 V *vs* SCE, the SPEs showed linear responses in the ranges presented in Table 14.

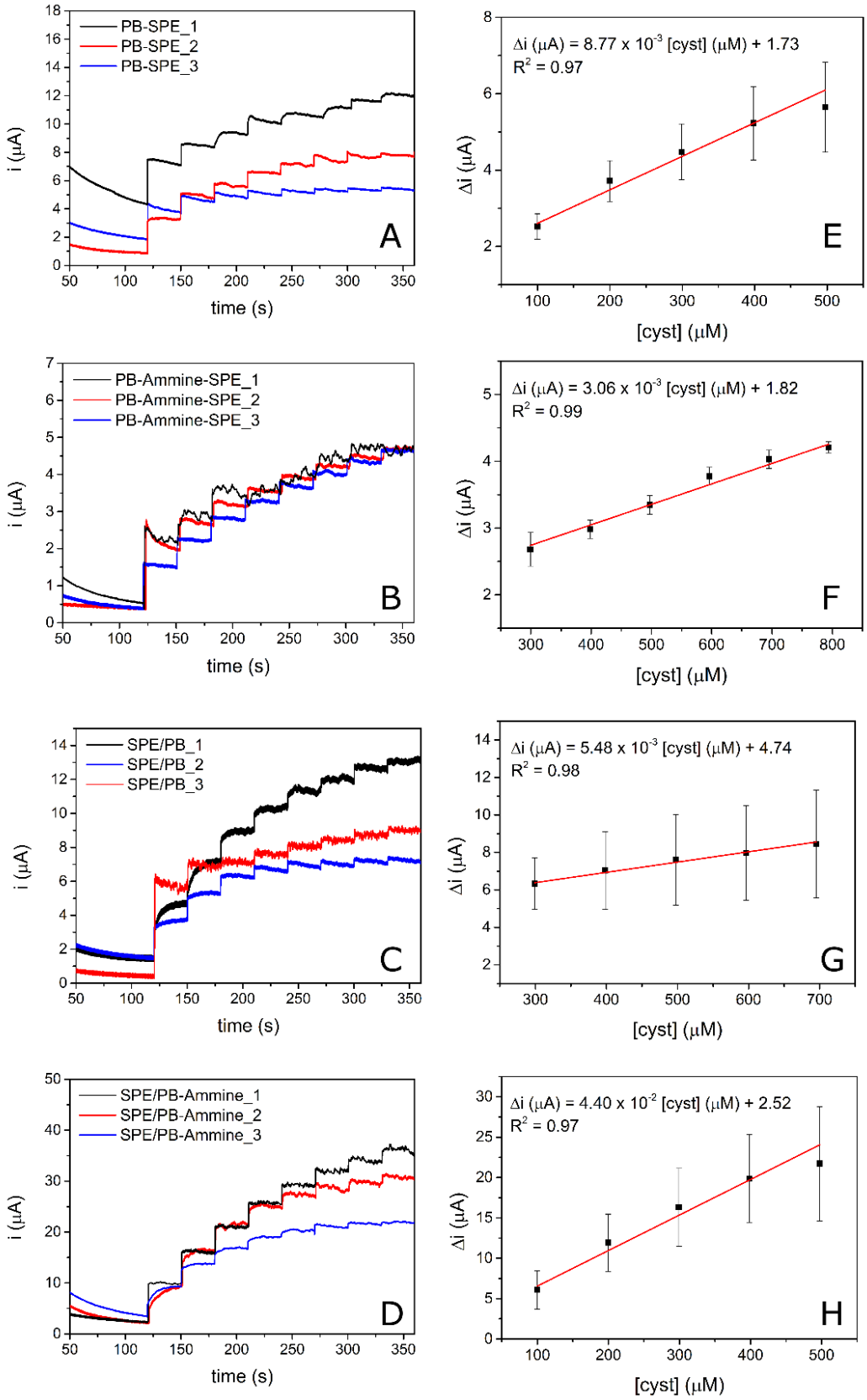

Figure 36: Chronoamperograms of A) PB-SPE (*ink*), B) PB-Ammine-SPE (*ink*), C) SPE/PB (*drop*) and D) SPE/PB-Ammine (*drop*) upon successive additions of

0.1 mol L^{-1} cysteine, in 0.1 mol L^{-1} ABS (pH 6.0) and 0.1 mol L^{-1} KCl. Applied potential: + 0.8 V *vs* SCE. E-H) The respective calibration curves.

Table 14 :Comparison of the amperometric responses of the modified electrodes

Electrode	Linear dependence	R^2	Linear range	LOD
PB-SPE*	$\Delta i(\mu A) = 7.03x10^{-3}$ [cyst](µM) + 2.80	0.99	200-600 µM	45.1 µM
PB-Ammine-SPE*	$\Delta i(\mu A) = 3.61x10^{-3}$ [cyst](µM) + 1.58	0.99	300-800 µM	102.4 µM
SPE/PB**	$\Delta i(\mu A) = 4.24x10^{-3}$ [cyst](µM) + 5.55	0.99	300-700 µM	70.2 µM
SPE/PB-Ammine**	$\Delta i(\mu A) = 4.89x10^{-2}$ [cyst](µM) + 3.58	0.99	100-500 µM	58.6 µM

* ink, **drop

The electro-oxidation of cysteine at the surface of the modified SPEs begins with the deprotonation of this molecule, which is diffused from the bulk solution to the electrode surface. On the PB or PB-Ammine modified SPE surface, the deprotonated cysteine is oxidized by the Fe^{3+} ions in the PB or PB-Ammine in an electro-catalytic process. The performances of the electrodes towards detection of cysteine are dependent on the electrode stability, the electron transfer from the modified electrode to the analyte, the availability of the ferric ions and the kinetics of the chemical reaction between the catalytic sites and the analyte.

Comparing the different ferric cyanidoferrates and the modification methods, the lowest detection limit was obtained at the PB-SPE, due to its high electroactive area and availability of Fe^{3+} catalytic sites. The incorporation of a non-conductive material as PB in the ink allows a less pronounced decrease of the heterogeneous electron transfer rate than the drop-casting method. In addition, as it is demonstrated in Figure 36 the error bars of the electrodes modified with ink are lower than that of the electrodes modified by drop casting. Thus, showing better reproducibility of the screen-printed electrodes modified within the ink. Although, PB-ammine electrochemical potentials are shifted to lower values than PB, the PB-ammine transfer rate is lower than that of the PB. This

feature explains the differences observed in the oxidation of cysteine (k_{obs}) and in the sensing of this analyte.

The possible interference for cysteine determination at the modified electr odes was further investigated. Figure 37 demonstrates the amperometric responses of the modified electrodes after addition of 0.1 mmol L^{-1} cysteine, followed by subsequent addition of 0.1 mmol L^{-1} L-tryptophan and 0.1 mmol L^{-1} L-tyrosine. The results showed that L-tyrosine did not cause significant interference. However, L-tryptophan is susceptible for electrochemical sensing at the surfaces of the modified SPEs affecting the selectivity of these electrodes.

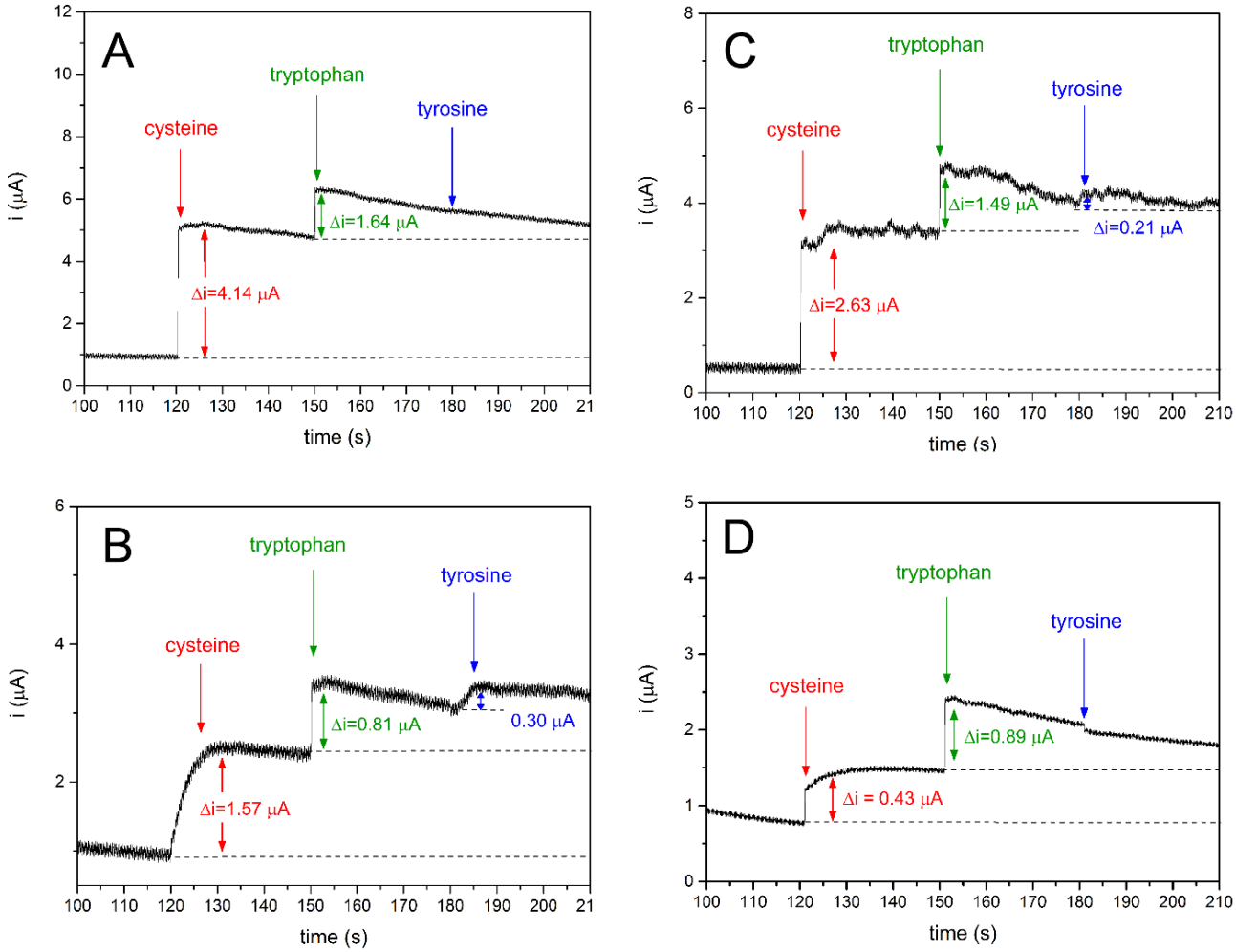

Figure 37: Chronoamperograms obtained for A) PB-SPE (*ink*), B) PB-Ammine-SPE (*ink*), C) SPE/PB (*drop*) and D) SPE/PB-Ammine (*drop*) upon successive addition of 0.1 mmol L^{-1} of cysteine, tryptophan and tyrosine into N_2-satured 0.1 mol L^{-1} ABS containing 0.1 mol L^{-1} KCl at pH 6.0.

2.4 Conclusion

Ferric cyanidoferrates polymers, PB and PB-Ammine, synthesized from different monomers $[Fe\ (CN)_6]^{4-}$ and $[Fe\ (CN)_5NH_3]^{3-}$ were used to modify screen-printed electrodes. The modification was performed via two methods, namely, the drop-casting and the incorporation of the materials in the ink used in the screen-printed process. The SPE modified by PB-Ammine (drop-casting) has the highest electroactive area. However, the highest heterogeneous rate constants are found with the SPE modified by PB-Ammine incorporated into the ink.

All of them have catalytic behaviour toward electro-oxidation of cysteine, but the highest value of kobs and lowest limit of detection was observed in the SPE modified by PB incorporated into the ink. These results suggest that the electrocatalytic properties
of SPE modified by PB and PB Ammine are dependent on the availability of Fe^{3+} cata lytic sites and the faster chemical reaction between the catalytic sites and the analyte.

Chapter 4

3D printed low-cost spectroelectrochemical cell for *in situ* Raman measurements

4.1 Introduction

The fusion of electrochemistry and spectroscopy results in a new technique known as spectroelectrochemistry [89,90]. This technique allows two measurements to be performed simultaneously, avoiding misinterpretation of electrochemical or spectroscopic results [91]. With the possibility to control applied potential, spectroscopic information can be obtained such as electronic absorption and vibrational states of molecules, related to in situ electrogenerated species. Numerous spectroscopic techniques coupled with electrochemical systems such as UV-Vis, Infrared and Raman spectroelectrochemistry have been reported [92–94].

Among them, Raman spectroelectrochemistry, a non-destructive tool with no sample preparation, emerges as a powerful technique for investigation of interfacial and surface phenomena. Therefore, this technique has been applied in the elucidation of formation, corrosion and passivation of films under different experimental conditions [95]. Spectroelectrochemistry allows real-time monitoring of electrode surfaces, kinetic studies of electrochemical reactions [96] and adsorption-desorption processes [97].

In addition, Raman spectroelectrochemistry has been extensively employed to identify reaction intermediates and to understand mechanism of electrocatalytic processes [98–101]. To perform spectroelectrochemical measurements, a proper spectroelectrochemical cell (SEC) should be used, and it is usually designed for specific equipment [101,102]. Timm et al. have reported a robust Raman SEC, resistant to chemical reactants and solvents [102]. However, the utilization of

expensive materials such as quartz plate and platinum ring increase the cost of the SEC. Additionally, the fabrication process requires specialized technicians to operate subtractive manufacturing machines.

To overcome this limitation, 3D printing technologies emerge as alternative tools for production of cheap, versatile and robust SEC. The multidisciplinary characteristic of this technology comes from its simplicity and the possibility to design almost without boundaries using free available designing tools, and to generate 3D objects [103]. Generally, 3D printing technologies enable the production of any kind of devices, either a part of the complex structures or the structure itself [104].

The main advantages of this technology are the ability of fast prototyping, waste management and generation of low-cost products [103,104]. Because of this, 3D printing technology has found applications in a variety of fields [105–107] including fabrication of electrochemical devices, such as electrodes [108], microbatteries [109], microfluidic chips [105] and electrochemical synthetic reactors [108]. In our recent work, we have enhanced performance of 3D printed graphene electrodes towards sensing of dopamine by applying simple electrochemical pre-treatment [40]. Cardoso et al. have reported a 3D printed electrochemical cell, for sensing of phenolic compounds, which allows the large-scale production and use for educational purposes [103].

Herein, we report the production of a cheap and robust Raman spectroelectrochemical cell printed in a 3D printer. The dome-shaped design of the SEC was produced using ABS filament. This design was chosen to fit Raman objective lenses in the center of the cell, above the surface of a working electrode. Additionally, a screw shaped working electrode was printed using conductive graphene-based PLA filament. The printing process was divided into two parts, a cup and a cover, to optimize printing and slicing processes. After printing the two parts were easily assembled. To prevent leakage of solution from SEC during the measurements, a printed screw nut was used which fitted perfectly with the working electrode. Beside a screw nut a rubber O-ring was used to fix working electrode in the center of the cell and to additionally prevent any leakage.

Details about design and construction of the 3D printed spectroelectrochemical cell are provided. To evaluate the applicability of the cell, the working electrode was modified with Prussian blue, and structural changes were studied during redox process. In addition, Raman-assisted electrochemical oxidation of 3D printed graphene working electrode were performed to investigate the structural defects during the functionalization process.

4.2 Experimental section

4.2.1 Design of the spectroelectrochemical cell and the working electrode

The spectroelectrochemical cell and the working electrode were designed using TinkerCAD™, a free online 3D CAD design tool. Standard tessellation language (STL) file was obtained and then the model was sliced on Simplify3D to generate the G-Code language, which instructs movements of 3D printer (RepRap Graber i3). The SEC was printed with ABS filament and the printing parameters were set to a resolution of 0.2 mm per layer, nozzle temperature of 230 ºC and bed temperature of 110 ºC. The working electrode was printed with commercial Black Magic PLA/graphene filament, and printing parameters were set to a resolution of 0.2 mm per layer, nozzle temperature of 190 ºC and bed temperature of 90 ºC.

The cell design was divided in two parts: the cup and the cover, to optimize slicing and printing process, as presented in Figure 38. The cup is a cylinder with diameter of 60 mm, height of 10 mm and wall thickness of 2 mm (item 1, Figure 38-A). The circular hole was introduced to (outer and inner diameter of 14 mm, and of 8.5 mm, respectively) allow coupling with a working electrode (item 3 in the Figure 38-A). The working electrode consists of a circular base of 9.9 mm in diameter, and height of 2.0 mm coupled with a screw thread.

The 3D printed screw nut (item 4, Figure 38-A) enables pressuring the head of working electrode against the O-ring to assemble the cell. This allows contact between working electrode and solution without leakage. The cover is a spherical cap (base diameter of 60.0 mm and height of 19.3 mm) with three holes (item 2, Figure 38-

A). A centered one with a diameter of 30.0 mm is the aperture for incident laser and the Raman lenses. The size and the dome-shape were defined to ease the entrance of Raman lenses in the cell interior to focus properly on the surface of the working electrode and to prevent solution contamination.

A support was printed to guarantee the cell immobility during the measurement. It consists of a 1 mm-thick rectangular shape base (85 mm x 75 mm, item 6 from Figure 38), which dimensions were defined according to Raman sample holder size. The support has a cylindrical cavity with a diameter 2 mm larger relative to the cup and depth of 1 mm inside a parallelepiped (height of 1 mm and square base of side 65 mm). In the center of the support a circular hole was introduced to enable screw and electrode connection. The other two holes (diameter of 10.0 mm each) were located with a maximum separation of 45.0 mm from each other with respect to their centers with an inclination of 22.5 degrees, for traditional reference and counter electrode, Figure 38-C The diameters were designed according to the size of the electrodes.

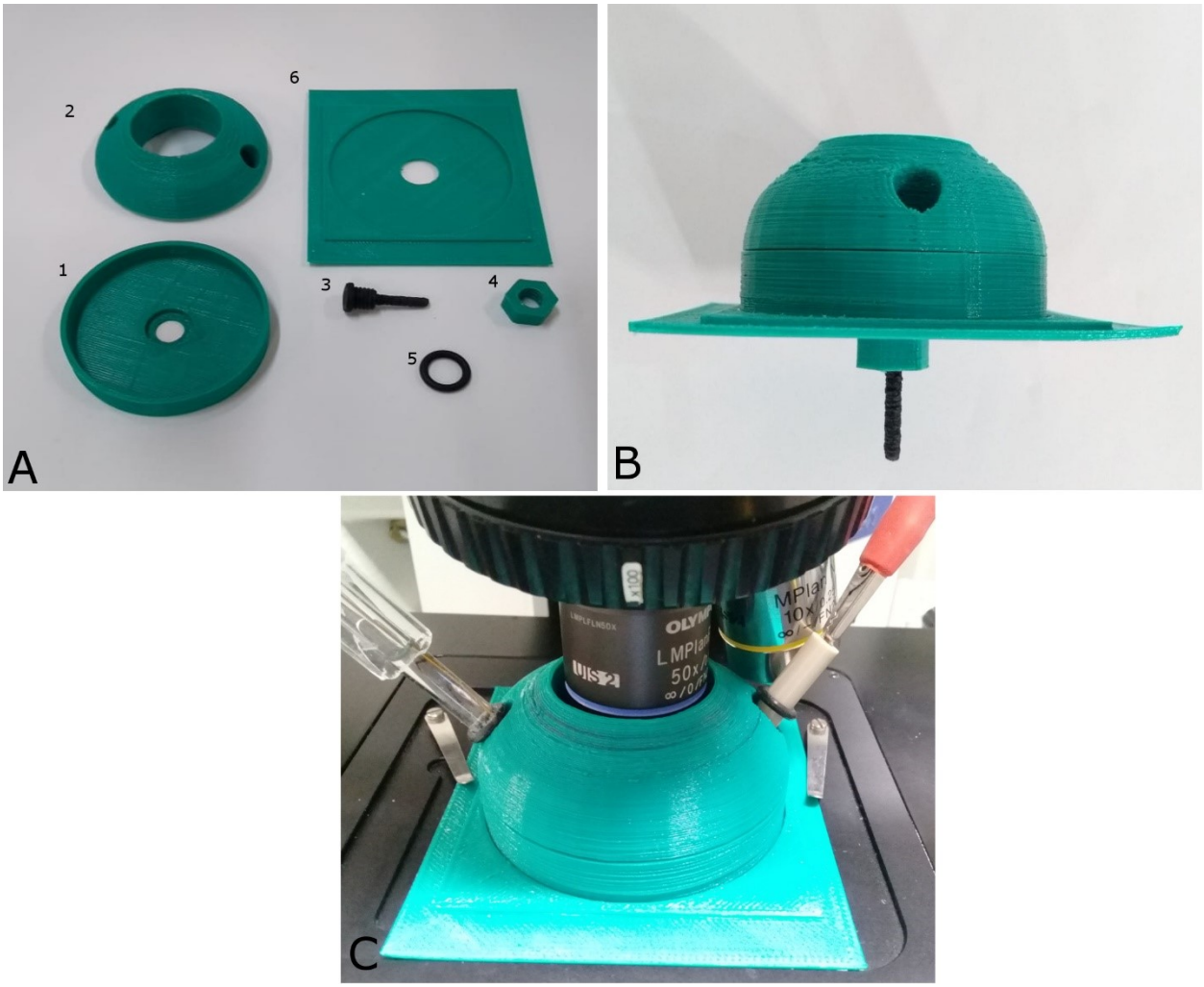

Figure 38: Real representation of spectroelectrochemical cell: A) Components of the 3D printed cell: (1) cell cup, (2) cell cover, (3) graphene 3D screw - shaped working electrode (9.9 mm in diameter), (4) screw nut, (5) O-ring and (6) support for equipment, B) the lateral view of assembled spectroelectrochemical cell, C) 3D printed cell before Raman measurements, in left orifices reference electrode (Ag/AgCl) and in the right orifices counter electrode (platinum wire).

4.2.2 Modification of 3D printed electrode

Before electrochemical and spectroelectrochemical experiments using Prussian blue (PB), the 3D graphene electrodes were submitted to an electrochemical pre-treatment, according to our unpublished results. Briefly, the surface of working electrode was oxidized (applying potential of 1.8 V *vs* Ag/AgCl for 15 minutes), and then reduced (by applying potential of -1.8 V *vs* Ag/AgCl for 50 seconds). Afterwards, the modified electrodes were prepared by casting of 500 µL of suspension (2 mg mL-1) of PB, prepared according to a previous report [46].

4.2.3 Characterization

The morphologies of the 3D graphene electrodes before and after the electrochemical functionalization were investigated by FEI Quanta 250 field emission scanning electron microscope (FE-SEM) from FEI Co., USA, operating at 2.0 kV. The Raman spectra of the electrodes were recorded at room temperature using a Confocal T64000 spectrometer from Jobin Yvon with a solid-state sapphire laser (532 nm).

4.2.4 Spectroelectrochemical analysis

Spectroelectrochemical measurements were performed using the setup presented in Figure 38. Electrochemical measurements were carried out by a portable bipotentiostat/galvanostat mSTAT400 (DropSens, Spain) controlled by DropView 8400 2.1 software. Simultaneously to the electrochemical analysis, Raman spectra were recorded at room temperature using a Confocal T64000 spectrometer from Jobin Yvon with a solid-state sapphire laser (532 nm, 25mW), resolution of 2.9 cm^{-1}, with a 50xLWD objective.

For PB modified 3D printed graphene electrode, the first spectrum was recorded under open circuit condition (OCP) in solution of 0.1 mol L^{-1} HCl and 0.1 mol L^{-1} KCl. Then, recording sequence started by applying potential of -0.5 V *vs* Ag/AgCl up to 1.2 V *vs* Ag/AgCl, increasing for 0.1 V. Potentials were applied for 20 minutes and single scan was acquired for 30 s, in the range of 2200-2000 cm^{-1}. After each measurement the equipment was disconnected for 15 minutes.

Raman-assisted electrochemical functionalization of 3D printed graphene electrode was performed by chronoamperometry in 0.1 mol L^{-1} PBS under an applied

potential of +1.8 V *vs* Ag/AgCl for 16 minutes. Simultaneously, Raman spectra were collected under OCP, initial condition, and after 2, 4, 8, 12 and 16 minutes. The spectra were recorded using a solid-state sapphire laser (532 nm, 40 mW) and a 50x LWD objective with an integration time of 120 s in the range of 1250-1750 cm^{-1}. All Raman spectra were recorded after instrument calibration with silicon (~ 520.7 cm^{-1}).

4.3 Results and discussion

4.3.1 Morphology of the bare and PB modified working electrode

The morphology of the electrodes was investigated by FE-SEM. In accordance with out previous work [40], the electrochemically pre-treated 3D printed graphene electrode presented a rough surface, as can be seen in Figure 39-A. After the modification with PB, the surface was covered with cubic and spherical micrometric particles, Figure 39-B.

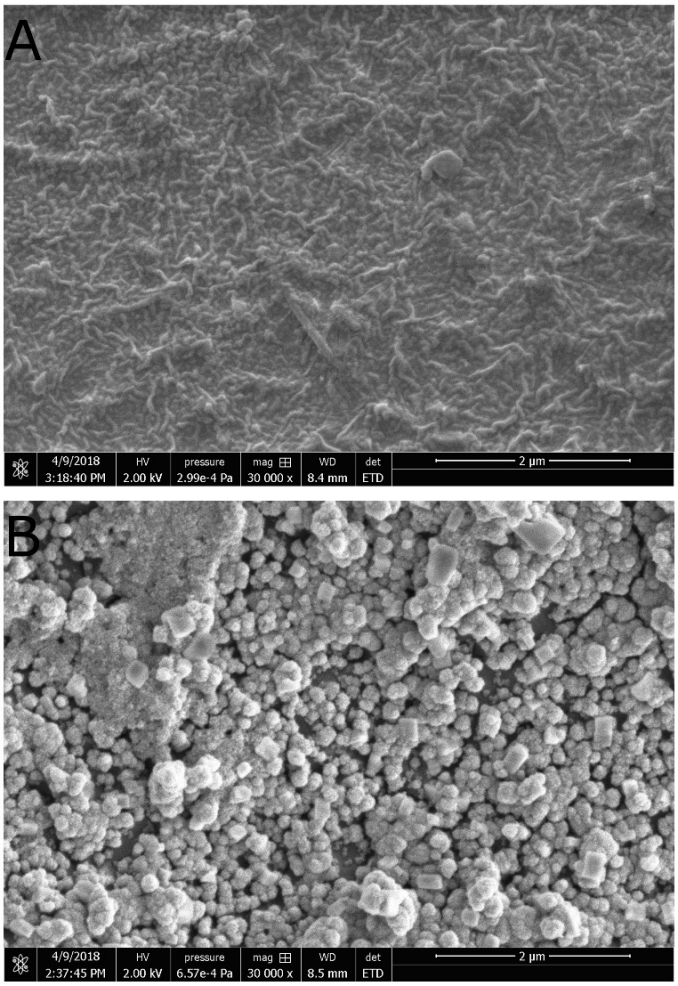

Figure 39: Field emission scanning electron microscopy (FE-SEM) micrographs of A) the electrochemically oxidized 3D graphene electrode at +1.8 *vs* Ag/AgCl then reduced at -1.8 *vs* Ag/AgCl, B) PB modified 3D electrode after oxidation and reduction pre-treatment.

4.3.2 Monitoring structural changes of Prussian blue during electrochemical measurements

To evaluate the applicability of the cell, PB was chosen as the electrode modifier due to its well-known redox properties [12]. Typical cyclic voltammogram of PB modified 3D electrode at slow scan rate (5 mV s^{-1}) is presented in Figure 40. As it can be seen two distinct well-defined pairs of redox peaks were observed. The peak at E_0 = +0.2 V *vs* Ag/AgCl corresponds to the oxidation of Prussian White (PW) to Prussian blue (PB) Eq .5, (Chapter 1) $Fe^{II}/Fe^{II} \rightarrow Fe^{III}/Fe^{II}$) and the peak with E_0= +0.9 V *vs*. Ag/AgCl is ascribed to oxidation of PB to Berlin Green (BG) according to Eq. 6 (Chapter 1) ($Fe^{III}/Fe^{II} \rightarrow Fe^{III}/Fe^{III}$).

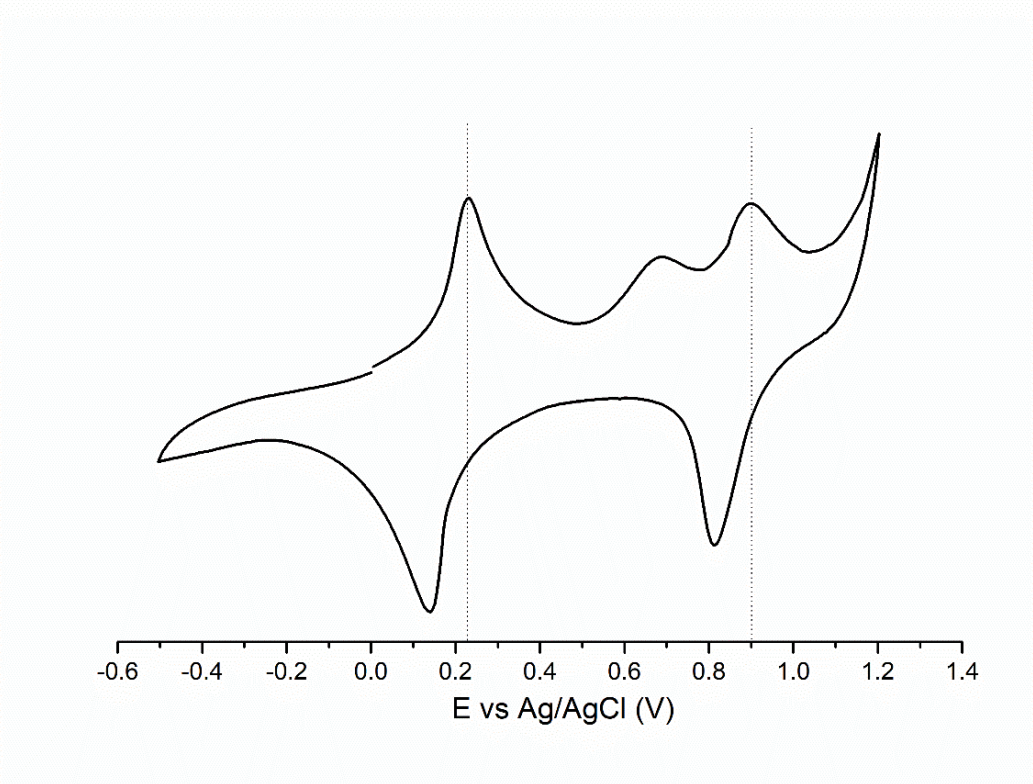

Figure 40: Cyclic voltammogram of PB modified 3D electrode recorded at scan rate of 5 mV s^{-1} in 0.1 mol L^{-1} HCl (pH=1) and 0.1 mol L^{-1} KCl.

Raman spectroscopy is frequently used for PB characterization, since these compounds have characteristic ν(CN), C≡N stretching, band between 2200 and 2000 cm^{-1} [110]. The frequency of ν (CN) is directly related to the oxidation state of the metal cation coordinated to the cyanide. Consequently, the ν (CN) is shifted to higher frequencies when the metals on its structure are oxidize [111,112]. The cyanide groups act as σ-donor and an increase of the strength of the cyanide bond is observed due to an increasing metal charge. Therefore, the electron density from the antibonding orbital is reduced in the cyanide bond, strengthening the cyanide bond and increasing its vibrational frequency [113]. The band at lower frequencies (~ 2091 cm^{-1}) is assigned to a ν (CN) mode associated to Fe(II) cation, and the higher frequency band (~ 2154 cm^{-1}) is assigned to Fe(III) cation [112,114].

In-situ Raman spectra of PB on the 3D graphene electrode are shown in Figure 41, obtained within a broad electrode potential window ranging from -0.5 V to 1.2 V vs. Ag/AgCl. The spectra have been normalized and limited between 2200 and 2000 cm^{-1} to investigate the shift of the characteristic ν (CN) band of PB. The alterations of the

frequencies of C≡N stretching band as a function of the applied potential are described in detail in

Table 15.

Spectra acquired under potentials close to 0.2 V and 0.9 V *vs* Ag/AgCl can be considered a mixed PW-PB and PB-BG phases, respectively, Figure 40. The spectra recorded at potentials distanced from these values can be considered as pure PW and BG, respectively. The cyanide ligand of PW, PB and BG is coordinated to iron ions of different formal oxidation states. Thus, Fe^{II}-CN- Fe^{II} for PW, Fe^{III}-CN- Fe^{II} for PB and Fe^{III}-CN- Fe^{III} for BG. This change in the chemical environment of C≡N group causes shifts in its vibration frequency.

The first spectrum acquired, obtained under OCP conditions in solution, presents “pure PB” as the predominant phase, with corresponding bands located at 2056 cm^{-1} and 2092 cm^{-1}. Similar bands of PB at 2056 cm^{-1} and 2094 cm^{-1} were reported under 785 nm excitation [114]. The *in-situ* measurements started by applying negative potentials from -0.5 V. In cathodic potentials, ranging from -0.5 V to -0.1 V, two characteristic bands appear approximately at 2141 cm^{-1} and 2110 cm^{-1} (Figure 41-A, Table 15). When -0.3 V and -0.4 V were applied, the third band arose located at 2050 and 2056 cm^{-1}, respectively. In this potential range, PW is the dominant phase. Very similar bands of PW have been reported at 2132, 2095 and 2048 cm^{-1} under 785 nm excitation [114].

With an increase in applied potential, the band close to 2150 cm^{-1} increases and the band at c.a. 2110 cm^{-1} decreases in intensity, indicating the formation of PB. In a potential range from 0.1 V to 0.7 V PB is the predominant phase, with bands located close to 2156 and at 2120 cm^{-1} (Figure 41-A,Table 15). The first band corresponds to the same band observed under OCP conditions.

According to Samain et al. [112], BG exhibits a broad band located at 2049 cm^{-1}, and two shoulders located at 2090 and 2140 cm^{-1}. As it can be seen from the cyclic voltammogram presented in Figure 40, the PB oxidizes to BG at 0.9 V vs. Ag/AgCl. A slow transition is expected from PB to BG to occur upon application of 0.9 V. As it can be seen in Table 15 the band at 2156 cm^{-1} shifted to lower values only when 1.2 V was applied. However, the shoulder located approximately at 2090 cm^{-1}

was observed at potential 0.9 V, indicating that oxidation to BG begun to occur. The complete oxidation from PB to BG would probably occur if the cathodic potential was applied for more than 20 minutes. Since, the area of electrode is large, it takes more time for the complete oxidation of PB to BG.

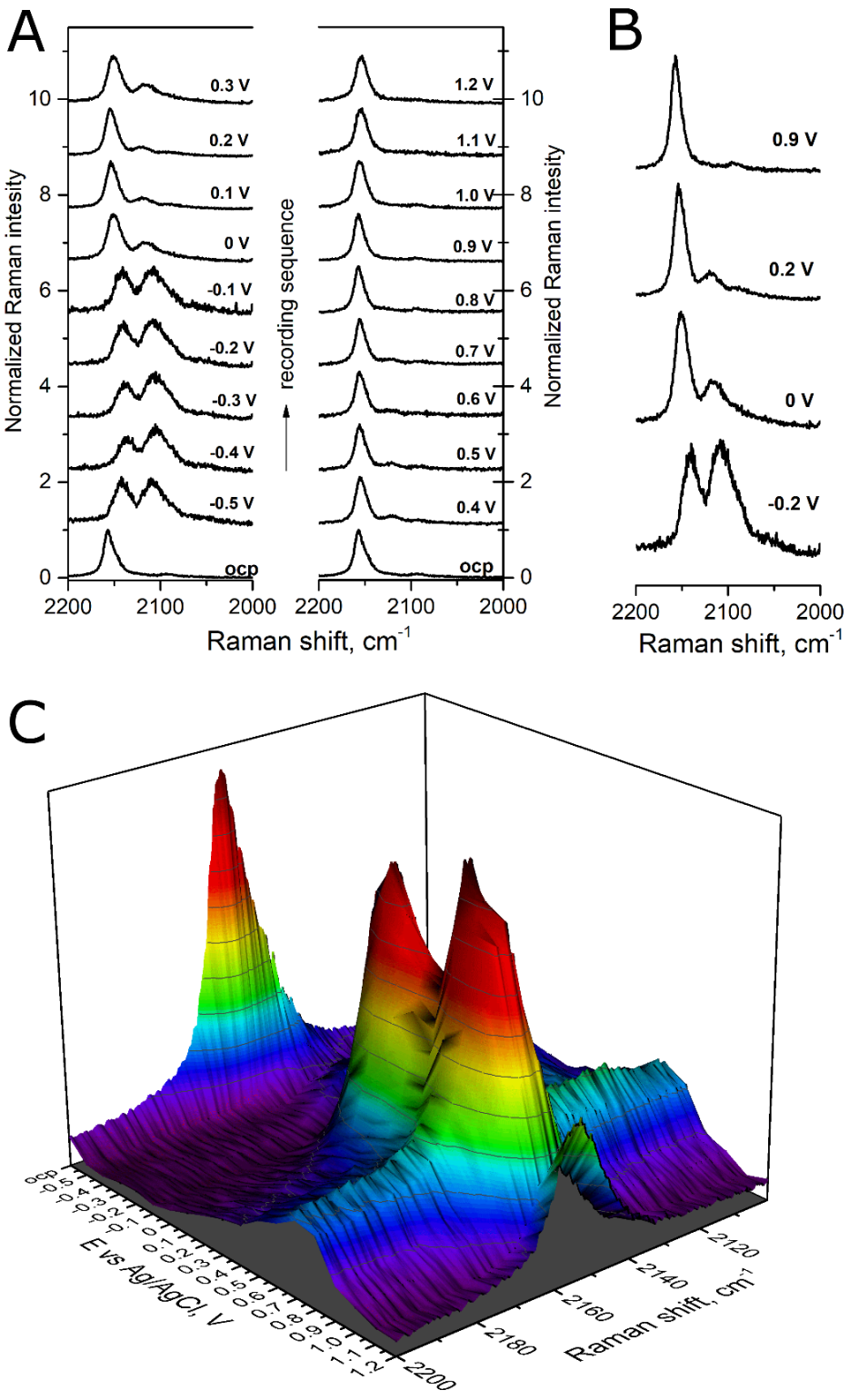

Figure 41: Raman spectra of PB modified 3D graphene electrodes A) Overall spectra recorder at electrode potential ranging from -0.5 V to 1.2 V *vs* Ag/AgCl, at excitation wavelength of 532 nm (25mW). B) the most pronounced shifts in ν(CN) vibrational modes, bands depicted without potential (OCP) and at applied potentials of

-0.2, 0 V, 0.2 V and 0.9 V *vs*. Ag/AgCl C) 3D illustration of Raman spectra, recorded in potential range between – 0.5 V and 1.2 V *vs* Ag/AgCl.

Table 15: Alteration in CN^- stretching band with applied potential.

Potential applied, V *vs* Ag/AgCl	Wavenumber, cm^{-1}		
ocp	2156	2092	-
-0.5	2141	2110	-
-0.4	2135	2108	2050
-0.3	2139	2108	2056
-0.2	2142	2109	
-0.1	2141	2109	2065
0	2150	2117	-
0.1	2153	2118	
0.2	2154	2121	
0.3	2154	2121	
0.4	2155	2120	
0.5	2155	2120	
0.6	2156	2123	
0.7	2155	2125	
0.8	2156	2093	-
0.9	2157	2093	-
1.0	2156	2093	-
1.1	2154	2089	-
1.2	2154	2094	

4.3.3 Raman-assisted electrochemical functionalization of 3D printed graphene electrode (3DGrE)

The presence of functional groups plays an important role in the modulation of the electrochemical properties of graphene [115]. For example, graphene oxide [116] has shown superior performance when compared to graphene [115] in electroanalysis, due to the specific interactions between oxygen functionalities and the analyte of interest.

Additionally, a wide range of materials can be attached to the functionalized graphene to prepare composites with synergistic properties [116,117]. Thus, electrochemical techniques have been reported as simple, fast and green approaches to prepare graphene oxide on the surface of glassy carbon electrode [118]. In our previous work, we have used a simple electrochemical oxidation/reduction pre-treatment of 3D printed graphene electrodes to improve their electrocatalytic properties [40]. The good performance of the electrodes was attributed to the increase of structural defects/disorders, the presence of oxygen functionalities and the exposure of graphene sheets on the surface.

As it can be seen in Figure 42 A-B the surface of the electrode became rough after the electrochemical pre-treatment, probably due to insertion of oxygen functional groups into the graphene structure, increasing the distance between the graphene layers, which were compacted in the polymeric matrix. Raman spectra obtained before and after the electrochemical functionalization (Figure 42 -C) confirms the increase of the structural defects, due to the increase of the ratio between bands D and G intensities (I_D/I_G). The D (~ 1350 cm^{-1}) and G (~ 1580 cm^{-1}) bands are attributed to out-of-plane vibrational mode of the graphene network and sp^2 in-plane carbon vibrations, respectively. Thus, the I_D/I_G ratio, is an indication of the level of disorder/defects in graphene sheets [119–121].

For better understanding of the structural changes of graphene during the electrochemical treatment and to achieve the best experimental condition, such as the applied potential and the reaction time, the reaction can be assisted by *in situ* Raman spectroscopy. In this sense, electrochemical oxidation of the 3DGrE was investigated using the proposed spectroelectrochemical cell.

According to Figure 42-D the intensity of the D band increases till the 12th minute. The I_D/I_G ratio in OCP conditions was 0.58, increasing to 0.67, 0.70, 0.72, 0.80 and 0.79 after application of +1.8 V *vs* Ag/AgCl for 2, 6, 8, 12 and 16 minutes, respectively. As disorder increases, the I_D/I_G increases due to insertion of oxygen

functional groups promoted by the electrochemical treatment, affecting the band structure and the density of states (DOS) of the electrodes.

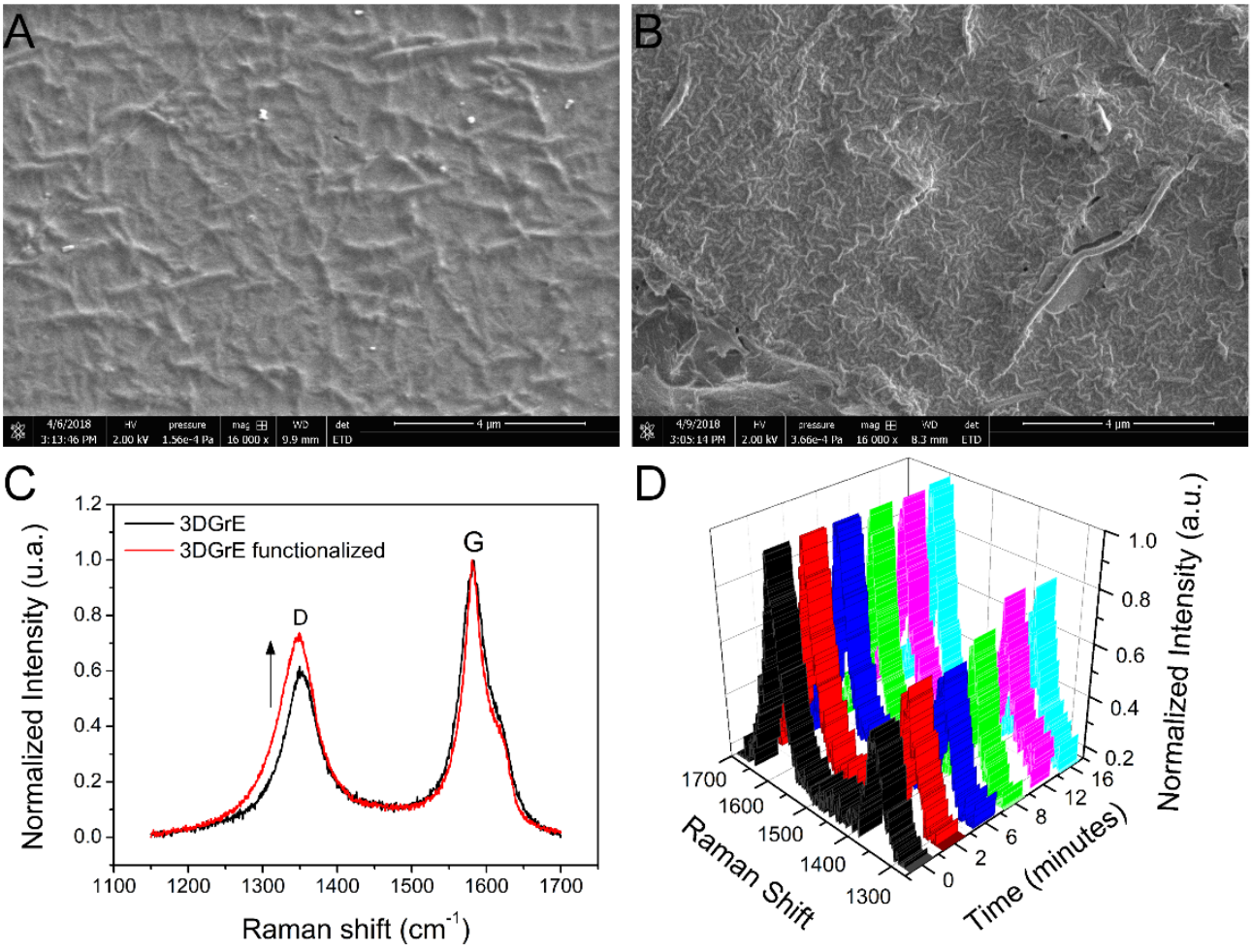

Figure 42: Field emission scanning electron microscopy (FEG-SEM) micrographs of the 3D printed graphene electrode A) before and B) after the electrochemical functionalization. C) Raman spectra of the samples presented in A and B. D) 3D illustration of Raman spectra of the 3DGrE collected in 0.1 mol L^{-1} PBS, using the spectroelectrochemical cell. The spectra were acquired simultaneously to chronoamperometry measurements, under OCP condition (t = 0) and under an applied potential of +1.8 V vs. Ag/AgCl (in 3 mol L^{-1} KCl) after 2, 4, 8, 12 and 16 minutes.

4.3 Conclusion

The 3D technique was used to print a simple, low-cost, robust 3D printed SEC and working electrode. The SEC was produced using cheap, inert ABS filament, whereas working electrode was printed using conductive PLA/ graphene filament. The reported SEC was designed intentionally for Raman measurements; therefore, its design was chosen to fit Raman lenses specifically. However, 3D printing is boundless when it comes to the shape and dimensions, therefore SECs for any kind of equipment can be easily produced. The proposed SEC is very cheap, as the whole printing process costed less than US$ 2 including working electrode and without reference and counter electrodes.

The 3D printed SEC was tested for *in situ* Raman measurements, with non-modified and PB modified working electrodes. It was possible to investigate the structural changes of PB during the redox process. In addition, from *in situ* electrochemical functionalization of graphene, a relationship between the number of structural defects and reaction time could be established. Therefore, *in situ* measurements facilitate the optimization of electrochemical parameters for obtention of electroactive surfaces. Moreover, the 3D printed SEC opens new possibilities to explore film formation, adsorption processes, kinetics of electrochemical reactions and electrocatalytic mechanism.

Chapter 5

Assembly of low-cost lab-made photoreactor for preparation of nanomaterials

5.1 Introduction

Photochemical methods for the preparation of nanomaterials have received great attention due to the possibility of temporal control, reaction rate modulation and

spatial adjust. Also, the photochemical reactions can be changed in stepwise even in mild condition [122].

Gold nanoparticles (AuNP), for example, can be synthesized using tetrachloroauric(III) acid, Irgacure™ 2959 (photoinitiator) and UV light [123]. This method allows the synthesis of unprotected AuNP in water with high reproducibility, high stability and a range of sizes controlled by the illumination intensity. Due to the reported features of these AuNP, it is possible to highlight their use in studies of SERS (Surface Enhanced Raman Scattering) effect, catalysis, photocatalysis and plasmonics. Also, the use of different wavelengths, in the photochemical synthesis, can lead to the formation of silver nanoparticles with different shape and size [124]. This process occurs directly by irradiation of silver ions or nanometric spherical seed of AgNP [125]

From the coordination chemistry point of view, the irradiation of nitroprusside under UV light leads to the production of Prussian blue nanoparticles and the modulation of the size can be performed by altering the light source and its intensity [126]. Another example of the application of UV-light in materials is the modulation of the electrochemical properties of the graphene oxide through the control of reduction level which can be adjusted by the intensity and time of irradiation [115]. Thereby, it is possible to make a fine and planned adjustment in the final properties of the graphene oxide, which is sometimes difficult to control using chemical methods. An overview of the main uses of light to produce or modulate properties of (nano) materials is presented in the Figure 43.

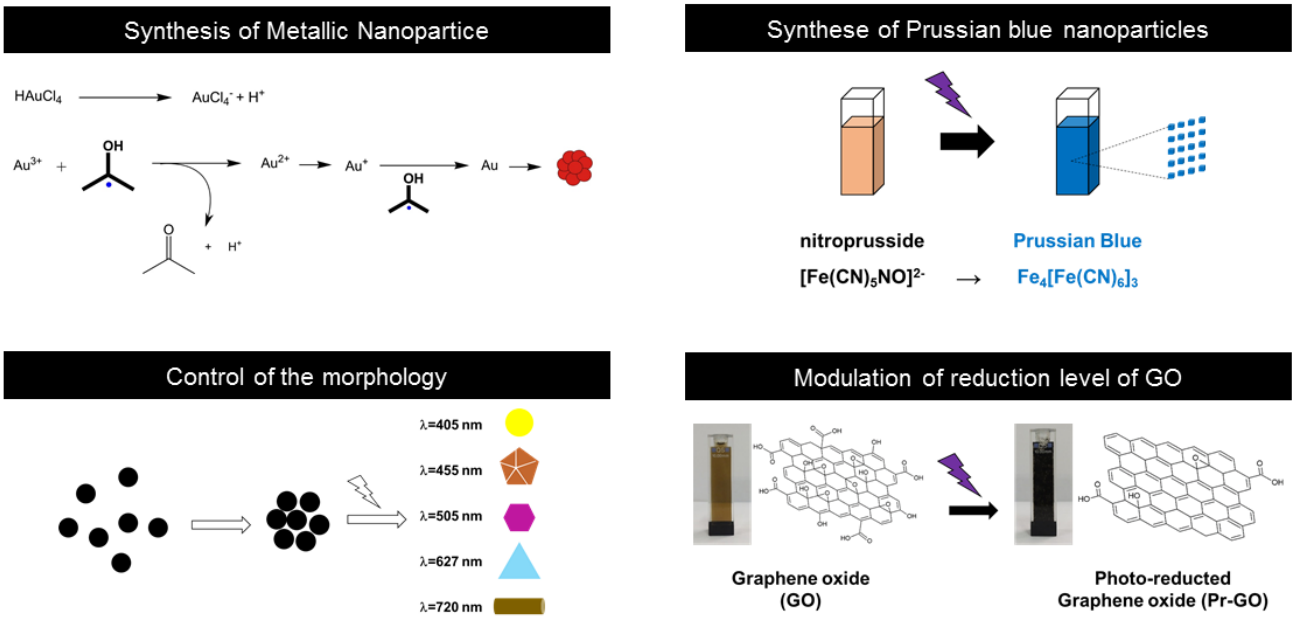

Figure 43: Overview of the main uses of light to produce (nano)materials *[127]*.

The use of light in chemistry goes beyond the preparation of materials and may be used in strategic areas ranging from medicine to energy. A simple UV-LED can be applied in generation of singlet oxygen and its quantification [128]. Light can contribute to environment when used in systems of photodegrading of waste or polluting [129,130]. Furthermore, light is converted directly in electricity [131] or its energy can be stored regarding chemical bonding as in water splitting process [132].

One of the strategies to work with light in preparation of nanomaterials is the utilization of the photoreactors. They offer the possibility to control the wavelength of light source, the power and the time of reaction. The atmosphere and the stirring can also be controlled, and all process must be performed in closed system to protect the users from light exposure. A main disadvantage of photoreactors are their cost that is sometimes high for research laboratories. Due to the importance of the use of light in chemistry and material chemistry we are reporting how to construct a low-cost lab-made photoreactor.

5.2 Experimental section

5.2.1 Design of the lab-made photoreactor

The lamps used in photoreactor (PR) were UV-A (Sylvania, 8W) and UV-C (Sankyo Denki, 8W). The lamps reactors used in the PR were Econoluz EC-1X8W. The PR was equipped with the timer model CT4S-1P (Autonoics).

The PR was designed using six steel plates arranged in a rectangular prism shape with dimensions described in Figure 44. The frontal steel plate has an opening of 336.0 cm^2 where a 31.0 cm wide reaction chamber was constructed.

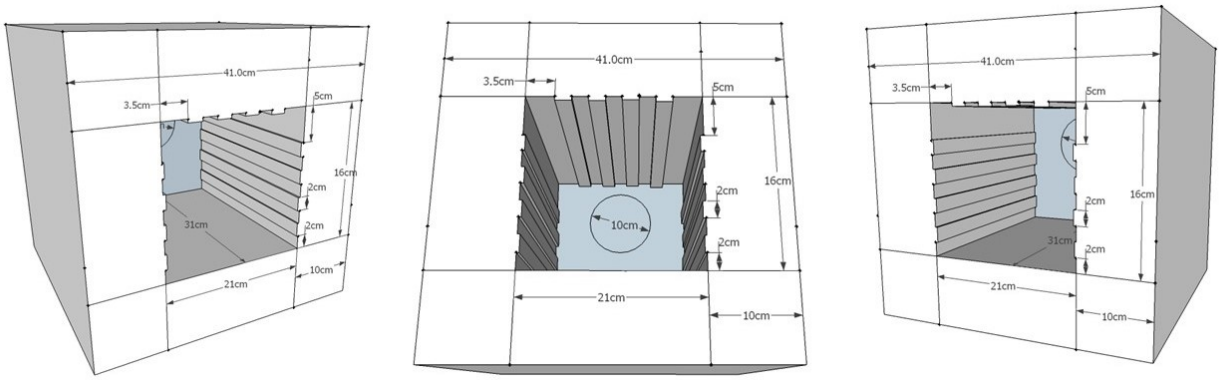

Figure 44: Sketch of photoreactor draw in SketchUp™ software.

The inner walls of the chamber were made of steel coated with a temperature resistant paint. As can be seen in the Figure 45, a timer with a push button and an on/off switch were installed for time monitoring and start of the system, respectively.

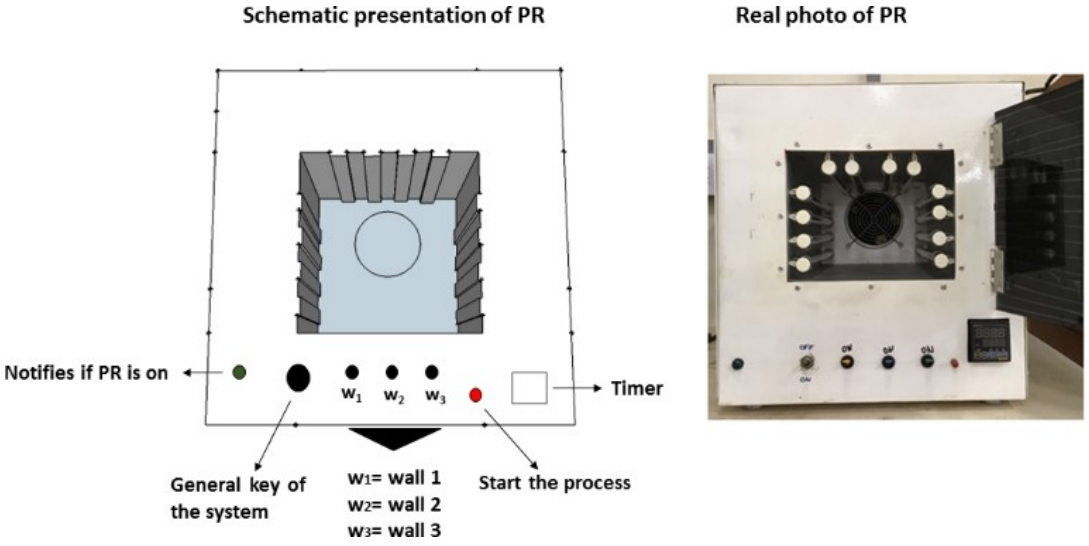

Figure 45: Scheme and digital photo of the lab-made photoreactor used for production of gold nanoparticles and photo-reduction of graphene oxide.

An acrylic plate of dimensions (30 x 24 cm) coated with black plastic film was used to cover the door to avoid light exposure by the user (Figure 46-A). A pilot lamp was fixed to indicate the on/off operation of the system. Lamps sockets for four lamps (8 W, 30 cm) were installed on each of the lateral and upper walls on the inner side of the chamber (Figure 46-B). Also, a handle was attached to the top of the reactor for handling and transport. (Figure 46-C).

The electronic part was designed in such a way that each of the four lamp sets could be triggered individually or simultaneously via switches, modulating the intensity of the emitted light. The lamps reactors were linked in parallel way (Figure 46 D-E). The sockets of the lamps allowed them to be easily replaced with others of different wavelengths, such as UV-A and UV-C. The heat dissipation was performed by an 8 W fan cooler. A 220 V supply powered the whole system. The expert technicians of Institute of Chemistry (UNICAMP) have assisted in the assembly of the photoreactor.

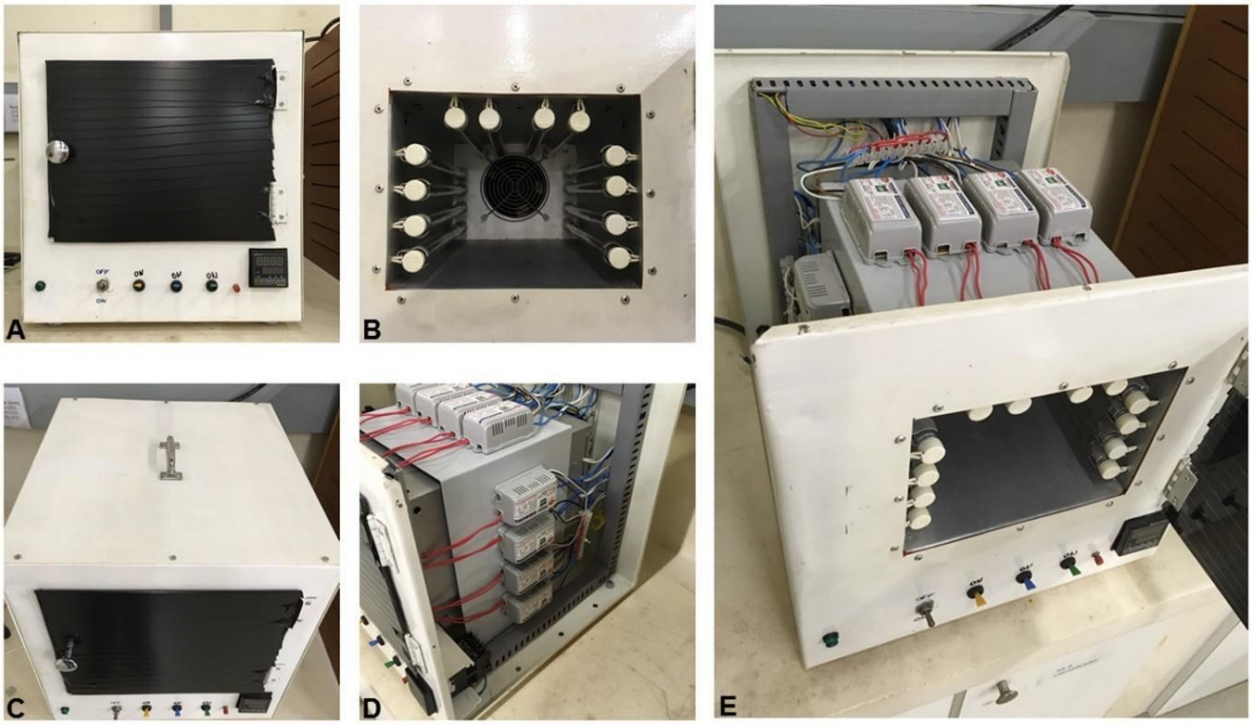

Figure 46: Digital photos of A) frontal view of lab-made photoreactor with closed door and B) with opened door, C) upper view with the handle and D, E) disassembled reactor showing the parallel arrangement of the lamp reactors.

5.2.2 Synthesis of gold nanoparticles

The preparation of gold nanoparticle (GNP) following the procedure described in literature [123]. Briefly, 0.33 mM gold (III) chloride trihydrate ($HAuCl_4.3H_2O$) was mixed with 1.0 mM Irgacure™ (1-[4-(2-hydroxyethoxy)phenyl]-2-hydroxy-2-methyl- 1-propane-1-one) I-2959 in water. The mixture was added to 24-well plates and irradiated for 15 minutes in the photoreactor. The Sylvania UV-A lamps were used, since Irgacure™ I-2959 forms radicals upon excitation at λ = 350 nm. The well plates or cuvettes should be placed in the center of the photoreactor to guarantee the homogeneity of light. An important observation is to put the well plates in the same place to obtain reproducible results.

5.2.3 Photochemical reduction of graphene oxide

Graphite oxide was synthesized using a modified Hummer's method [115] and graphene oxide (GO) was obtained by exfoliation of graphite oxide using an ultrasonic bath for 10 minutes. Photochemical reduction of graphene oxide was performed under UV-A and UV-C lamps in the lab-made photoreactor by irradiation of GO (1.0 mg mL^{-1}) for 12h and 24h in quartz cuvettes. The well plates also can be used for this purpose. We have obtained good results using quartz cuvettes and a volume of 3 mL per batch.

5.2.4 Characterization

Spectroradiometer LuzChem SPR-4002 was used to obtain the absorption spectra and power of the UV-A and UV-C lamps. UV-Vis spectra of the synthesized nanomaterials were recorded on a HP Agilent 8453 spectrophotometer.

5.3 Results and discussion

The lab-made photoreactor was powered by UV-A or UV-C for the syntheses of nanomaterials. The emission spectra of UV-A and UV-C spectra are presented in the Figure 47.

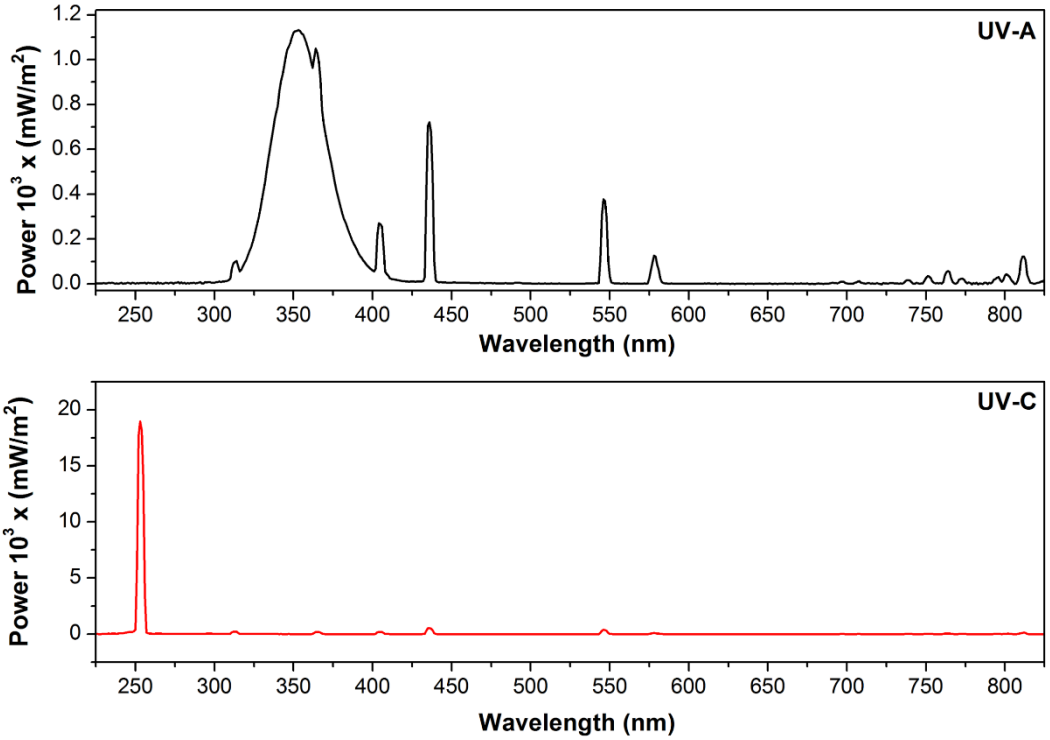

Figure 47: Emission spectra of UV-A and UV-C lamps.

The UV-A lamp emits in a broad region between 300 and 850 nm, with the maximum at 350 nm. The UV-C lamp emits the most of its total irradiation at 254 nm.

Scaiano *et al.* [125] reported a synthesis of unprotected aqueous gold nanoparticles prepared in minutes with a commercial photoreactor (Luzchem LZC-4V or LZC-ORG). By comparison, we have synthesized gold nanoparticles (AuNP) using the same procedure in our lab-made photoreactor. AuNP were synthesized with photoinitiator Irgacure™ I-2959 in excess to generate enough acetone ketyl radicals to reduce tetrachloroaurate and form nanoparticle [133]. Extinction spectra from Figure 48 shows surface plasmon band with an extinction peak close to 530 nm indicating the size close to 12 nm, which has been confirmed by TEM microscopy (an inset of Figure 48). It was possible to synthesize reproducible gold nanoparticles in a very short period (15 minutes of irradiation) with

efficiency comparable to commercial photoreactors, but with a final cost much lower than those available in the market.

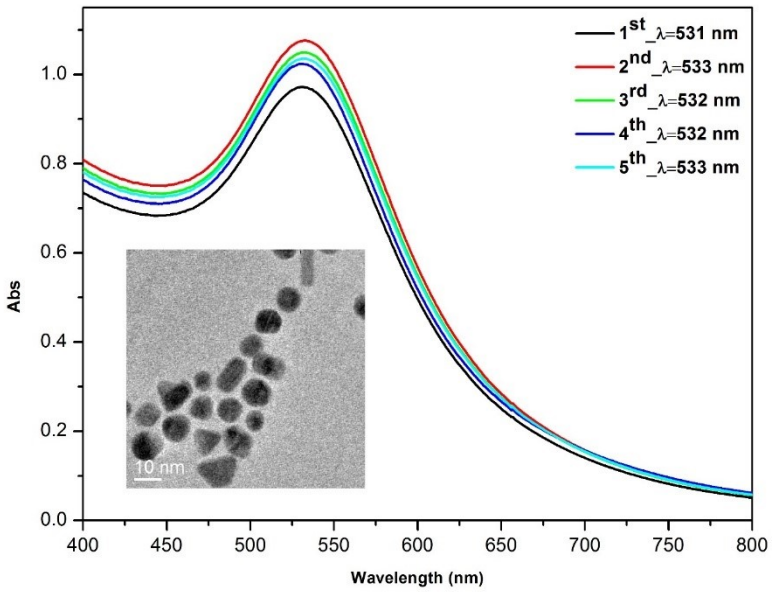

Figure 48: Extinction spectra of AuNP synthesized five times with a 5 minutes interval between each synthesis. The AuNP were prepared with 0.33mmol L^{-1} $HAuCl_4$ and 1.0 mmol L^{-1} Irgacure 2959 in 24-well plates at 15 minutes UV-A exposure. Insert: TEM images of AuNP.

Another example of use of the lab-made photoreactor is related to the photochemical reduction of graphene oxide. This process is simple and effective in tuning the percentage of oxygenated groups and consequently the physical and chemical properties of the reduced graphene oxide (rGO). The photoreduction can be accompanied by changes in the electronic spectrum of the graphene oxide. As shown in Figure 49, the electronic spectrum of the GO has two characteristic bands in UV-Vis region. The first one at 234 nm is assigned to $\pi \rightarrow \pi^*$ (transitions of aromatic C=C bonds) and the second one is a shoulder at 310 nm assigned to $n \rightarrow \pi^*$ (transition of C=O bonds) [134]. When GO is reduced to rGO, the band at 234 nm undergoes a red-shift and the shoulder at 310 nm disappears.

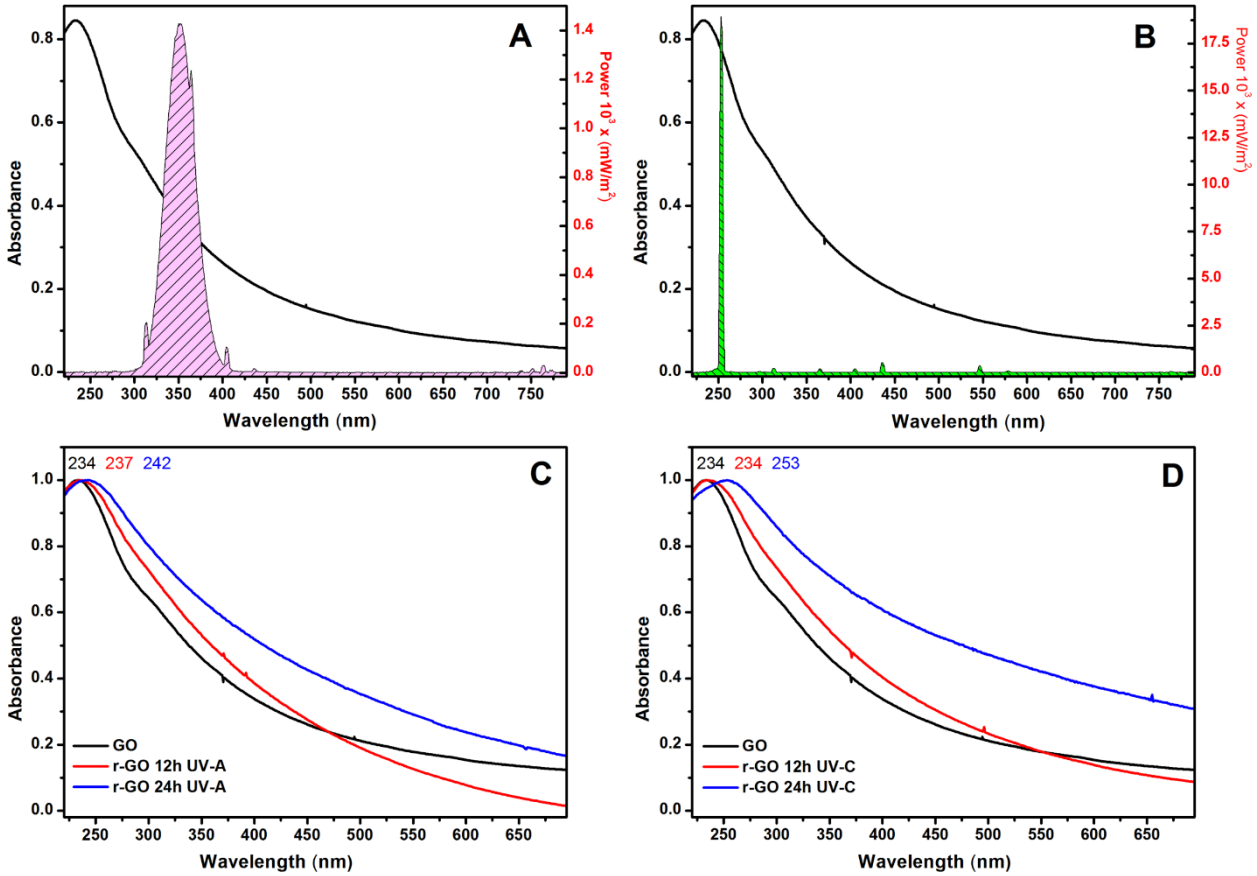

Figure 49: The observed differences between electronic spectra of graphene oxide after irradiated by A) UV-A lamps and B) UV-C lamps. UV-Vis absorption spectra of GO before and after 12h and 24h of irradiation with C) UV-A lamps and D) UV-C lamps.

The reduction degree increases with the irradiation time and is more pronounced for the irradiation by UV-C lamps. Upon excitation by light with enough energy to overcome the value of the bandgap of graphene oxide, electron–hole pairs are generated in the conduction and the valence bands of GO, respectively. The main process observed in the irradiation of GO by UV light is the reduction of GO nanosheets by the photogenerated electrons. On the other hand, the holes produced by light contribute to the oxidation of the C skeleton to CO_2, but in minor proportion than the reduction [115,135]. The excitation with highly energetic light (UV-C) leads to the formation of a greatly reduced material and reduction level of GO can be controlled by setting the parameter such as time of irradiation, power of the lamp and wavelength.

5.4 Conclusion

We have described a procedure to assemble a lab-made photoreactor with low cost and similar efficiency when compared with commercial one. The pieces and electronic components can be found easily on the market, and an electronic technician or expert in electronics can set up a photoreactor.

The size and power of the equipment will depend on the proposed use. De scribed photoreactor is suitable for synthesis of metallic nanoparticles, as gold nanoparticles, using environmentally friendly approach. The photoreactor also is suitable for controlling the photoreduction level of graphene oxide under mild conditions.

5. Overall conclusion and further perspectives

The electrochemical and structural properties of Prussian blue and its analogs make this class of materials very versatile emphasizing its application in sensing devices. Through work this remarkable material was principal focus of our research, especially its electrochemical behavior. Five different substrates have been used and it each of them was successfully modified with Prussian blue.

Additionally, cheap spectroelectrochemical cell was designed and created using 3D printed. The cell was built with intuition to follow *in operando* conditions the electroactive species. Working electrode was printed, also, using conductive graphene filament. The electrode and spectroelectrochemical cell were designed to fit within Raman equipment. With simple electrochemical pre – treatment, the surface of electrode was functionalized, allowing Prussian blue to be anchored and to further study in situ its redox behavior.

Even though, a lot of concepts were explored during these four years, still there are some unanswered questions. For an example, the studies related to electrocatalytic reduction of hydrogen peroxide with Prussian blue modified gold, platinum and glassy carbon electrodes. The sensing of peroxide with these electrodes is explored in literature to great extent. With these results, we will compare to those we already have with 3D graphene modified electrode and have better insight to this new material.

6. References

[1] K. Kalantar-zadeh, B. Fry, eds., Sensor Characteristics and Physical Effects, in: Nanotechnology-Enabled Sensors, Springer US, Boston, MA, 2008: pp. 13–62. doi:10.1007/978-0-387-68023-1_2.

[2] Y.-B. Hahn, R. Ahmad, N. Tripathy, Chemical and biological sensors based on metal oxide nanostructures, Chemical Communications. 48 (2012) 10369. doi:10.1039/c2cc34706g.

[3] A.J. Bandodkar, J. Wang, Non-invasive wearable electrochemical sensors: a review, Trends in Biotechnology. 32 (2014) 363–371. doi:10.1016/j.tibtech.2014.04.005.

[4] A. Hulanicki, S. Glab, F. Ingman, Chemical sensors: definitions and classification, Pure and Applied Chemistry. 63 (1991) 1247–1250. doi:10.1351/pac199163091247.

[5] A. Pandikumar, G.T. Soon How, T.P. See, F.S. Omar, S. Jayabal, K.Z. Kamali, N. Yusoff, A. Jamil, R. Ramaraj, S.A. John, H.N. Lim, N.M. Huang, Graphene and its nanocomposite material based electrochemical sensor platform for dopamine, RSC Adv. 4 (2014) 63296–63323. doi:10.1039/C4RA13777A.

[6] A. C., A. Morri, Electroanalytical Sensor Technology, in: M. Khalid (Ed.), Electrochemistry, InTech, 2013. doi:10.5772/51480.

[7] S. Husmann, E. Nossol, A.J.G. Zarbin, Carbon nanotube/Prussian blue paste electrodes: Characterization and study of key parameters for application as sensors for determination of low concentration of hydrogen peroxide, Sensors and Actuators B: Chemical. 192 (2014) 782–790. doi:10.1016/j.snb.2013.10.074.

[8] W.P. Griffith, Cyanide complexes of the transition metals, Quarterly Reviews, Chemical Society. 16 (1962) 188. doi:10.1039/qr9621600188.

[9] J. Nai, X.W.D. Lou, Hollow Structures Based on Prussian Blue and Its Analogs for Electrochemical Energy Storage and Conversion, Advanced Materials. (2018) 1706825. doi:10.1002/adma.201706825.

[10] A. Paolella, C. Faure, V. Timoshevskii, S. Marras, G. Bertoni, A. Guerfi, A. Vijh, M. Armand, K. Zaghib, A review on hexacyanoferrate-based materials for energy storage and smart windows: challenges and perspectives, Journal of Materials Chemistry A. 5 (2017) 18919–18932. doi:10.1039/C7TA05121B.

[11] S.-H. Lee, Y.-D. Huh, Preferential Evolution of Prussian Blue's Morphology from Cube to Hexapod, Bulletin of the Korean Chemical Society. 33 (2012) 1078–1080. doi:10.5012/bkcs.2012.33.3.1078.

[12] F. Ricci, G. Palleschi, Sensor and biosensor preparation, optimisation and applications of Prussian Blue modified electrodes, Biosensors and Bioelectronics. 21 (2005) 389–407. doi:10.1016/j.bios.2004.12.001.

[13] B. Kong, C. Selomulya, G. Zheng, D. Zhao, New faces of porous Prussian blue: interfacial assembly of integrated hetero-structures for sensing applications, Chemical Society Reviews. 44 (2015) 7997–8018. doi:10.1039/C5CS00397K.

[14] A.A. Karyakin, Prussian Blue and Its Analogues: Electrochemistry and Analytical Applications, Electroanalysis. 13 (2001) 813–819. doi:10.1002/1521-4109(200106)13:10<813::AID-ELAN813>3.0.CO;2-Z.

[15] J. Agrisuelas, J.J. García-Jareño, D. Gimenez-Romero, F. Vicente, Insights on the Mechanism of Insoluble-to-Soluble Prussian Blue Transformation, Journal of The Electrochemical Society. 156 (2009) P149. doi:10.1149/1.3177258.

[16] J. Vidal, Amperometric cholesterol biosensors based on the electropolymerization of pyrrole and the electrocatalytic effect of Prussian-Blue layers helped with self-assembled monolayers, Talanta. 64 (2004) 655–664. doi:10.1016/j.talanta.2004.03.038.

[17] C. Wang, L. Zhang, Z. Guo, J. Xu, H. Wang, H. Shi, K. Zhai, X. Zhuo, A New Amperometric Hydrazine Sensor Based on Prussian Blue/Single-walled Carbon Nanotube Nanocomposites, Electroanalysis. 22 (2010) 1867–1872. doi:10.1002/elan.201000058.

[18] K.-C. Ho, C.-Y. Chen, H.-C. Hsu, L.-C. Chen, S.-C. Shiesh, X.-Z. Lin, Amperometric detection of morphine at a Prussian blue-modified indium tin oxide electrode, Biosensors and Bioelectronics. 20 (2004) 3–8. doi:10.1016/j.bios.2003.11.027.

[19] Y. Zhang, B. Huang, F. Yu, Q. Yuan, M. Gu, J. Ji, Y. Zhang, Y. Li, 3D nitrogen-doped graphite foam@Prussian blue: an electrochemical sensing platform for highly sensitive determination of H2O2 and glucose, Microchimica Acta. 185 (2018). doi:10.1007/s00604-017-2631-3.

[20] T.S.T. Balamurugan, V. Mani, C.-C. Hsieh, S.-T. Huang, T.-K. Peng, H.-Y. Lin, Real-time tracking and quantification of endogenous hydrogen peroxide production in living cells using graphenated carbon nanotubes supported Prussian blue cubes, Sensors and Actuators B: Chemical. 257 (2018) 220–227. doi:10.1016/j.snb.2017.10.151.

[21] M. Giorgio, M. Trinei, E. Migliaccio, P.G. Pelicci, Hydrogen peroxide: a metabolic by-product or a common mediator of ageing signals?, Nature Reviews Molecular Cell Biology. 8 (2007) 722–728. doi:10.1038/nrm2240.

[22] P.L. dos Santos, V. Katic, K.C.F. Toledo, J.A. Bonacin, Photochemical one-pot synthesis of reduced graphene oxide/Prussian blue nanocomposite for simultaneous electrochemical detection of ascorbic acid, dopamine, and uric acid, Sensors and Actuators B: Chemical. 255 (2018) 2437–2447. doi:10.1016/j.snb.2017.09.036.

[23] K. Itaya, N. Shoji, I. Uchida, Catalysis of the reduction of molecular oxygen to water at Prussian blue modified electrodes, Journal of the American Chemical Society. 106 (1984) 3423–3429. doi:10.1021/ja00324a007.

[24] H. Li, Y. Ban, Q. Gao, Q. Wei, A New Hydrogen Peroxide Sensor Based on Prussian Blue Modified n-n $^{+}$ -Si Photo-Electrode, Integrated Ferroelectrics. 135 (2012) 110–118. doi:10.1080/10584587.2012.685418.

[25] P.M. Hallam, C.E. Banks, A facile approach for quantifying the density of defects (edge plane sites) of carbon nanomaterials and related structures, Phys. Chem. Chem. Phys. 13 (2011) 1210–1213. doi:10.1039/C0CP01562H.

[26] S. Jana, A. Mondal, Fabrication of SnO_2 /α-Fe_2O_3 , SnO_2 /α-Fe_2O_3 –PB Heterostructure Thin Films: Enhanced Photodegradation and Peroxide Sensing, ACS Applied Materials & Interfaces. 6 (2014) 15832–15840. doi:10.1021/am5030879.

[27] S. Wu, Q. He, C. Tan, Y. Wang, H. Zhang, Graphene-Based Electrochemical Sensors, Small. 9 (2013) 1160–1172. doi:10.1002/smll.201202896.

[28] A. Ambrosi, M. Pumera, 3D-printing technologies for electrochemical applications, Chemical Society Reviews. 45 (2016) 2740–2755. doi:10.1039/C5CS00714C.

[29] B.R. Liyarita, A. Ambrosi, M. Pumera, 3D-printed Electrodes for Sensing of Biologically Active Molecules, Electroanalysis. 30 (2018) 1319–1326. doi:10.1002/elan.201700828.

[30] J.-Y. Lee, J. An, C.K. Chua, Fundamentals and applications of 3D printing for novel materials, Applied Materials Today. 7 (2017) 120–133. doi:10.1016/j.apmt.2017.02.004.

[31] A.L. Jardini, M.A. Larosa, R.M. Filho, C.A. de C. Zavaglia, L.F. Bernardes, C.S. Lambert, D.R. Calderoni, P. Kharmandayan, Cranial reconstruction: 3D biomodel and custom-built implant created using additive manufacturing, Journal of Cranio-Maxillofacial Surgery. 42 (2014) 1877–1884. doi:10.1016/j.jcms.2014.07.006.

[32] T.D. Ngo, A. Kashani, G. Imbalzano, K.T.Q. Nguyen, D. Hui, Additive manufacturing (3D printing): A review of materials, methods, applications and challenges, Composites Part B: Engineering. 143 (2018) 172–196. doi:10.1016/j.compositesb.2018.02.012.

[33] V. Mironov, R.P. Visconti, V. Kasyanov, G. Forgacs, C.J. Drake, R.R. Markwald, Organ printing: Tissue spheroids as building blocks, Biomaterials. 30 (2009) 2164–2174. doi:10.1016/j.biomaterials.2008.12.084.

[34] A.H. Loo, C.K. Chua, M. Pumera, DNA biosensing with 3D printing technology, The Analyst. 142 (2017) 279–283. doi:10.1039/C6AN02038K.

[35] C. Parra-Cabrera, C. Achille, S. Kuhn, R. Ameloot, 3D printing in chemical engineering and catalytic technology: structured catalysts, mixers and reactors, Chemical Society Reviews. 47 (2018) 209–230. doi:10.1039/C7CS00631D.

[36] C. Tan, M.Z.M. Nasir, A. Ambrosi, M. Pumera, 3D Printed Electrodes for Detection of Nitroaromatic Explosives and Nerve Agents, Analytical Chemistry. 89 (2017) 8995–9001. doi:10.1021/acs.analchem.7b01614.

[37] B. Gross, S.Y. Lockwood, D.M. Spence, Recent Advances in Analytical Chemistry by 3D Printing, Analytical Chemistry. 89 (2017) 57–70. doi:10.1021/acs.analchem.6b04344.

[38] C.L. Manzanares Palenzuela, F. Novotný, P. Krupička, Z. Sofer, M. Pumera, 3D-Printed Graphene/Polylactic Acid Electrodes Promise High Sensitivity in Electroanalysis, Analytical Chemistry. 90 (2018) 5753–5757. doi:10.1021/acs.analchem.8b00083.

[39] M.N.L. de Camargo, M. Santhiago, C.M. Maroneze, C.C.C. Silva, R.A. Timm, L.T. Kubota, Tuning the electrochemical reduction of graphene oxide: structural correlations towards the electrooxidation of nicotinamide adenine dinucleotide hydride, Electrochimica Acta. 197 (2016) 194–199. doi:10.1016/j.electacta.2015.09.022.

[40] Pãmyla L. dos Santos, V. Katic, H. Loureiro, M. F. dos Santos, A.L. Formiga, J.A. Bonacin, Enhanced Performance of 3D printed graphene electrodes after electrochemical pre-treatment: Role of exposed graphene sheets, Sensors and Actuator B: Chemical. submitted (2018).

[41] L. Chen, X. Wang, X. Zhang, H. Zhang, 3D porous and redox-active prussian blue-in-graphene aerogels for highly efficient electrochemical detection of H2O2, Journal of Materials Chemistry. 22 (2012) 22090. doi:10.1039/c2jm34541b.

[42] R.J. Mortimer, Electrochromic materials, Chemical Society Reviews. 26 (1997) 147. doi:10.1039/cs9972600147.

[43] A. Karyakin, On the mechanism of H2O2 reduction at Prussian Blue modified electrodes, Electrochemistry Communications. 1 (1999) 78–82. doi:10.1016/S1388-2481(99)00010-7.

[44] J.F. Watts, High resolution XPS of organic polymers: The Scienta ESCA 300 database. G. Beamson and D. Briggs. 280pp., £65. John Wiley & Sons, Chichester, ISBN 0471 935921, (1992): BOOK REVIEW, Surface and Interface Analysis. 20 (1993) 267–267. doi:10.1002/sia.740200310.

[45] A.J. Bard, L.R. Faulkner, Electrochemical methods: fundamentals and applications, 2nd ed, Wiley, New York, 2001.

[46] J.A. Bonacin, P.L. Dos Santos, V. Katic, C.W. Foster, C.E. Banks, Use of Screen-printed Electrodes Modified by Prussian Blue and Analogues in Sensing of Cysteine, Electroanalysis. 30 (2018) 170–179. doi:10.1002/elan.201700628.

[47] R.S. Nicholson, Theory and Application of Cyclic Voltammetry for Measurement of Electrode Reaction Kinetics., Analytical Chemistry. 37 (1965) 1351–1355. doi:10.1021/ac60230a016.

[48] M.A. Malik, P.J. Kulesza, R. Wlodarczyk, G. Wittstock, R. Szargan, H. Bala, Z. Galus, Formation of ultra-thin prussian blue layer on carbon steel that promotes adherence of hybrid polypyrrole based protective coating, Journal of Solid State Electrochemistry. 9 (2005) 403–411. doi:10.1007/s10008-005-0654-x.

[49] Matheus F. dos Santos, Vera Katic, P.L. dos Santos, B. Morandi Pires, A.L. Formiga, J.A. Bonacin, 3D printed low-cost spectroelectrochemical cell for in situ Raman measurements, submitted, Electrochimica acta. (2018).

[50] L. Cao, Y. Liu, B. Zhang, L. Lu, In situ Controllable Growth of Prussian Blue Nanocubes on Reduced Graphene Oxide: Facile Synthesis and Their Application as Enhanced Nanoelectrocatalyst for H 2 O 2 Reduction, ACS Applied Materials & Interfaces. 2 (2010) 2339–2346. doi:10.1021/am100372m.

[51] F. Meng, X. Zhang, B. Xu, S. Yue, H. Guo, Y. Luo, Alkali-treated graphene oxide as a solid base catalyst: synthesis and electrochemical capacitance of graphene/carbon composite aerogels, Journal of Materials Chemistry. 21 (2011) 18537. doi:10.1039/c1jm13960f.

[52] A.C. Ferrari, Raman spectroscopy of graphene and graphite: Disorder, electron–phonon coupling, doping and nonadiabatic effects, Solid State Communications. 143 (2007) 47–57. doi:10.1016/j.ssc.2007.03.052.

[53] K. Itaya, T. Ataka, S. Toshima, Spectroelectrochemistry and electrochemical preparation method of Prussian blue modified electrodes, Journal of the American Chemical Society. 104 (1982) 4767–4772. doi:10.1021/ja00382a006.

[54] P. Chen, R.L. McCreery, Control of Electron Transfer Kinetics at Glassy Carbon Electrodes by Specific Surface Modification, Analytical Chemistry. 68 (1996) 3958–3965. doi:10.1021/ac960492r.

[55] R.R. Moore, C.E. Banks, R.G. Compton, Basal Plane Pyrolytic Graphite Modified Electrodes: Comparison of Carbon Nanotubes and Graphite Powder as Electrocatalysts, Analytical Chemistry. 76 (2004) 2677–2682. doi:10.1021/ac040017q.

[56] P. Heiduschka, A.W. Munz, W. Göpel, Impedance spectroscopy and scanning tunneling microscopy of polished and electrochemically pretreated glassy carbon, Electrochimica Acta. 39 (1994) 2207–2223. doi:10.1016/0013-4686(94)E0166-W.

[57] T.J. Davies, M.E. Hyde, R.G. Compton, Nanotrench Arrays Reveal Insight into Graphite Electrochemistry, Angewandte Chemie International Edition. 44 (2005) 5121–5126. doi:10.1002/anie.200462750.

[58] A.A. Karyakin, E.E. Karyakina, Prussian Blue-based `artificial peroxidase' as a transducer for hydrogen peroxide detection. Application to biosensors, Sensors and Actuators B: Chemical. 57 (1999) 268–273. doi:10.1016/S0925-4005(99)00154-9.

[59] B.M. Pires, F.E. Galdino, J.A. Bonacin, Electrocatalytic reduction of oxygen by metal coordination polymers produced from pentacyanidoferrate(II) complex, Inorganica Chimica Acta. 466 (2017) 166–173. doi:10.1016/j.ica.2017.06.003.

[60] M.P. O'Halloran, M. Pravda, G.G. Guilbault, Prussian Blue bulk modified screen-printed electrodes for H2O2 detection and for biosensors, Talanta. 55 (2001) 605–611. doi:10.1016/S0039-9140(01)00469-6.

[61] E. Nossol, A.J.G. Zarbin, A Simple and Innovative Route to Prepare a Novel Carbon Nanotube/Prussian Blue Electrode and its Utilization as a Highly Sensitive H_2O_2 Amperometric Sensor, Advanced Functional Materials. 19 (2009) 3980–3986. doi:10.1002/adfm.200901478.

[62] Y. Zhang, X. Sun, L. Zhu, H. Shen, N. Jia, Electrochemical sensing based on graphene oxide/Prussian blue hybrid film modified electrode, Electrochimica Acta. 56 (2011) 1239–1245. doi:10.1016/j.electacta.2010.11.011.

[63] J.P. Metters, R.O. Kadara, C.E. Banks, New directions in screen printed electroanalytical sensors: an overview of recent developments, The Analyst. 136 (2011) 1067. doi:10.1039/c0an00894j.

[64] H. Beitollahi, H. Karimi-Maleh, H. Khabazzadeh, Nanomolar and Selective Determination of Epinephrine in the Presence of Norepinephrine Using Carbon Paste Electrode Modified with Carbon Nanotubes and Novel 2-(4-Oxo-3-phenyl-3,4-dihydro-quinazolinyl)- *N* ′-phenyl-hydrazinecarbothioamide, Analytical Chemistry. 80 (2008) 9848–9851. doi:10.1021/ac801854j.

[65] M. Mazloum-Ardakani, B. Ganjipour, H. Beitollahi, M.K. Amini, F. Mirkhalaf, H. Naeimi, M. Nejati-Barzoki, Simultaneous determination of levodopa, carbidopa and tryptophan using nanostructured electrochemical sensor based on novel hydroquinone and carbon nanotubes: Application to the analysis of some real samples, Electrochimica Acta. 56 (2011) 9113–9120. doi:10.1016/j.electacta.2011.07.021.

[66] Z. Taleat, M. Mazloum Ardakani, H. Naeimi, H. Beitollahi, M. Nejati, H. Reza Zare, Electrochemical Behavior of Ascorbic Acid at a 2,2′-[3,6-Dioxa-1,8-octanediylbis(nitriloethylidyne)]-bis-hydroquinone Carbon Paste Electrode, Analytical Sciences. 24 (2008) 1039–1044. doi:10.2116/analsci.24.1039.

[67] B. Morandi Pires, S.A. Venturinelli Jannuzzi, A.L. Barboza Formiga, J. Alves Bonacin, Prussian Blue Films Produced by Pentacyanidoferrate(II) and Their Application as Active Electrochemical Layers: Prussian Blue Films as Active Electrochemical Layers, European Journal of Inorganic Chemistry. 2014 (2014) 5812-N5819. doi:10.1002/ejic.201402760.

[68] H. Beitollahi, M.A. Taher, M. Ahmadipour, R. Hosseinzadeh, Electrocatalytic determination of captopril using a modified carbon nanotube paste electrode: Application to determination of captopril in pharmaceutical and biological samples, Measurement. 47 (2014) 770–776. doi:10.1016/j.measurement.2013.10.001.

[69] H. Karimi-Maleh, A.A. Ensafi, H. Beitollahi, V. Nasiri, M.A. Khalilzadeh, P. Biparva, Electrocatalytic determination of sulfite using a modified carbon nanotubes paste electrode: application for determination of sulfite in real samples, Ionics. 18 (2012) 687–694. doi:10.1007/s11581-011-0654-z.

[70] C.E. Banks, C.W. Foster, R.O. Kadara, Screen-Printing Electrochemical Architectures, Springer International Publishing, Cham, 2016. doi:10.1007/978-3-319-25193-6.

[71] J.R. Windmiller, J. Wang, Wearable Electrochemical Sensors and Biosensors: A Review, Electroanalysis. 25 (2013) 29–46. doi:10.1002/elan.201200349.

[72] K. Kalantar-zadeh, B. Fry, Nanotechnology-Enabled Sensors, Springer US, Boston, MA, 2008. doi:10.1007/978-0-387-68023-1.

[73] S. Sadeghi, A. Garmroodi, Design and Construction of a New Modified Screen-Printed Sensor for Voltammetric Determination of Molybdenum(VI) Ions, Electroanalysis. 25 (2013) 323–330. doi:10.1002/elan.201200413.

[74] C.W. Foster, J.P. Metters, D.K. Kampouris, C.E. Banks, Ultraflexible Screen-Printed Graphitic Electroanalytical Sensing Platforms, Electroanalysis. 26 (2014) 262–274. doi:10.1002/elan.201300563.

[75] N. Jadon, R. Jain, S. Sharma, K. Singh, Recent trends in electrochemical sensors for multianalyte detection – A review, Talanta. 161 (2016) 894–916. doi:10.1016/j.talanta.2016.08.084.

[76] M.C. Gallo, B.M. Pires, K.C.F. Toledo, S.A.V. Jannuzzi, E.G.R. Arruda, A.L.B. Formiga, J.A. Bonacin, The use of modified electrodes by hybrid systems gold nanoparticles/Mn-porphyrin in electrochemical detection of cysteine, Synthetic Metals. 198 (2014) 335–339. doi:10.1016/j.synthmet.2014.10.024.

[77] S. Shahrokhian, Lead Phthalocyanine as a Selective Carrier for Preparation of a Cysteine-Selective Electrode, Analytical Chemistry. 73 (2001) 5972–5978. doi:10.1021/ac010541m.

[78] M.C. Monteiro, K.C.F. Toledo, B.M. Pires, R. Wick, J.A. Bonacin, Improvement in Efficiency of the Electrocatalytic Reduction of Hydrogen Peroxide by Prussian Blue Produced from the $[Fe(CN)_5(mpz)]^{2-}$ Complex: Improvement in Efficiency of the Electrocatalytic Reduction of Hydrogen Peroxide by Prussian Blue Produced from the $[Fe(CN)_5(mpz)]^{2-}$ Complex, European Journal of Inorganic Chemistry. 2017 (2017) 1979–1988. doi:10.1002/ejic.201601540.

[79] H. Karimi-Maleh, A.A. Ensafi, H. Beitollahi, V. Nasiri, M.A. Khalilzadeh, P. Biparva, Electrocatalytic determination of sulfite using a modified carbon nanotubes paste electrode: application for determination of sulfite in real samples, Ionics. 18 (2012) 687–694. doi:10.1007/s11581-011-0654-z.

[80] A.L.B. Formiga, S. Vancoillie, K. Pierloot, Electronic Spectra of *N* -Heterocyclic Pentacyanoferrate(II) Complexes in Different Solvents, Studied by Multiconfigurational Perturbation Theory, Inorganic Chemistry. 52 (2013) 10653–10663. doi:10.1021/ic401704r.

[81] E. Blanco, C.W. Foster, L.R. Cumba, D.R. do Carmo, C.E. Banks, Can solvent induced surface modifications applied to screen-printed platforms enhance their electroanalytical performance?, The Analyst. 141 (2016) 2783–2790. doi:10.1039/C6AN00440G.

[82] S.J. Rowley-Neale, G.C. Smith, C.E. Banks, Mass-Producible 2D-MoS_2 -Impregnated Screen-Printed Electrodes That Demonstrate Efficient

Electrocatalysis toward the Oxygen Reduction Reaction, ACS Applied Materials & Interfaces. 9 (2017) 22539–22548. doi:10.1021/acsami.7b05104.

[83] R.J. Mortimer, D.R. Rosseinsky, Iron hexacyanoferrate films : spectroelectrochemical distinction and electrodeposition sequence of “soluble” (K+-containing) and “insoluble” (K+-free) Prussian Blue, and composition changes in polyelectrochromic switching, Journal of the Chemical Society, Dalton Transactions. (1984) 2059. doi:10.1039/dt9840002059.

[84] W.T. Tan, A.M. Bond, S.W. Ngooi, E.B. Lim, J.K. Goh, Electrochemical oxidation of l-cysteine mediated by a fullerene-C60-modified carbon electrode, Analytica Chimica Acta. 491 (2003) 181–191. doi:10.1016/S0003-2670(03)00791-8.

[85] S. Fei, J. Chen, S. Yao, G. Deng, D. He, Y. Kuang, Electrochemical behavior of l-cysteine and its detection at carbon nanotube electrode modified with platinum, Analytical Biochemistry. 339 (2005) 29–35. doi:10.1016/j.ab.2005.01.002.

[86] N. Hernández-Ibáñez, I. Sanjuán, M.Á. Montiel, C.W. Foster, C.E. Banks, J. Iniesta, l -Cysteine determination in embryo cell culture media using Co (II)-phthalocyanine modified disposable screen-printed electrodes, Journal of Electroanalytical Chemistry. 780 (2016) 303–310. doi:10.1016/j.jelechem.2016.09.028.

[87] C.C. Corrêa, S.A.V. Jannuzzi, M. Santhiago, R.A. Timm, A.L.B. Formiga, L.T. Kubota, Modified electrode using multi-walled carbon nanotubes and a metallopolymer for amperometric detection of l-cysteine, Electrochimica Acta. 113 (2013) 332–339. doi:10.1016/j.electacta.2013.09.050.

[88] J.-B. Raoof, R. Ojani, H. Beitollahi, L-Cysteine Voltammetry at a Carbon Paste Electrode Bulk-Modified with Ferrocenedicarboxylic Acid, Electroanalysis. 19 (2007) 1822–1830. doi:10.1002/elan.200703932.

[89] Y. Zhai, Z. Zhu, S. Zhou, C. Zhu, S. Dong, Recent advances in spectroelectrochemistry, Nanoscale. 10 (2018) 3089–3111. doi:10.1039/C7NR07803J.

[90] W. Kaim, J. Fiedler, Spectroelectrochemistry: the best of two worlds, Chemical Society Reviews. 38 (2009) 3373. doi:10.1039/b504286k.

[91] L. León, J.D. Mozo, Designing spectroelectrochemical cells: A review, TrAC Trends in Analytical Chemistry. 102 (2018) 147–169. doi:10.1016/j.trac.2018.02.002.

[92] T.E. Rosser, E. Reisner, Understanding Immobilized Molecular Catalysts for Fuel-Forming Reactions through UV/Vis Spectroelectrochemistry, ACS Catalysis. 7 (2017) 3131–3141. doi:10.1021/acscatal.7b00326.

[93] C.N. Hernández, D. Martín-Yerga, M.B. González-García, D. Hernández-Santos, P. Fanjul-Bolado, Evaluation of electrochemical, UV/VIS and Raman spectroelectrochemical detection of Naratriptan with screen-printed electrodes, Talanta. 178 (2018) 85–88. doi:10.1016/j.talanta.2017.09.004.

[94] A.J. Wain, M.A. O'Connell, G.A. Attard, Insights into Self-Poisoning during Catalytic Hydrogenation on Platinum Surfaces Using ATR-IR Spectroelectrochemistry, ACS Catalysis. 8 (2018) 3561–3570. doi:10.1021/acscatal.8b00492.

[95] C.A. Melendres, N. Camillone, T. Tipton, Laser raman spectroelectrochemical studies of anodic corrosion and film formation on iron in phosphate solutions, Electrochimica Acta. 34 (1989) 281–286. doi:10.1016/0013-4686(89)87098-7.

[96] R. Mazeikiene, A. Statino, Z. Kuodis, G. Niaura, A. Malinauskas, In situ Raman spectroelectrochemical study of self-doped polyaniline degradation kinetics, Electrochemistry Communications. 8 (2006) 1082–1086. doi:10.1016/j.elecom.2006.04.017.

[97] H. Luo, M.J. Weaver, A versatile surface Raman spectroelectrochemical flow cell: applications to chemisorbate kinetics, Journal of Electroanalytical Chemistry. 501 (2001) 141–150. doi:10.1016/S0022-0728(00)00517-9.

[98] M.W. Louie, A.T. Bell, An Investigation of Thin-Film Ni–Fe Oxide Catalysts for the Electrochemical Evolution of Oxygen, Journal of the American Chemical Society. 135 (2013) 12329–12337. doi:10.1021/ja405351s.

[99] O. Diaz-Morales, F. Calle-Vallejo, C. de Munck, M.T.M. Koper, Electrochemical water splitting by gold: evidence for an oxide decomposition mechanism, Chemical Science. 4 (2013) 2334. doi:10.1039/c3sc50301a.

[100] K.S. Joya, X. Sala, In situ Raman and surface-enhanced Raman spectroscopy on working electrodes: spectroelectrochemical characterization of water oxidation electrocatalysts, Physical Chemistry Chemical Physics. 17 (2015) 21094–21103. doi:10.1039/C4CP05053C.

[101] B.S. Yeo, A.T. Bell, In Situ Raman Study of Nickel Oxide and Gold-Supported Nickel Oxide Catalysts for the Electrochemical Evolution of Oxygen, The Journal of Physical Chemistry C. 116 (2012) 8394–8400. doi:10.1021/jp3007415.

[102] R.A. Timm, E.T.S.G. da Silva, V.C. Bassetto, H.D. Abruña, L.T. Kubota, Versatile and low cost spectroelectrochemical cell for in situ study of electrode surfaces, Electrochimica Acta. 232 (2017) 150–155. doi:10.1016/j.electacta.2017.02.132.

[103] R.M. Cardoso, D.M.H. Mendonça, W.P. Silva, M.N.T. Silva, E. Nossol, R.A.B. da Silva, E.M. Richter, R.A.A. Muñoz, 3D printing for electroanalysis: From multiuse electrochemical cells to sensors, Analytica Chimica Acta. 1033 (2018) 49–57. doi:10.1016/j.aca.2018.06.021.

[104] G.N. Meloni, 3D Printed and Microcontrolled: The One Hundred Dollars Scanning Electrochemical Microscope, Analytical Chemistry. 89 (2017) 8643–8649. doi:10.1021/acs.analchem.7b01764.

[105] P.R. Miller, X. Xiao, I. Brener, D.B. Burckel, R. Narayan, R. Polsky, Microneedle-Based Transdermal Sensor for On-Chip Potentiometric Determination of K^+,

Advanced Healthcare Materials. 3 (2014) 876–881. doi:10.1002/adhm.201300541.

[106] C.L. Manzanares Palenzuela, M. Pumera, (Bio)Analytical chemistry enabled by 3D printing: Sensors and biosensors, TrAC Trends in Analytical Chemistry. 103 (2018) 110–118. doi:10.1016/j.trac.2018.03.016.

[107] T.-S. Wei, B.Y. Ahn, J. Grotto, J.A. Lewis, 3D Printing of Customized Li-Ion Batteries with Thick Electrodes, Advanced Materials. 30 (2018) 1703027. doi:10.1002/adma.201703027.

[108] P.J. Kitson, M.H. Rosnes, V. Sans, V. Dragone, L. Cronin, Configurable 3D-Printed millifluidic and microfluidic 'lab on a chip' reactionware devices, Lab on a Chip. 12 (2012) 3267. doi:10.1039/c2lc40761b.

[109] K. Sun, T.-S. Wei, B.Y. Ahn, J.Y. Seo, S.J. Dillon, J.A. Lewis, 3D Printing of Interdigitated Li-Ion Microbattery Architectures, Advanced Materials. 25 (2013) 4539–4543. doi:10.1002/adma.201301036.

[110] G. Moretti, C. Gervais, Raman spectroscopy of the photosensitive pigment Prussian blue, Journal of Raman Spectroscopy. 49 (2018) 1198–1204. doi:10.1002/jrs.5366.

[111] K. Nakamoto, Infrared and Raman Spectra of Inorganic and Coordination Compounds, John Wiley & Sons, Inc., Hoboken, NJ, USA, 2008. doi:10.1002/9780470405840.

[112] L. Samain, B. Gilbert, F. Grandjean, G.J. Long, D. Strivay, Redox reactions in Prussian blue containing paint layers as a result of light exposure, Journal of Analytical Atomic Spectrometry. 28 (2013) 524. doi:10.1039/c3ja30359d.

[113] E. Nossol, A.J. Gorgatti Zarbin, Transparent films from carbon nanotubes/Prussian blue nanocomposites: preparation, characterization, and application as electrochemical sensors, J. Mater. Chem. 22 (2012) 1824–1833. doi:10.1039/C1JM14225A.

[114] S.A. Agnihotry, P. Singh, A.G. Joshi, D.P. Singh, K.N. Sood, S.M. Shivaprasad, Electrodeposited Prussian blue films: Annealing effect, Electrochimica Acta. 51 (2006) 4291–4301. doi:10.1016/j.electacta.2005.12.008.

[115] P.L. dos Santos, R.A. Timm, L.T. Kubota, J.A. Bonacin, Modulation of Electrochemical Properties of Graphene Oxide by Photochemical Reduction Using UV-Light Emitting Diodes, ChemistrySelect. 1 (2016) 1168–1175. doi:10.1002/slct.201600121.

[116] F. Gao, X. Cai, X. Wang, C. Gao, S. Liu, F. Gao, Q. Wang, Highly sensitive and selective detection of dopamine in the presence of ascorbic acid at graphene oxide modified electrode, Sensors and Actuators B: Chemical. 186 (2013) 380–387. doi:10.1016/j.snb.2013.06.020.

[117] J. Huang, L. Zhang, B. Chen, N. Ji, F. Chen, Y. Zhang, Z. Zhang, Nanocomposites of size-controlled gold nanoparticles and graphene oxide:

Formation and applications in SERS and catalysis, Nanoscale. 2 (2010) 2733. doi:10.1039/c0nr00473a.

[118] M. Santhiago, C.M. Maroneze, C.C.C. Silva, M.N.L. Camargo, L.T. Kubota, Electrochemical Oxidation of Glassy Carbon Provides Similar Electrochemical Response as Graphene Oxide Prepared by Tour or Hummers Routes, ChemElectroChem. 2 (2015) 761–767. doi:10.1002/celc.201402387.

[119] A.C. Ferrari, Raman spectroscopy of graphene and graphite: Disorder, electron–phonon coupling, doping and nonadiabatic effects, Solid State Communications. 143 (2007) 47–57. doi:10.1016/j.ssc.2007.03.052.

[120] L.M. Malard, M.A. Pimenta, G. Dresselhaus, M.S. Dresselhaus, Raman spectroscopy in graphene, Physics Reports. 473 (2009) 51–87. doi:10.1016/j.physrep.2009.02.003.

[121] K. Zhang, Y. Zhang, S. Wang, Enhancing thermoelectric properties of organic composites through hierarchical nanostructures, Scientific Reports. 3 (2013). doi:10.1038/srep03448.

[122] J.C. Scaiano, P. Billone, C.M. Gonzalez, L. Marett, M.L. Marin, K.L. McGilvray, N. Yuan, Photochemical routes to silver and gold nanoparticles, Pure and Applied Chemistry. 81 (2009) 635–647. doi:10.1351/PAC-CON-08-09-11.

[123] K.L. McGilvray, M.R. Decan, D. Wang, J.C. Scaiano, Facile Photochemical Synthesis of Unprotected Aqueous Gold Nanoparticles, Journal of the American Chemical Society. 128 (2006) 15980–15981. doi:10.1021/ja066522h.

[124] R. Jin, Photoinduced Conversion of Silver Nanospheres to Nanoprisms, Science. 294 (2001) 1901–1903. doi:10.1126/science.1066541.

[125] K.G. Stamplecoskie, J.C. Scaiano, Light Emitting Diode Irradiation Can Control the Morphology and Optical Properties of Silver Nanoparticles, Journal of the American Chemical Society. 132 (2010) 1825–1827. doi:10.1021/ja910010b.

[126] Santos Pãmyla Layene dos, Obtenção fotoquímica de nanocompósito baseado em azul da Prússia e óxido de grafeno reduzido, UNICAMP, 2015. http://www.repositorio.unicamp.br/handle/REPOSIP/250675.

[127] V. Katic, P. Santos, J. Gabriel, A. Salomão, J. Bonacin, ASSEMBLY OF LOW-COST LAB-MADE PHOTOREACTOR FOR PREPARATION OF NANOMATERIALS, Química Nova. (2017). doi:10.21577/0100-4042.20170123.

[128] J.A. Bonacin, F.M. Engelmann, D. Severino, H.E. Toma, M.S. Baptista, Singlet oxygen quantum yields (Φd) in water using beetroot extract and an array of LEDs, Journal of the Brazilian Chemical Society. 20 (2009) 31–36. doi:10.1590/S0103-50532009000100006.

[129] D. Chen, Photocatalytic kinetics of phenol and its derivatives over UV irradiated TiO2, Applied Catalysis B: Environmental. 23 (1999) 143–157. doi:10.1016/S0926-3373(99)00068-5.

[130] S. Gelover, P. Mondragón, A. Jiménez, Titanium dioxide sol–gel deposited over glass and its application as a photocatalyst for water decontamination, Journal of Photochemistry and Photobiology A: Chemistry. 165 (2004) 241–246. doi:10.1016/j.jphotochem.2004.03.023.

[131] J.-P. Correa-Baena, A. Abate, M. Saliba, W. Tress, T. Jesper Jacobsson, M. Grätzel, A. Hagfeldt, The rapid evolution of highly efficient perovskite solar cells, Energy & Environmental Science. 10 (2017) 710–727. doi:10.1039/C6EE03397K.

[132] S.F. Sousa, A.O.T. Patrocinio, COORDINATION CHEMISTRY AND SOLAR FUEL PRODUCTION, Química Nova. (2014). doi:10.5935/0100-4042.20140140.

[133] E. Gachard, H. Remita, J. Khatouri, B. Keita, L. Nadjo, and J. Belloni, Radiation-induced and chemical formation of gold clusters, New Journal of Chemistry. 22 (1998) 1257–1265. doi:10.1039/a804445g.

[134] D.R. Dreyer, S. Park, C.W. Bielawski, R.S. Ruoff, The chemistry of graphene oxide, Chem. Soc. Rev. 39 (2010) 228–240. doi:10.1039/B917103G.

[135] Y. Matsumoto, M. Koinuma, S. Ida, S. Hayami, T. Taniguchi, K. Hatakeyama, H. Tateishi, Y. Watanabe, S. Amano, Photoreaction of Graphene Oxide Nanosheets in Water, The Journal of Physical Chemistry C. 115 (2011) 19280–19286. doi:10.1021/jp206348s.